

Computational and Experimental Nano Mechanics

Amir Alipour Skandani

Dissertation submitted to the faculty of the Virginia Polytechnic Institute and State University in
partial fulfillment of the requirements for the degree of

Doctor of Philosophy
In
Engineering Mechanics

Marwan Al-Haik, Chair
Muhammad R. Hajj
Scott W. Case
Mayuresh J. Patil
Sunny Jung

August 14, 2014
Blacksburg, VA

Keywords: Carbon nano tubes, ZnO nano rods, Viscoelasticity, Viscoplasticity, molecular dynamics, nano composites, nano characterization, lipid cell membrane

Computational and Experimental Nano Mechanics

Amir Alipour Skandani

ABSTRACT

The many advances of nano technology extensively revolutionize mechanics. A tremendous need is growing to further bridge the gap between the classical mechanics and the nano scale for many applications at different engineering fields. For instance, the themes of interdisciplinary and multidisciplinary topics are getting more and more attention especially when the coherency is needed in diagnosing and treating terminal diseases or overcoming environmental threats. The fact that how mechanical, biomedical and electrical engineering can contribute to diagnosing and treating a tumor per se is both interesting and unveiling the necessity of further investments in these fields. This dissertation presents three different investigations in the area of nano mechanics and nano materials spanning from computational bioengineering to making mechanically more versatile composites.

The first part of this dissertation presents a numerical approach to study the effects of the carbon nano tubes (CNTs) on the human body in general and their absorbability into the lipid cell membranes in particular. Single wall carbon nano tubes (SWCNTs) are the elaborate examples of nano materials that departed from mere mechanical applications to the biomedical applications such as drug delivery vehicles. Recently, experimental biology provided detailed insights of the SWCNTs interaction with live organs. However, due to the instrumental and technical limitations, there are still numerous concerns yet to be addressed. In such situation, utilizing numerical simulation is a viable alternative to the experimental practices. From this perspective, this dissertation reports a molecular dynamics (MD) study to provide better insights on the effect of the carbon nano tubes chiralities and aspect ratios on their interaction with a lipid bilayer membrane as well as their reciprocal effects with surface functionalizing. Single walled carbon nano tubes can be utilized to diffuse selectively on the targeted cell via surface functionalizing. Many experimental attempts have smeared polyethylene glycol (PEG) as a biocompatible surfactant to carbon nano tubes. The simulation results indicated that SWCNTs have different time-evolving mechanisms to internalize within the lipid membrane. These mechanisms comprise both penetration and endocytosis. Also, this study revealed effects of length and chirality and surface functionalizing on the penetrability of different nano tubes.

The second part of the dissertation introduces a novel *in situ* method for qualitative and quantitative measurements of the negative stiffness of a single crystal utilizing nano mechanical characterization; nano indentation. The concept of negative stiffness was first introduced by metastable structures and later by materials with negative stiffness when embedded in a stiffer (positive stiffness) matrix. However, this is the first time a direct quantitative method is developed to measure the exact value of the negative stiffness for triglycine sulfate (TGS) crystals. With the advancements in the precise measuring device and sensors, instrumented nano indentation became a reliable tool for measuring submicron properties of variety of materials ranging from single phase humongous materials to nano composites with heterogeneous microstructures.

The developed approach in this chapter of the dissertation outlines how some modifications of the standard nano indentation tests can be utilized to measure the negative stiffness of a ferroelectric material at its Curie temperature.

Finally, the last two chapters outline the possible improvements in the mechanical properties of conventional carbon fiber composites by introducing 1D nano fillers to them. Particularly, their viscoelastic and viscoplastic behavior are studied extensively and different modeling techniques are utilized. Conventional structural materials are being replaced with the fiber-reinforced plastics (FRPs) in many different applications such as civil structures or aerospace and car industries. This is mainly due to their high strength to weight ratio and relatively easy fabrication methods. However, these composites did not reach their full potential due to durability limitations. The majorities of these limitations stem from the polymeric matrix or the interface between the matrix and fibers where poor adhesion fails to carry the desired mechanical loadings. Among such failures are the time-induced deformations or delayed failures that can cause fatal disasters if not taken care of properly. Many methodologies are offered so far to improve the FRPs' resistance to this category of time-induced deformations and delayed failures. Several researchers tried to modify the chemical formulation of polymers coming up with stiffer and less viscous matrices. Others tried to modify the adhesion of the fibers to the matrix by adding different chemically functional groups onto the fibers' surface. A third approach tried to modify the fiber to matrix adhesion and at the same time improve the viscous properties of the matrix itself. This can be achieved by growing 1D nano fillers on the fibers so that one side is bonded to the fiber and the other side embedded in the matrix enhancing the matrix with less viscous deformability. It is shown that resistance to creep deformation and stress relaxation of laminated composites improved considerably in the presence of the nano fillers such as multiwall carbon nano tubes (MWCNTs) and zinc oxide nano wires (ZnO- NWs). The constitutive behaviors of these hybrid composites were investigated further through the use of the time temperatures superposition (TTS) principle for the linear viscoelastic behavior and utilizing phenomenological models for the viscoplastic behavior.

*Dedicated to my beloved parents Ahmad and Saeedeh,
for their infinite love, patience and support throughout all these years.*

Acknowledgments

The completion of all the work presented here would not have been possible without consistent supervision, thorough knowledge and generous assistance of my advisor, Dr. Al-Haik. I am deeply indebted to him for providing me the opportunity of working in many different interdisciplinary fields. Also, I would like to express my appreciation to my committee members for their valuable comments on the thesis, especially Dr. Scott Case for his assistance in providing access to some of the mechanical testing facilities.

Finally, I could not have made to this point initially without the help and support from my family, friends and teachers throughout the course of my education.

Contents

Acknowledgments	v
Contents	vi
List of Figures.....	ix
List of Tables	xiii
1. Introduction.....	1
1.1. The Emergence of Nanobiomechanics.....	1
1.2. Nano Materials for Drug Delivery	2
1.3. Nano Mechanical Characterization of Negative Stiffness Materials	4
1.4. Review of the Viscoelasto-plastic Behavior of FRPs	6
1.4.1. Maxwell Model.....	11
1.4.2. Kelvin-Voigt Model.....	11
1.4.3. Standard Linear Solid Model.....	12
1.4.4. Generalized Maxwell Model	13
1.4.5. Time-Temperature-Stress-Superposition Principle (TTSSP)	14
2. Nanobiomechanics: Carbon Nano Tubes Penetration into Lipid Membranes	17
2.1. Introduction	18
2.2. Force Field Selection.....	23
2.3. Chirality of SWCNT	25
2.3.1. Numerical Experiments	27
2.4. PEGylated SWCNTs	30
2.4.1. Numerical Experiments	31
2.5. Results and Discussion.....	33
2.5.1. Effect of SWCNT Length.....	34
2.5.2. Effect of the SWCNT Chirality	38
2.5.2.1. Adhesion Energy	39
2.5.3. Effect of Surface Functionalizing.....	40
2.5.3.1. Adhesion Energy	46
2.6. Conclusions	47

3. Nano Mechanical Characterization of the Negative Stiffness of a Ferroelectric Material using Nano Indentation	49
3.1. Introduction	50
3.2. Materials and Experiments.....	53
3.3. Results and Discussion.....	57
3.4. Conclusions	65
4. Vibrational Damping and Viscoelastic Characterization of Hybrid Carbon Fiber/ZnO Nano Rods Polymer Composite	66
4.1. Introduction	67
4.2. Experimental Methods	72
4.2.1. Samples Preparation	72
4.2.2. Sample Characterization.....	73
4.3. Results and Discussion.....	74
4.4. Conclusions	83
5. Viscoplastic Characterization of Hybrid Carbon Fiber/ Nano Phase Reinforced Composites	85
5.1. Introduction	86
5.2. Materials, Processing and Experimental Techniques:.....	90
5.2.1. Samples Preparation	90
5.2.1.1. Sizing Removal from Fibers	90
5.2.1.2. Growth of ZnO Nano Rods and CNTs.....	92
5.2.1.3. Composites Fabrication.....	92
5.2.2. Samples Characterization	93
5.2.2.1. Scanning Electron Microscopy (SEM), Thermal Gravimetric Analyzer (TGA)..	93
5.2.2.2. Mechanical Testing	93
5.3. Results and Discussion.....	95
5.3.1. Thermo Gravitational Analysis (TGA).....	98
5.3.2. Tensile Tests	99
5.3.3. Stress Relaxation	105
5.3.4. Creep.....	110
5.4. Phenomenological Modeling of Viscoplasticity	115
5.4.1. Material Parameters	117

5.4.2. Model Validation	121
5.5. Conclusions	123
6. Conclusions and Future Work.....	125
6.1. Conclusions	125
6.2. Future Work	129
7. References.....	131

List of Figures

Figure 1.1. The major phenomena in polymer matrix composites induced by high temperature and/or prolonged time ⁴⁸	9
Figure 1.2. Flowchart of the accelerated viscoelastic and delayed failure analysis schemes in polymer matrix composites via the mesomechanics approaches.....	10
Figure 1.3. Maxwell model representation.	11
Figure 1.4. Kelvin-Voigt model representation.	12
Figure 1.5. Standard linear solid model representation.	12
Figure 1.6. Generalized Maxwell model representation.	13
Figure 1.7. Schematic of different superposition principles to yield the final master curve.	15
Figure 2.1. Schematic illustration of the chiral angle and chiral vector.	26
Figure 2.2. Common PEG-SWCNT intermediary chemical bonding, a) through carboxylic acid groups and b) through 1, 3 dipolar cycloaddition reactions.....	31
Figure 2.3. A top view from the assumed structure for a (10, 0) f-SWCNT.	32
Figure 2.4. Energy minimization for the different SWCNTs and the bilayer membrane.....	33
Figure 2.5. Energy minimization data for some of the SWCNT/membrane assembled configurations.	34
Figure 2.6. Normalized total energy and temperature evolutions during the molecular dynamic simulation of short SWCNTs.....	35
Figure 2.7. Normalized total energy and temperature evolutions during the molecular dynamic simulation of long SWCNTs.....	36
Figure 2.8. Sequential representation of SWCNTs penetration through cell membrane: (a) Initial configuration, (b) after 0.4 ps, (c) after 4 ps, (d) after 10 ps, (e) after 30 ps, and (f) after 60 ps..	37
Figure 2.9. Molecular dynamic evolution of the z-coordinate of bottommost carbon atom in different chiralities.....	38

Figure 2.10. Adhesion energy of the different SWCNTs/membrane configurations	40
Figure 2.11. Energy minimization evolution for different configurations.....	41
Figure 2.12. The evolution of total energy during the MD run.	42
Figure 2.13. Schematic representation of SWCNTs penetrating into lipid membrane, a) (5, 5), b) (10, 0), c) (10, 10) chiralities.	43
Figure 2.14. Schematic representation of f-SWCNTs penetrating into lipid membrane, a) (5, 5), b) (10, 0), c) (10, 10) chiralities.	44
Figure 2.15. Molecular dynamic evolution of the trajectory of the Z coordinate of the bottommost carbon atom for all studied systems.....	45
Figure 2.16. Changes in the adhesion energy after PEG functionalizing. Red bars represent the adhesion energy for different chirality SWCNTs and the adjacent blue bars are the PEG functionalized counterparts.....	47
Figure 3.1. Schematics of the (a) NanoTest system and (b) hot stage feature.....	54
Figure 3.2. (a) Nano indentation thermomechanical history of the sample using a Berkovich indenter and (b) The thermomechanical record of a nano creep test performed using spherical indenter at low load to account for deformation due to sample thermal expansion.	56
Figure 3.3. The load-temperature evolution during the nano creep test using a Berkovich nano indenter.	57
Figure 3.4. Measured XRD pattern for TGS.....	58
Figure 3.5. Indentation hysteresis pre and post unloading depth corrections. The unloading cycle was performed in the temperature range of 60-37 °C ¹²⁰	59
Figure 3.6. The time/temperature evolution of the corrected indenter penetration depth during the indentation experiment performed using a Berkovich indenter in the range of 37-60 °C.....	62
Figure 3.7. Upper part of the corrected indentation curve with the linear fit of its positive and negative sloped sections ¹²⁰	63
Figure 3.8. Time evolution of the corrected creep curve for the TGS crystal with (a) corresponding temperature and (b) depth change rate during 780 s duration creep test measured in the temperature range of 60-37 °C.....	64

Figure 4.1. XRD patterns for a) Neat carbon fiber, b) ZnO film sputtered on carbon fiber and c) ZnO-grown nano rods on carbon fibers.....	75
Figure 4.2. SEM micrograph of hydrothermally grown ZnO nano rods a-c) before and d) after hand lay-up process.....	76
Figure 4.3. Linear viscoelastic regimes of a) Neat, b) ZnO-sputtered & c) ZnO-grown composite samples.....	77
Figure 4.4. Creep compliance master curves for the different composites.....	78
Figure 4.5. Shift factor evolution for composites based on carbon fiber with ZnO grown nano rods, experimental data were fitted using WLF model with $C_1=-40$, $C_2=-285K$	79
Figure 4.6. Prolonged stress relaxation data for all configurations.	80
Figure 4.7. a) Storage modulus, b) Tan (δ) and c) Loss modulus for composites made out of raw (non-processed), sputtered (ZnO coated and soaked in solution) and growth (with surface grown ZnO nano rods) woven carbon fibers.....	82
Figure 5.1. Effect of the duration of exposure to high temperature on the fibers a) Elastic moduli, b) Ultimate strength and c) Elongation at failure.....	91
Figure 5.2. The fortified creep frame with pneumatic air cylinder and 5klb load cell.	95
Figure 5.3. Different configurations of samples a) Neat, b) heat treated, c) Substrate, d) ZnO-G, e) CNT-G and f) patterned-CNT-G.	97
Figure 5.4. Volume fraction of the epoxy matrix in the different composite samples obtianed via TGA.	98
Figure 5.5. Mechanical properties of different composites configurations at 25 °C, a) Ultimate Strength, b) Elastic modulus and c) Elongation to failure.	100
Figure 5.6. Mechanical properties of different composites configurations at 45 °C, a) Ultimate Strength, b) Elastic modulus and c) Elongation to failure.	102
Figure 5.7. Mechanical properties of different composites configurations at 65 °C, a) Ultimate Strength, b) Elastic modulus and c) Elongation to failure.	103
Figure 5.8. Mechanical properties of different composite configurations at 85 °C, a) Ultimate Strength, b) Elastic modulus and c) Elongation to failure.	105

Figure 5.9. Stress relaxation curves for the Neat composite samples at different temperatures.	106
Figure 5.10. Stress relaxation curves for the HT composite samples at different temperatures.	106
Figure 5.11. Stress relaxation curves for the Substrate composite samples at different temperatures.....	107
Figure 5.12. Stress relaxation curves for the ZnO composite samples at different temperatures.	107
Figure 5.13. Stress relaxation curves for CNT composite samples at different temperatures....	108
Figure 5.14. Stress relaxation curves for Pat-CNT composite samples at different temperatures.	108
Figure 5.15. Creep curves for Neat composite samples at different temperatures.	110
Figure 5.16. Creep curves for the HT composite samples at different temperatures.....	111
Figure 5.17. Creep curves for Substrate composite samples at different temperatures.....	111
Figure 5.18. Creep curves for ZnO composite samples at different temperatures.	112
Figure 5.19. Creep curves for CNT composite samples at different temperatures.....	112
Figure 5.20. Creep curves for pat- CNT composite samples at different temperatures.....	113
Figure 5.21. $\log\sigma - \log\dot{\varepsilon}vp$ Plot for CNT sample at 85 °C.....	118
Figure 5.22. A sample plot of $\log\sigma - \sigma * -\log\dot{\varepsilon}p$ for CNT sample at different temperatures. These curves are used to determine the material constants K and m at each temperature (Overstress is in MPa).....	119
Figure 5.23. A sample plot of $\log\varepsilon - \sigma */E - \log\sigma *$ for CNT sample at different temperatures. These curves are used to determine the material constants A and n at each temperature (Quasistatic stress is in MPa).....	120
Figure 5.24. A sample plot of experimental data versus model prediction for the CNT composite sample at four different temperatures and load levels.....	122

List of Tables

Table 2.1. Total number of atoms utilized in MD simulation for chiral nano tubes.	28
Table 4.1. Differences in creep compliance and stress relaxation modulus for each configuration with the standard deviation.	81
Table 5.1. Normilized percentage of stress reduction after 15 mins for the different composites configurations.	109
Table 5.2. Normilized percentage of creep after 15 mins for the different compsoites configurations.	114
Table 5.3. Material Parameters m , K , n , and A for the different composite configurations.	121

|Chapter 1

1. Introduction

1.1. The Emergence of Nanobiomechanics

The emergence of nano materials in the biological applications spans from diagnostic tools to drug delivery vehicles. This constitutes the nanobiomechanics as a growing interdisciplinary/multidisciplinary field. Both experimentalist from the biological side and modelers from the mechanics side have contributed significantly to this field. The hows and whys of many biomechanical phenomena are discovered so far but much more remain unknown. Tissues in live organs and biological materials have a hierarchical design from nano scale to macro scale and even larger. Bone as an example is made up of materials with seven levels of different scales starting from hydroxylapatite fibers with average size less than 100 nm¹. This and many identical examples vindicate the application of the nano scale instruments into the biology field. The majority of the nano scale studies in the biological science are tied to the measurements of the forces in the living cells. For instance, studying the red blood cells revealed that the stiffness of these cells can increase up to 10 times when infected by malaria ², or majority of cancer cells

become up to 70% less stiff than normal cells ³. The concepts such as force, stiffness and deformation are the natural places where knowledge of the classical mechanics can play a role. In spite of the development of high precision measuring instruments and imaging techniques there are still considerable limitations to overcome all the possible challenges. Therefore, computer assisted simulations and particularly molecular dynamics simulations (MD) turned out to be powerful tools in understanding some of the phenomena occurring at the nano scale where accessing or measuring the physical parameters are impossible or erroneous. Molecular dynamics simulations have been extensively utilized in unfolding the facts behind many biological phenomena so far. The results obtained from MD are trustworthy when the appropriate force field is chosen and the correct thermo dynamical ensemble is applied throughout the simulation.

1.2. Nano Materials for Drug Delivery

Drug delivery admissibility of engineered nano materials such as carbon nano tubes (CNTs) coupled with the uncertainties about their interaction with live organs and their possible side effects on human health engrossed a tremendous deal of research. Single wall carbon nano tubes (SWCNTs) are promising candidates for cancer invasive treatments such as photo-thermal and photo acoustic therapies due to their high near-infrared absorption. They are also viable for drug delivery due to their high diffusivity through cells' membranes. The drug delivery functionality of SWCNTs can be attributed partially to their ability in transfecting through different cell membranes in the human body. Such penetration can be affected by the different properties of SWCNTs such as the length to diameter ratio of the nano tubes (i.e. chirality). In most of their bio missions, CNTs should be able to target the cancerous cells to convey the drug to the right target.

Surface functionalizing often times is the best method to achieve this goal. Different surface functionality combined with SWCNT type result in different behavior confronting with the target cell. The growing demand of production and application of engineered nano materials and in particular CNTs is associated with concerns and uncertainties regarding their side effects on human health⁴⁻⁶. On the other hand, CNTs have been utilized for diagnoses and treatment of terminal diseases such as cancer, tumors and so on⁷⁻⁹. Drug delivery vehicles can best describe the CNTs and other nano materials roles when it comes to transfecting proteins¹⁰, peptides¹¹, therapeutic active molecules and nucleic acids¹² into different types of cells. The high near-infrared absorption⁸ and photoacoustic properties¹³ of SWCNTs make them likely tools in the targeting and selective destruction of cancer cells. Despite all these promising potentials of CNTs, their toxicity and the mechanisms by which they interact with cell membranes are not well understood yet⁶. Different synthesis, purification and post processing methods of CNTs result in a vast range of different types and chiralities, which makes it practically difficult to clarify their behavior in contact with, live organs. For example, while in-vitro toxicity of SWCNTs is not yet fully determined¹⁴ while some reports found multiwall carbon nano tubes (MWCNTs) to be nonimmunogenic when functionalized¹⁵. Due to the unlikelihood of synthesizing CNTs with distinct chirality, there are many reports utilizing simulation techniques such as molecular dynamics (MD) to provide better insights on the effect of the CNTs on cell membranes. However, the chirality and surface functionality effects on the interaction with a lipid bilayer membrane has not been investigated in much needed details.

In this dissertation, MD simulations are conducted exploiting the Chemistry at HARvard Macromolecular Mechanics (CHARMM) force filed potential parameters. The cell membrane

comprises both dipalmitoylphosphatidylcholine (DPPC) lipid molecules and water molecules. Surface functionalizing, on the other hand, is of great interest for the researchers. Achieving better water solubility and dispersion could reduce the toxicity of the nano particles, which is one of the motivation of this investigation. Polyethylene glycol (PEG) is a widely used polyether compound in medicine. Being water-soluble polymer it is utilized in most experimental investigations to functionalize different nano materials to address both the higher dispersibility and lower cytotoxicity requirements^{7, 16}. Polyethylene glycol molecules were shown, experimentally, to enhance the penetration of CNTs in the lipid cell membranes⁷. The results of MD computational experiments, investigating SWCNTs -with different length, chirality and surface functionalizing- are presented in chapter 2. Also, the nature of the adhesion energy between the lipid membranes and the CNTs is explained.

1.3. Nano Mechanical Characterization of Negative Stiffness Materials

Depth sensing nano indentation is a contact based technique widely used for evaluation of mechanical properties at very small scales. During a typical test a diamond tip of known geometry is pressed into the sample surface, while the indentation load and depth are continuously recorded. The hardness and elastic modulus are measured in most cases, but other phenomena like pressure-induced phase transformations ¹⁷, incipient plasticity ¹⁸ or time dependent effects ¹⁹ can be studied by analyzing the indentation curve as well. Furthermore, it is possible to perform such test at elevated temperatures and investigate the temperature stability of the material ²⁰ or temperature related phenomena.

The concept of materials and structures with negative stiffness, although not too recent, requires further clarifications in terms of both definition and quantification. It is well understood that a constrained bi-stable structure such as a buckled beam could exhibit negative stiffness under certain circumstances ^{21, 22}. Through negative stiffness one may expect the material/structure to displace opposite to the direction of the applied force. The importance of such materials/structures can be expressed in terms of extremal vibrational damping ²³, composites with infinite stiffness ²⁴, ²⁵ and acoustical absorbers ²⁶. Even more application are still evolving ranging from meta-materials to seismic protection of structures ²⁷ and strings with negative stiffness and hyperfine structure ²⁸.

The design and evaluation of bi-stable structures as negative stiffness elements has been studied in several cases, whereas the investigation for materials with negative stiffness remains limited to the proof of concept. Lakes *et al.* ^{24, 29, 30} showed that materials undergoing certain structural changes, mostly phase transformations, when embedded within a constraining matrix display negative stiffness. They also showed that the concept of the negative stiffness varies fundamentally from the negative Poisson's ratio materials. The overall mechanical properties of the resultant composites changes dramatically when the stimulating factors (temperature in the case of a phase change) reaches the threshold. Lake *et al.* ³¹ reported an infinitely stiff composite of VO₂ 1% –Sn around the phase transition temperature of VO₂ (~66 °C). Furthermore, based on their observation the damping parameter ($\tan \delta$) showed a peak at the same temperature range with a value much greater than best naturally damping materials such as rubber. However, no attempt has been made so far to measure the negative stiffness of these materials directly and report the quantitative value of it. The idea of high temperature nano indentation and temperature induced

phase transformation of the ferroelectric materials motivated the idea of a unique in situ nano indentation experiment for measuring the negative stiffness value. A detailed explanation of this method and the results are presented in Chapter 3.

1.4. Review of the Viscoelasto-plastic Behavior of FRPs

The temperature and rate dependent behaviors of polymeric materials have been reported in the literature³²⁻³⁵. Polymers exhibit a wide range of viscous behavior from brittle elastic to viscoelastic when exposed to different temperatures and/or strain rates. Oftentimes viscous behavior dominates at higher temperatures and increases till passing the glass transition (T_g) where the polymeric chains lose their cross-linked molecular structure and, consequently, the polymer flows viscously. The consequent changes at the microscopic scale lead to alteration of the macroscopic material properties and ultimately affects the composite structure. Figure 1.1 summarizes the main phenomena that take place in composites caused by elevated temperatures.

Modeling of the viscoelastic behavior of polymer matrix composites (PMCs) has been practiced extensively utilizing both macroscopic and microscopic approaches. The applicability of the linear constitutive models to FRPs at relatively low stress levels is well documented³⁶. Several attempts were made to model the nonlinear-viscoelastic/viscoplastic behavior of FRPs using macroscopic approach where the whole composite is considered as an anisotropic homogenous material without taking the individual constituent into account. For example, Gates and Sun³³ utilized a quadratic plastic potential function to model the inelastic behavior of a carbon fiber reinforced thermoplastic polymer. On the other hand, Bordonaro³⁷ modified Krempl's viscoplastic

model³⁸ to better describe the phenomena encountered in reinforced polymers compared to metals where the main body of model initiates from.

In micromechanical approaches, the response of each individual constituent is taken into account when modeling the overall behavior of the composite³⁹. To better predict the cumulative response of the composite, the reinforcement and the matrix are modeled explicitly utilizing numerical methods such as finite element or boundary element analysis⁴⁰. Alternatively, the viscoelastic behavior of laminates having different architectures (symmetrical, cross-plies, etc...) can be predicted by applying a time dependent form of the classical laminate theory (CLT). The third category of modeling schemes is “mesomechanic” where the constitutive models are defined at the ply level rather than constituent levels or cumulative scale⁴¹.

Assuming the FRP to be orthotropic, the time dependent principal strains for a general unidirectional case can be related to the corresponding stresses in the following form assuming that changes in $S_{11}+S_{12}$ are much less than $S_{22}+S_{66}$:

$$\begin{Bmatrix} \epsilon_{11}(t) \\ \epsilon_{22}(t) \\ \epsilon_{12}(t) \end{Bmatrix} = \begin{bmatrix} S_{11} & S_{12} & 0 \\ S_{12} & S_{22}(t) & 0 \\ 0 & 0 & S_{66}(t) \end{bmatrix} \begin{Bmatrix} \sigma_{11}(t) \\ \sigma_{22}(t) \\ \tau_{12}(t) \end{Bmatrix} + \begin{Bmatrix} 0 \\ \epsilon_{22}(t) \\ \epsilon_{12}(t) \end{Bmatrix}_{VP} \quad 1.1$$

Where subscripts 1 and 2 refer to the fiber direction and normal to the fiber direction, respectively and the compliance in the fiber-dominant direction is taken to be time independent. The viscoplastic portion of the strain is denoted by the subscript “VP” which can be linearly added to the overall strain field^{41, 42}. The majority of models at all three scales (i.e., micro, meso and macro-mechanics) incorporate the materials properties within their constitutive equations as

experimentally calculated parameters. Hence, to obtain all of the parameters for a phenomenological model, experimental mechanical testing protocols should be carried out. Upon the successful construction of such viscoelastic-plastic models, one approach to verify the models is simply to compare the model prediction to prolonged creep or stress relaxation tests. In return, the need to validate the models for long durations has motivated many researchers to propose a substantial number of accelerated methods to evaluate the viscoelasto-plastic behavior of materials using the results from tests conducted at considerably shorter time durations. Figure 1.2 highlights the most common methods for creep compliance and delayed failure analysis which are utilized frequently to shorten the prolonged mechanical testing in mesomechanics type analysis ⁴². In the case of relatively small stress (or strain) the time dependent behavior of the composite is described by linear and nonlinear viscoelastic modeling of polymer matrices. When the composite is loaded to a high stress (or strain) the time-dependent behavior of polymers tends to deviate from the predictions of viscoelastic models. This is partly because loading of solid polymers to high stress or high strain levels results in yielding ⁴³ and time-dependent inelastic deformation ^{44, 45}. To describe the time-dependent inelastic behavior of PMCs, phenomenological viscoplasticity models were introduced ^{33, 46}. The deformation of polymeric materials strongly depends on the duration and the rate of loading, and this dependence becomes even more critical as the temperature approaches the glass transition temperature ^{43, 47}.

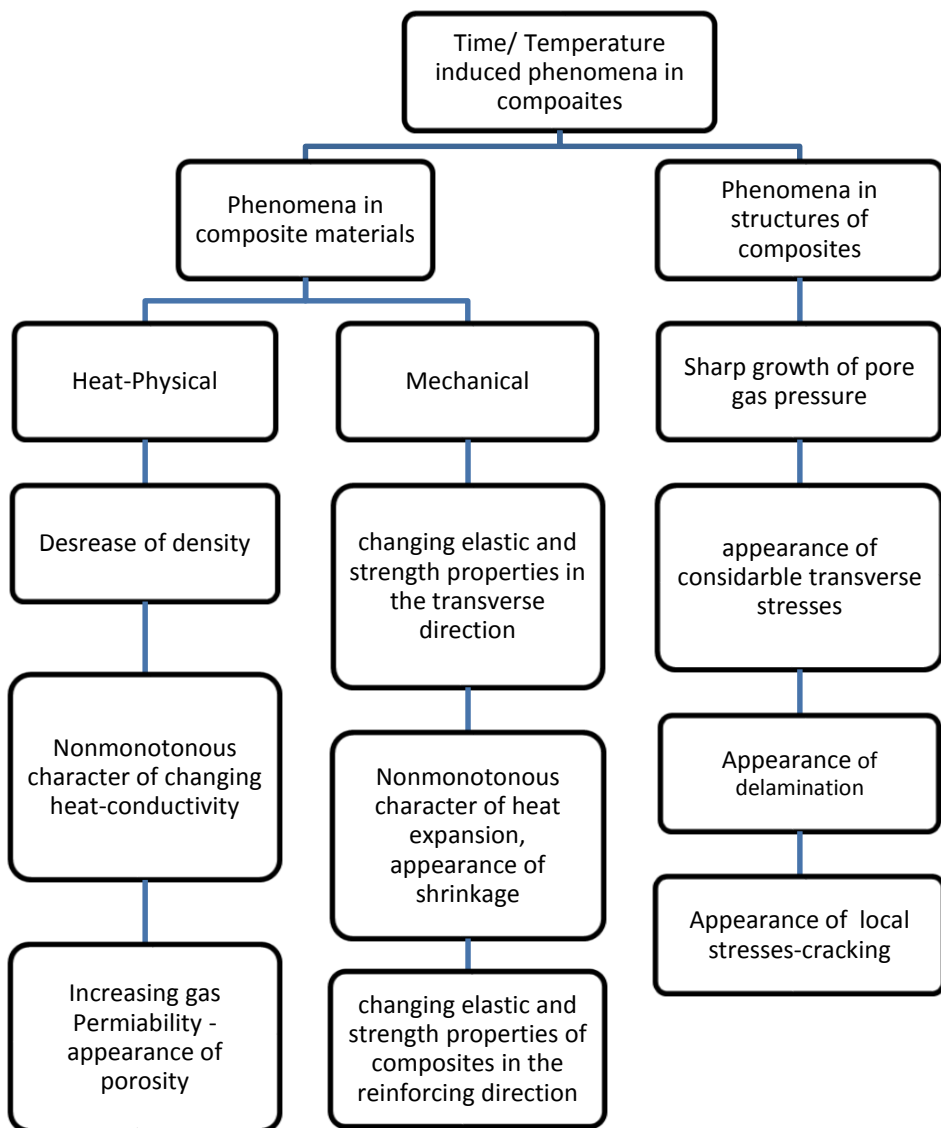


Figure 1.1. The major phenomena in polymer matrix composites induced by high temperature and/or prolonged time⁴⁸.

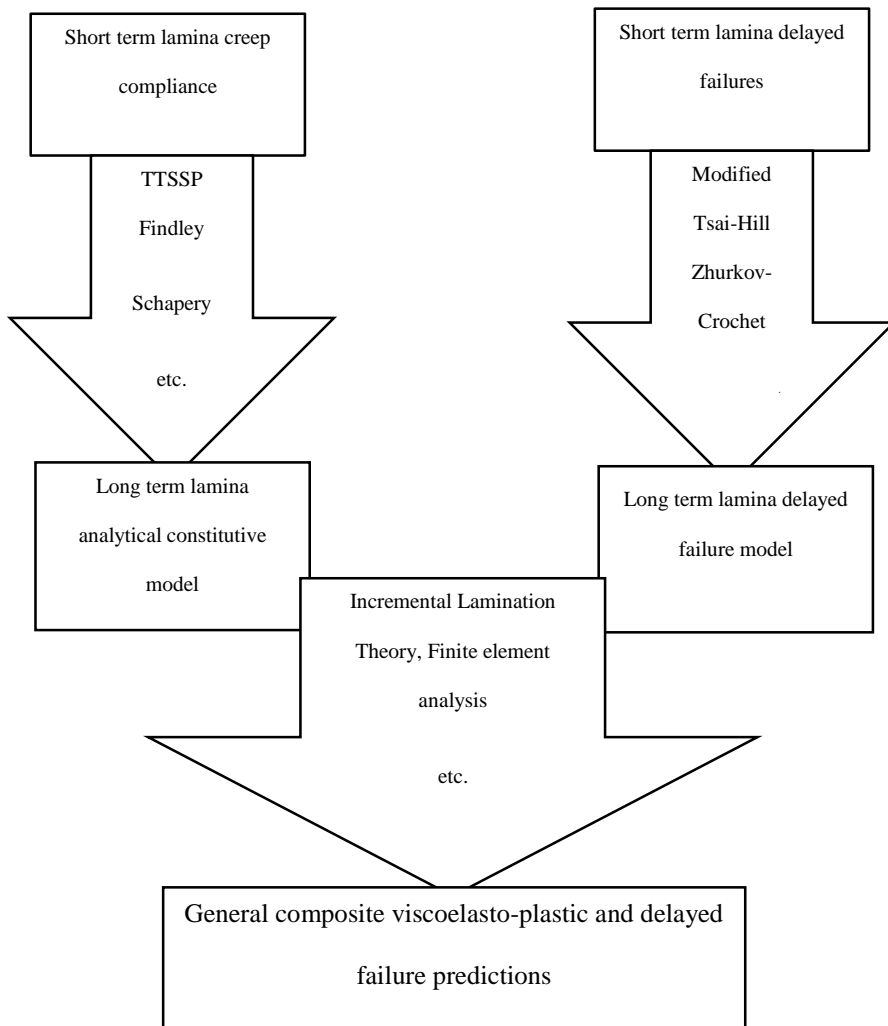


Figure 1.2. Flowchart of the accelerated viscoelastic and delayed failure analysis schemes in polymer matrix composites via the mesomechanics approaches.

The major constitutive models for viscoelastic behavior are as summarized here while some of models are valid for linear part of the viscos response of materials, others can go beyond to predict nonlinear viscoelastic or viscoplastic behavior as well.

1.4.1. Maxwell Model

Maxwell model consists of a viscous damper and an elastic spring in series (Figure 1.3) where the total time dependent strain can be expressed in form of summation of both:

$$\epsilon_{total} = \epsilon_D + \epsilon_S \rightarrow \frac{d\epsilon_{total}}{dt} = \frac{d\epsilon_D}{dt} + \frac{d\epsilon_S}{dt} = \frac{\sigma}{\eta} + \frac{d\sigma}{Edt} \quad 1.2$$

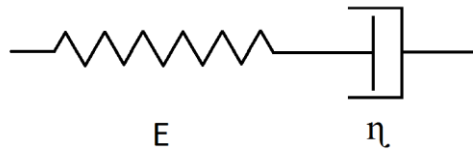


Figure 1.3. Maxwell model representation.

The model predicts the gradual decrease in the stress when a material is subjected to a constant strain, however it postulates a linearly increasing strain when a constant stress is applied which is not the case with most of the polymeric material.

1.4.2. Kelvin-Voigt Model

This model puts the viscous damper and elastic spring into parallel (Figure 1.4), where stress total is sum of each contributor. The model performs satisfactory when a constant stress is applied but it is not realistic when it comes to modeling relaxation.

$$\sigma(t) = E\epsilon(t) + \eta \frac{d\epsilon(t)}{dt} \quad 1.3$$

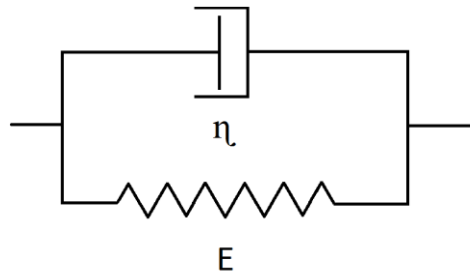


Figure 1.4. Kelvin-Voigt model representation.

1.4.3. Standard Linear Solid Model

As it can be seen from Figure 1.5, the standard linear model consists of a Maxwell element in parallel with a spring. The governing equation of the total strain rate can be expressed as a combination of a Maxwell element and a spring in parallel:

$$\frac{d\epsilon}{dt} = \frac{\frac{E_2}{\eta} \left(\frac{\eta}{E_2} \frac{d\sigma}{dt} + \sigma - E_1 \epsilon \right)}{E_1 + E_2} \quad 1.4$$

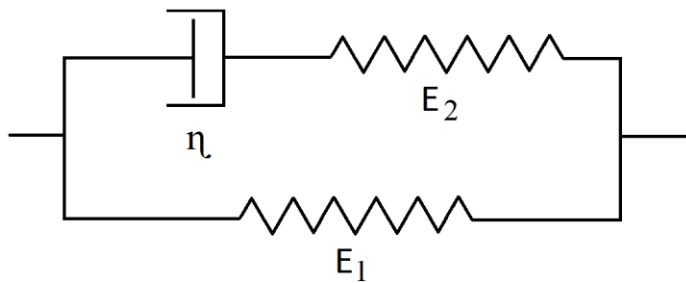


Figure 1.5. Standard linear solid model representation.

The spring in parallel makes up for the instantaneous response of material under stress (stiffness) and the Maxwell element contributes for the viscous time dependent part of the deformation. Even though this model performs better in comparison with the two previous ones, for more complicated material systems it lacks sufficient accuracy.

1.4.4. Generalized Maxwell Model

To yield more accurate results in predicting the viscoelastic response of materials, one can expand the standard linear solid model beyond a spring and Maxwell element by increasing the number of elements in parallel to accommodate for the fact that relaxation does not occur all at once but rather it takes place gradually in a period of time (Figure 1.6).

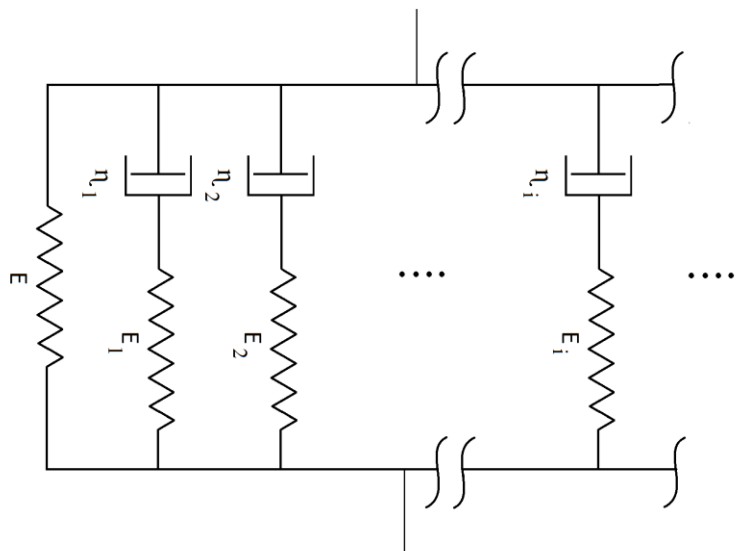


Figure 1.6. Generalized Maxwell model representation.

1.4.5. Time-Temperature-Stress-Superposition Principle (TTSSP)

Both the elevated stress and temperature can lead to a series of accelerated phenomena in deformations of polymer matrix. Taking the amplified deformation mechanisms to be similar in both cases of stress and temperature, one can shift either curves in the *log* time axes to form master curves. In essence, TTSSP is a combination of well-known time-temperature-superposition principle (TTSP) and time-stress-superposition principle (TSSP). Figure 1.7 illustrates schematically the log (time) based superposition. Figure 1.7 (a) & (b) represent a schematic of hypothetical data from short-term creep tests at different temperature and stress levels, respectively. Data from these figures then are shifted horizontally across the *x* axes so that the beginning of the higher stress level/temperature overlaps the previous temperature/stress segment. The shifted curves are then smoothed to form uniform curves of Figure 1.7 (a) & (b). The amount of shift obtained from the curves at different temperatures yields a temperature dependent factor called the temperature shift factor a_T .

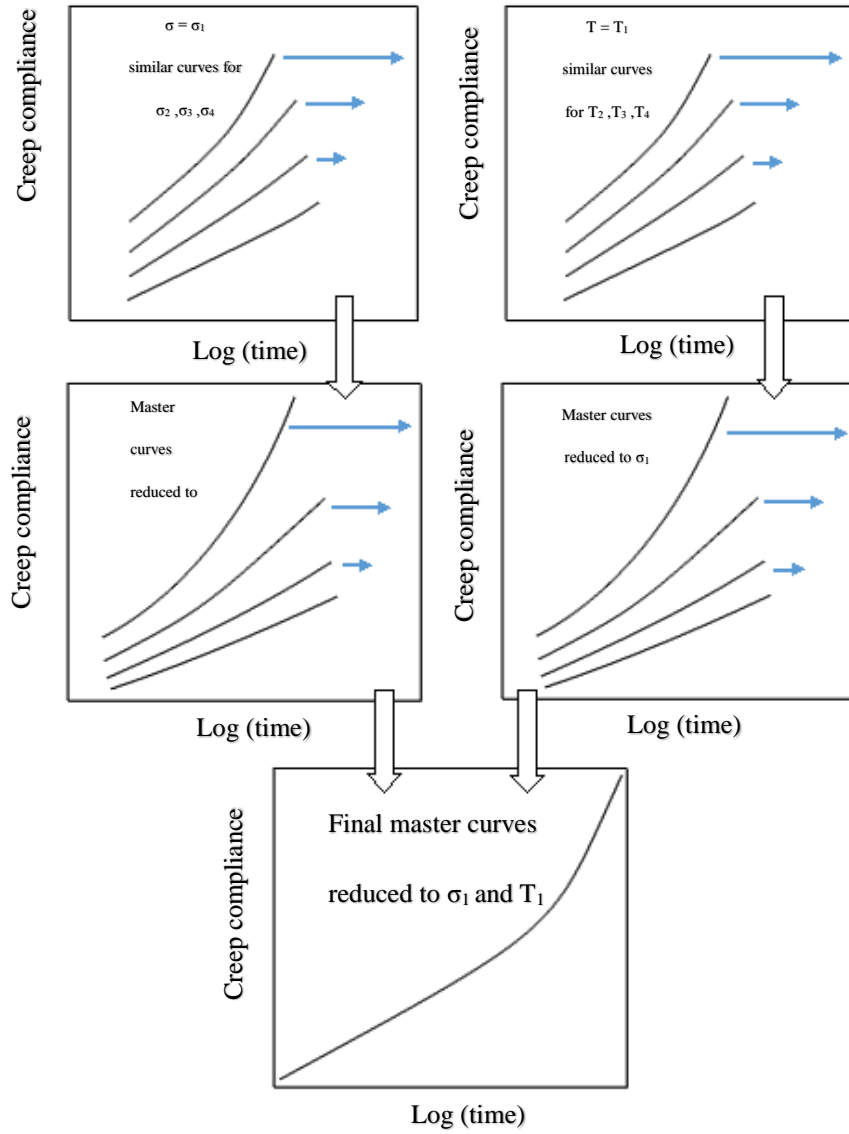


Figure 1.7. Schematic of different superposition principles to yield the final master curve.

A similar approach can be described to how to calculate the stress dependent shift factor such as temperature shift factor a_s which can be calculated from shifting the curves from their initial stress levels. Although there is considerable number of studies on formulating the shift

factors to validate the whole superposition idea, Schapery⁴⁹ has shown that vertical shifts are also necessary to better generalize the TTSSP. In spite of the shortcomings of this approach, it can be adopted to provide a unified master curve where temperature, stress and even moisture can be handled by choosing the appropriate shift factor. On the other hand, the approach is based on graphical shift techniques and there is no general relation to formulate the shift factor, which makes it impractical to incorporate into numerical procedure.

|Chapter 2

2. Nanobiomechanics: Carbon Nano Tubes Penetration into Lipid Membranes*

Abstract: *The ability of carbon nano tubes to enter the cell membrane acting as drug delivery vehicles has yielded plethora of experimental investigations, mostly with inconclusive results due to the wide spectra of carbon nano tubes structures. Due to the virtual impossibility of synthesizing CNTs with distinct chirality, we report a parametric study on the use of molecular dynamics (MD) simulations to provide better insights on the effect of the carbon nano tube chirality and aspect ratio on the interaction with a lipid bilayer membrane as well as their reciprocal effects with surface functionalizing. To boost single walled carbon nano tubes with selective diffusion encroachment, surface functionalizing is adopted in many different experimental attempts. Numerous studies have smeared polyethylene glycol (PEG) as a bio-compatible surfactant to CNTs. The simulation results indicated that a single wall carbon nano*

* A. Alipourskandani, RR. Zeineldin, M. Al-Haik, Langmuir 28(20), 7872-7879 (2012)
Reprinted with permission from Langmuir. Copyright 2012, ACS Publication
A. Alipourskandani, M. Al-Haik, Soft Matter 9(48), 11645-11649 (2013)
Reprinted with permission from Soft Matter. Copyright 2013, RCS Publication

tube utilizes different time-evolving mechanisms to facilitate its internalization within the membrane. These mechanisms comprise both penetration and endocytosis. It was observed that carbon nano tubes with higher aspect ratios penetrate the membrane faster while shorter nano tubes undergo significant rotation during the final stages of the endocytosis. Furthermore, the nano tubes with lower chiral indices developed significant adhesion with the membrane. This adhesion is hypothesized to consume some of the carbon nano tube energy, and thus resulting in longer times for the nano tube to translocate through the membrane. Also, a large scale, full atomistic molecular dynamic simulation was utilized to best disclose the cellular exposure and uptake mechanism(s) of PEG assist functionalized single walled carbon nano tubes (f-SWCNT) into lipid bilayer cell membrane. Results showed that with controlled amount of PEGs attached to a SWCNT the penetration depth and velocity can be controlled throughout the insertion process. Furthermore, the adhesion energy- between the CNT and the membrane- alters considerably in the presence of PEGs with respect to the chirality of nano tubes.

2.1. Introduction

The introduction of nano materials to the biomedical and biotechnological fields had opened a plethora of applications that were not possible before. The need for understanding the interaction of engineered nano materials with live organs; in particular their effect on human health, has been a pressing challenge^{4, 5, 14}. Also, their potential to enhance both determination and medication of several terminal diseases like cancer, tumors and so on are of a great interest and currently is the topic of several undergoing investigations⁷⁻⁹. While the application of CNTs as therapeutic transporters and/or diagnostic are not too recent, growing volume of research is still

undergoing, both experimentally and theoretically, to tailor the different involved factors and better comprehend the phenomenological aspects.

Several emerging technologies seek to employ nano materials as vehicles to deliver molecular probes and drugs into the cells. Carbon nano structures and in particular carbon CNTs are attracting growing attention for therapeutic active molecules delivery. It has been demonstrated that CNTs are capable of delivering proteins¹⁰, peptides¹¹, and nucleic acids¹² to different cells. Single wall carbon nano tubes (SWCNTs) are promising candidates for cancer invasive treatments such as photo-thermal therapies due to their high near-infrared absorption and for drug delivery due to their high diffusivity into cells^{7, 8}. Furthermore, the photo acoustic properties of SWCNTs are utilized for targeting and selective destruction of cancer cells¹³.

Despite all these attractive properties of CNTs, several issues related to their toxicity and the mechanism by which CNTs interact with the cell membranes need to be explored further⁶. For example, while the in-vitro toxicity of SWCNTs is not yet fully determined due to the broad variations in the synthesis and purification methods¹⁴ of these materials, post processing could alter the toxicity of SWCNTs. It was reported that functionalized CNTs display low toxicity and could be modified to be nonimmunogenic¹⁵.

While the CNTs were detected via different means (ex. transient absorption microscopy⁵⁰, Raman spectroscopy⁵¹ and confocal microscopy⁷) to be able to pass through the cell membranes, the mechanisms of the translocation of the CNTs through the phospholipid bilayers and their penetration into cells are yet to be determined. Several hypotheses were developed to explain the mechanism by which CNTs can translocate through cell membranes. The competing scenarios

include: non-specific physical penetration⁵², endocytosis^{53, 54} and spontaneous thermally driven diffusion across the cell membrane^{55, 56}. Kostareols et al.⁵⁷, concluded that functionalized carbon nano tubes (f-CNTs) possess the capacity to intracellularly traffic through the different cellular barriers by energy-independent mechanisms. The cylindrical shape and the high aspect ratio of f-CNTs allows their penetration through the plasma membrane, similar to a '*nano syringe*'⁵⁷. Alternatively, Yaron et al.⁵⁴ attributed the internalization of CNTs into cells to energy-dependent endocytosis. In contradiction, some theoretical investigations provided results indicating that due to their small diameters CNTs may not be able to initiate endocytosis⁵³.

Due to the conflicting findings of several experimental studies, numerical simulations were sought to investigate the mechanics of nano tubes translocation through lipid membranes. Early investigations focused on spherical form of carbon (e.g. fullerenes) interaction with lipid membranes and emphasized the importance of functionalizing the surface to facilitate the adsorption onto bilayer membrane⁵⁸. More recent investigations emphasized the effect of the shape of the particles, their anisotropy and initial orientation to be crucial to the nature of the interaction between the particle and the lipid bilayer membrane. In particular, the contact area between the particle and lipid, and the local curvature of the particle at the contact point are key parameters to trigger the translocation⁵⁹. Several studies employed molecular dynamics (MD) simulation to investigate the interaction of CNTs with lipid membranes. Wallace and Sansom⁶⁰ used coarse-grained molecular dynamics to simulate the penetration of dipalmitoylphosphatidylcholine (DPPC) bilayers by SWCNTs. The simulation showed the lipid lining the inner surface of the CNTs, which suggest that - for drug delivery applications- the therapeutic molecule should be attached to the exterior of the nano tube. Pogodin and Baulin⁵⁵

utilized single-chain mean field theory to calculate the energy required to insert a single CNT in phospholipid bilayer and they found that the energy cost of the bilayer rupture is quite high compared to that of the energy of thermal motion. This conclusion indirectly supports other energy-dependent translocation mechanisms; such as endocytosis. Experimental findings⁶¹ and simulation by another group⁶⁰ concluded that the length and diameter of a CNT are determinant parameters to how far a CNT can travel through cell membranes. While there are numerous publications employing molecular dynamics to simulate the mechanics of CNTs/lipid interaction, fewer investigations took into account the geometry of the CNTs such as the length. Moreover, the majority of the published effort assume a single type of CNTs and neglect a very crucial parameter; the chirality of the CNTs. Understandably, it is rather hard- if not impossible- to grow CNTs in a distinct chirality. Furthermore, extracting and isolating CNTs out of a bundle based on their chiralities is still in its infancy stages⁶²⁻⁶⁵. Therefore, due to the lack of a reasonable method to narrow down the chirality distribution of SWCNTs, experimental parametric investigations to how the chirality affects the CNTs interaction with cell membranes are currently absent. Drug delivery ability of CNTs in general and SWCNTs in particular can be attributed partially to their ability in transfecting through different lipid cell membranes in the human body⁶⁶⁻⁶⁸.

The purpose of this part of the dissertation is to investigate the effect of the length and chirality and surface functionalizing on the dynamic translocation of SWCNTs through a bilayer phospholipid membrane. To this end, MD simulations were carried out for four different SWCNTs chiralities with two different lengths. We also studied the interaction between the nano tube and the membrane qualitatively by probing the possibility of adhesion between the two entities. These simulations shed some light on the effect of CNTs morphologies on their translocation into cells,

which could facilitate future efforts for tailoring the cell uptake of CNTs toward delivering specific quantities of therapeutic molecules or bio probes. CNTs like all other foreign particles once jabbed into the body should first be able to elude the immunological system. Reticuloendothelial system (RES) is a monocular phagocytic organism that can pierce the alien objects (pathogen) from blood stream by identifying blood serum components (opsonins) attached to them. Thereafter, more than 60 lysosomal enzymes and oxidative chemicals attack the opsonized particle for degradation^{7, 69}. Immunogenicity and nonspecific uptake of CNTs encumber their drug delivery mission which most of the times can be fixed by surface functionalizing⁷⁰. SWCNTs are potential vehicles that can be easily convened with chemical functionalities to carry biomolecules such as proteins, DNA and RNAi^{66, 67, 71}. Based on clinical studies different functionalizing agents enhance both better attachment of biomolecules to SWCNTs and reduce their cytotoxicity by better dispersion in water⁷¹. An antibiofouling surface for increased circulation uptake and decreased non-specific interaction is entailed for application of therapeutic nano particles. Polyethylene glycol (PEG), is a widely used polyether compound in medicine and as a water soluble polymer is utilized in most experimental investigations to functionalize different nano particles to address both higher dispersibility and lower cytotoxicity issues^{7, 16}. However, due to the unsophisticated characterization techniques for tracking down the particles *in vivo*, most of the knowledge earned so far is limited to clinical observations and ensuing symptoms in animals. This makes it inconclusive to determine the phenomenological aspects of both functionalization and functionalized particles interactions in the body. It is of pivotal importance to understand the mechanism of cell internalization, trafficking and excretion of surface-modified SWCNTs to breed them as safe and applicable nano drugs.

Non-specific physical penetration of the cell membrane, endocytosis or combination of both are some hypothesis by which the uptake phenomena is explained so far in the literatures^{72, 73}. The eccentric conclusions obtained by experimental studies - mainly due to cavalier characterization techniques and error imposed by diagnostic tools - boost the implication of realistic simulation techniques such MD. Molecular dynamics have been extensively exploited to mimic the SWCNT/cell membrane interaction in relatively short time interval so far and revealed appealing facts about CNTs' internalization through cell membranes⁷³⁻⁷⁶. Few studies have published so far concerning the functionalization effects on the transfection of CNTs into cell membranes utilizing atomistic scale simulation techniques^{74, 75, 77}. Hence, this part of the dissertation reports the results of a large-scale full atomistic MD study on the effect of two interfacial properties of SWCNTs on their cell internalization. Mutual effects of SWCNT's chirality and surface functionalizing with covalently bounded PEG chains are investigated. Three different chiralities were chosen with identical total electrical charge and length with and without PEG chains attached to them.

2.2. Force Field Selection

The Chemistry at HARvard Macromolecular Mechanics (CHARMM27)^{78, 79} all-atom force field represents a highly-optimized empirical model valid for investigating nucleic acids, proteins, and lipids, allowing for simulation studies of heterogeneous systems via empirical force field calculations^{80, 81}. Equation 2.1 describes the functional form of the potential energy calculated by CHARMM27:

$$\begin{aligned}
E = & \sum_{bonds} k_b(b - b_0)^2 + \sum_{UB} k_{UB}(S - S_0)^2 + \sum_{angles} k_\theta(\theta - \theta_0)^2 \\
& + \sum_{dihedrals} k_\phi[1 + \cos(n\phi - \delta)] + \sum_{impropers} k_\omega(\omega - \omega_0)^2 \\
& + \sum_{nonbond} \epsilon \left[\left(\frac{R_{minij}}{\tau_{ij}} \right)^{12} - \left(\frac{R_{minij}}{\tau_{ij}} \right)^5 \right] \\
& + \frac{q_i q_j}{\epsilon_1 \tau_{ij}}
\end{aligned} \tag{2.1}$$

where K_b , K_{UB} , K_θ , K_ϕ , and K_ω are the bond, Urey-Bradley, angle, dihedral angle, and improper dihedral angle force constants, respectively; b , S , θ , ϕ , and ω are the bond length, Urey-Bradley 1,3-distance, bond angle, dihedral angle, and improper torsion angle, respectively, with the subscript zero representing the equilibrium values for the individual terms. In the dihedral term n is the multiplicity and δ is the phase, which dictates the location of the minima and maxima. Coulomb and Lennard-Jones 6-12 terms contribute to the external or nonbonded interactions; ϵ is the Lennard-Jones well depth and R_{min} is the distance at the Lennard-Jones minimum, q_i is the partial atomic charge, ϵ_1 is the effective dielectric constant and r_{ij} is the distance between i and j atoms⁸¹. Numerous investigations with adaptive improvements have turned CHARMM27 into one of the most utilized force fields for MD simulations of biomolecules⁸⁰⁻⁸³.

2.3. Chirality of SWCNT

The chirality, defined by the chiral vector \vec{C}_h and the chiral angle θ (briefly described here for completeness), characterizes the atomic structure of a SWCNT. They are also called the roll-up vector (that defines its diameter), and the helical angle respectively. The chiral vector, $\vec{C}_h = n\vec{a}_1 + m\vec{a}_2$, is defined on the honeycomb lattice of carbon atoms by unit vectors \vec{a}_1 and \vec{a}_2 (shown in Fig. 1), and the integers (n, m) which represent the number of steps along the zigzag carbon bonds of the hexagonal lattice. The chiral angle is the smallest angle enclosed by the nano tube axis and the row of edge-sharing hexagons, or, in other words, the smallest angle between the circumference line (chiral vector) and the primitive lattice vector (zigzag direction) on the hexagonal sheet as shown in Figure 2.1. A SWCNT can be visualized as a sheet of graphite, marked by bold lines in Figure 2.1, rolled into a tube such that the tip of the chiral vector touches its tail. The nano tube configurations where the chiral angles assume the extreme values of 0° and 30° are the limiting cases referred to as "zigzag" and "armchair", respectively. In terms of the chiral vector, the zigzag nano tube is defined as $(n, 0)$ and the armchair nano tube as (n, n) respectively. The chiral angle θ may be viewed as a measure of the twist in the tube, and this chirality dictates the nano tube diameter⁶¹.

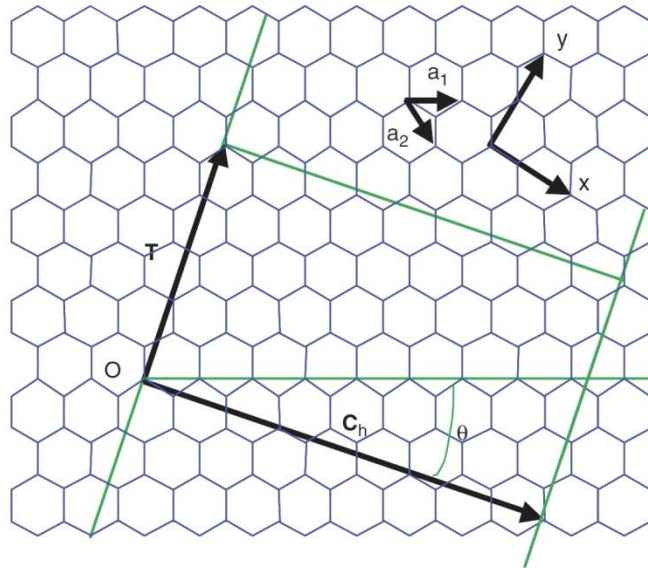


Figure 2.1. Schematic illustration of the chiral angle and chiral vector.

Single wall carbon nano tubes can also be defined by the diameter D_n and the chiral angle θ which themselves can be obtained uniquely by the integer pair (n, m) :

$$\theta = \pi \tan^{-1} \left(\frac{\sqrt{3m}}{2n + m} \right) \quad 2.2$$

$$D_n = \frac{\sqrt{3}}{\pi} b \sqrt{n^2 + m^2 + nm} \quad (0 \leq m \leq n) \quad 2.3$$

Where b is the C–C bond length ($\sim 0.142\text{nm}$). The thermal⁸⁴, electrical⁸⁵, and mechanical⁸⁶ properties of SWCNTs vary substantially depending on the SWCNTs diameters and chiral angles.

2.3.1. Numerical Experiments

The membrane cell in the current study comprises 72 dimyristoyl-sn-glycerophosphatidylcholine (DMPC) lipids, -a common membrane lipid^{87, 88-} and 2716 water molecules making an overall 17,796 atoms structure. To investigate the effect of chirality and length separately, eight SWCNT configurations were assembled. The morphologies comprised four short SWCNTs with (10, 0), (10, 5), (10, 7) and (10, 10) chiral indices. Four longer nano tubes -double the length of the short ones- with identical chiralities were generated to investigate the effect of the nano tubes length on translocation through the membrane.

To ensure the applicability of the CHARMM27 force field for both constituents, we analyzed the C-C bond in the lipid chains, the C-C bond within the body of the tubes, and the C-C bonding at the open ends of the SWCNTs. We noticed significant difference between the behavior of the carbon atoms located at the ends and at the body of the SWCNT. The number of the nearest neighbors (only 2) at the SWCNTs open ends is less than that for the body atom (3), and carbon atoms at the ends are unsaturated. The unsaturated boundary effect can be avoided by adding hydrogen atoms to the open ends of the CNT^{89, 90}. This practice in effect accounts for the cap's effect of the CNTs and was employed reasonably by several groups^{90, 91}. The exact numbers of carbon and hydrogen atoms for each chiral nano tube are presented in Table 2.1.

Table 2.1. Total number of atoms utilized in MD simulation for chiral nano tubes.

		H atoms	C atoms	Nano tube diameter (nm)	Nano tube length (nm)	Chiral Angle θ°
(10,0) NT-zigzag	short	40	600	0.783	6.5541	0.00
	long		1280		13.472	
	short	50	600	1.036	5.2281	19.11
	long		1300		10.972	
(10,7) NT	short	54	600	1.158	4.8061	24.18
	long		1308		10.212	
	short	60	600	1.356	4.1278	30.00
	long		1320		8.932	

Upon investigating the force field compatibility for this enforced C-H bonding we found that the “standard” CHARMM27 force field does not account for two missing bending angle parameters between the carbon atoms of nano tube and the added hydrogen. Since these force fields are largely empirical, we assigned the appropriate values for these two parameters from an analogous C-H bond types in a classical force field; molecular mechanics (MM3) force field. The MM3 force field is mostly used for hydrocarbon structures⁹²⁻⁹⁴ rather than biomolecules.

Having passed the force field compatibility test, the functionalized SWCNTs were placed -individually- above the center of mass of the membrane aligned with its Z axe. A two angstrom (2\AA°) clearance was maintained in all configurations preventing the tube from interacting with the membrane while carrying out the minimization step. The simulations were carried out using TINKER[®]; a general purpose package of molecular dynamics simulation subroutines ⁹⁵. Prior to the dynamic step, all the numerically generated microstructures were relaxed through the numerical minimization of the potential energy with BFGS quasi-Newton algorithm to a convergence criterion where the RMS per atom force cutoff of the energy is equal or less than 1 Kcal/mol Å. For example, for a long (10, 5) SWCNT the initial simulation box dimensions were set at approximately $109.009 \times 24.713 \times 14.145 \text{ \AA}^3$ and upon the relaxation of the molecule the simulation box size was found to be $113.000 \times 28.000 \times 16.000 \text{ \AA}^3$. The individual SWCNTs and the membrane were minimized both before and after assembling them together.

The assembled SWCNT/membrane simulation cells were obtained by equilibrating the system after combining the two structures. This equilibration is conducted by enforcing the Newton's equation of motion:

$$F_i = m_i \frac{d^2 r_i}{dt^2} = -\partial \frac{E(r_1, r_2, \dots, r_N)}{\partial r_i} \quad 2.4$$

where m_i is the atomic mass of the i -th atom. Successive configurations of the system are generated by the time integration of equation. 2.4. The result is a trajectory that specifies how the positions and velocities of the particles in the system vary with time. A statistical ensemble is used to compute the average of the physical quantity of interest. The physical quantity is taken as the time average on the trajectory. Statistical mechanics relates MD averages to their thermodynamics

counterparts, and the ergodicity hypothesis can be invoked to justify equating the trajectory averages to ensemble-based thermodynamic properties^{96 97}.

For each SWCNT/membrane system, we conduct a separate molecular dynamics simulation for 60 pico-seconds (ps), with MD time step of 1.0 femto-second (fs) under constant temperature of 300 K and external pressure of 1.0 atm. Unlike previous investigations⁶⁰, we did not apply a steered molecular dynamics (SMD) where an explicit external velocity is imposed to pull the nano tube through the bilayer. Rather, we relied on the statistical thermodynamics ensembles to rescale the velocities of the system particles to achieve a thermodynamic equilibrium. This scenario is closer to most of the experimental investigations mentioned earlier; no external field was applied to enforce the CNT translocation within the membrane. All of the MD simulations were performed within the framework of the canonical statistical ensemble (NVT)⁹⁸, which is characterized by a fixed number of atoms, N, a fixed volume, V, and a fixed temperature, T. Berendsen thermostat was used for the temperature control in the box. The numerical integration of the equation of motion was performed using the velocity Verlet algorithm. The integration time step was 1.0 fs, and the cutoff distance for the 12–6 Lennard–Jones potential was set to 9.0 Å.

2.4. PEGylated SWCNTs

The formulation and precise control of the targeting ligand density on the surfaces of therapeutic nano particles is crucial due to their additional effect on the ‘stealth’ surface of nano particles. On the other hand, the effectiveness of the obtained bundles highly depends on the binding mechanisms of these ligands to the surface of nano particles. Higher blood circulation times were achieved when PEG chains attach covalently to the CNTs compared to those with

surface-absorbed mechanism^{71, 99}. Figure 2.2 illustrates the two common intermediary chemical bonding between PEG chains and SWCNT. Experimentally, both bonding types can be practiced either by application of pristine materials after strong acid treatment or 1, 3 dipolar cycloaddition reaction⁶⁹. The common form of functionalizing is the former one where usually oxidation happens in an oxidizing agent such as piranha solution (mixture of sulfuric acid and hydrogen peroxide) or nitric acid.

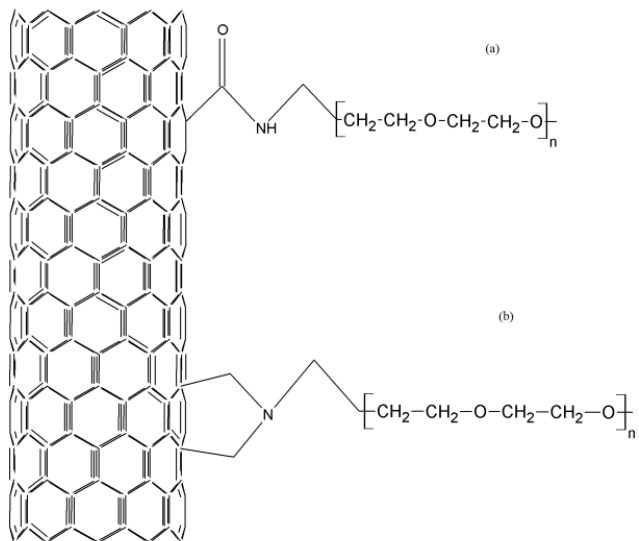


Figure 2.2. Common PEG-SWCNT intermediary chemical bonding, a) through carboxylic acid groups and b) through 1, 3 dipolar cycloaddition reactions.

2.4.1. Numerical Experiments

Molecular dynamics simulations were conducted utilizing the CHARMM27⁸² force field and the message-passing parallel GROMACS4.5.5 simulation package¹⁰⁰⁻¹⁰². The cell membrane comprised both 8580 dipalmitoylphosphatidylcholine (DPPC) lipid residues and 16296 water

molecules 103 , making up a 106776 atom structure in total (without taking the SWCNTs into account). To investigate the effect of chirality, equal length SWCNTs with (5, 5), (10, 0) and (10, 10) chiralities were generated and placed on top of the lipid bilayer membrane at a 2 \AA° clearance aligned perpendicular to the membrane. To probe the effect of the surface functionalizing, PEG single chain molecules ($n=1$) were covalently attached to the SWCNTs via a carboxylic acid groups (Figure 2.2-a). All SWCNT in the simulations maintained the same electrostatic charge and a fixed PEG density for the functionalized-SWCNTs (f-SWCNT). Figure 2.3 shows the position and density of PEG ligands attached to a (10, 0) SWCNT which was geometrically optimized to attain the minimum potential energy level and, hence, the most stable configuration.

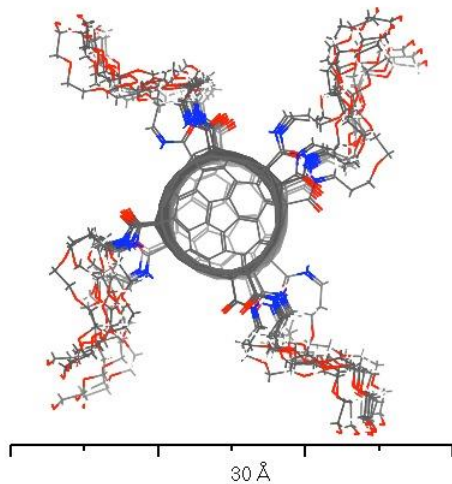


Figure 2.3. A top view from the assumed structure for a (10, 0) f-SWCNT.

The as built structures were geometrically optimized by minimizing their potential energy function via the steepest decent method. Molecular dynamic simulations were then conducted under canonical (NVT) thermodynamic ensemble to best describe the *in-vivo* environment of

living cells for 100 ps with 1 fs time integration intervals. Temperature convergence to the pre-set physiological temperature of 320°K was monitored using Berendsen thermostat^{98, 104}.

2.5. Results and Discussion

Plotted in Figure 2.4 and Figure 2.5 are the minimum potential energies per atom for the relaxed individual SWCNTs and the bilayer membrane achieved through the LM-BFGS minimization algorithm. The chirality seems not to influence the change in the potential energy for the short nano tubes as much as the nano tube length does. Doubling the length of the nano tube increased the equilibrium potential energy of the membrane/CNT systems by three folds, Figure 2.5.

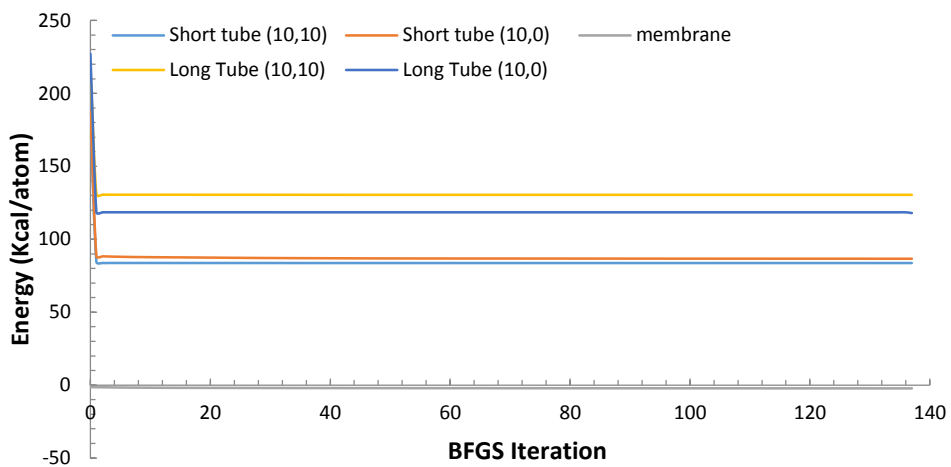


Figure 2.4. Energy minimization for the different SWCNTs and the bilayer membrane.

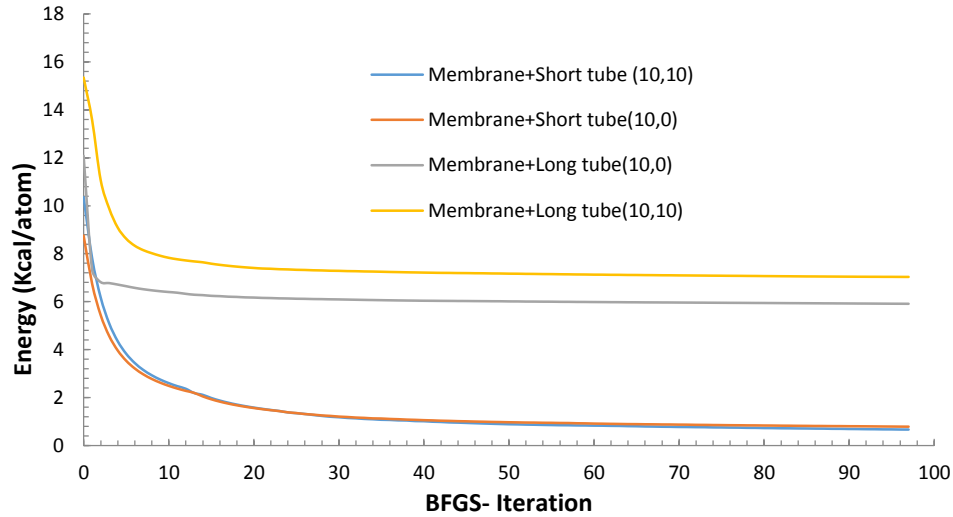


Figure 2.5.Energy minimization data for some of the SWCNT/membrane assembled configurations.

2.5.1. Effect of SWCNT Length

The relaxed SWCNT/membrane systems were equilibrated further by conducting MD simulation under NVT ensemble. The evolution of the potential energy for the two systems based on short and long zigzag and armchair nano tube systems are shown in Figure 2.6 and Figure 2.7, respectively. The relation between the approximation inherent in the velocity Varlet integration algorithm and the fluctuation in potential energy is discussed by Leach ⁹⁷ [pp. 359] where he indicates that a variation of the potential energy in the range 0.001-0.01 kcal/atom is generally considered acceptable as an equilibrium criterion. Since the change in potential energy beyond 60 ps is found to be about 0.004 kcal/atom, the system could be reasonably assumed to have reached equilibrium. Therefore, in the interest of computational time, the simulations were terminated at 60 ps.

Although the number of atoms is almost identical, regardless of the length, the SWCNT with smaller chiral indices (zigzag) always attained the highest total energy, as its slenderness allows more interactions with the membrane during the dynamic simulations. Increasing the length further, contrasted this observation, Figure 2.7, as the SWCNT aspect ratio was doubled.

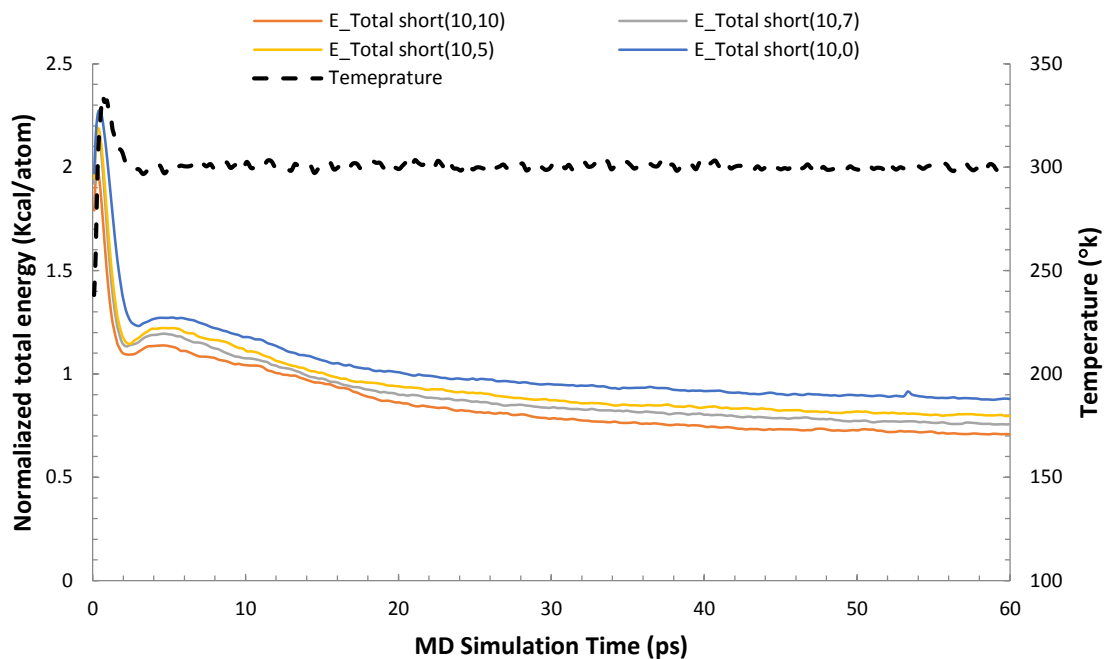


Figure 2.6. Normalized total energy and temperature evolutions during the molecular dynamic simulation of short SWCNTs.

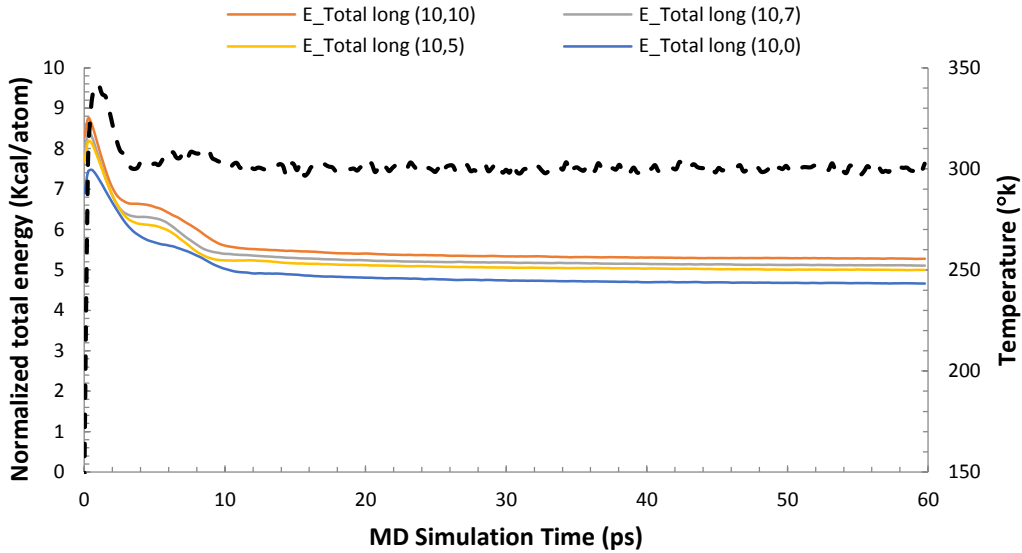


Figure 2.7. Normalized total energy and temperature evolutions during the molecular dynamic simulation of long SWCNTs.

Investigating the trajectories of the different configurations at different peaks of the energy evolution curves (the energy peaks shown in Figure 2.7) can provide useful insights on the SWCNT/membrane interactions. Figure 2.8 shows several MD snapshots at different simulation times for the eight SWCNT/membrane configurations. The first observation is that the mechanism of insertion comprises pure penetration at early stages (times within 0.4 ps), a mix of penetration and endocytosis in between 0.4-10 ps and mostly dominated by endocytosis at later stages (10-60 ps). Holding the chirality fixed, longer nano tubes find their ways through the membrane faster with less rotation from the vertical position. On the contrary, tubes with length shorter than thickness of membrane (i.e.~60 Å) are more likely to rotate in the membrane while trafficking via

endocytosis mechanism. The rotation of short nano tubes in relatively thick membranes was previously reported ¹⁰⁵.

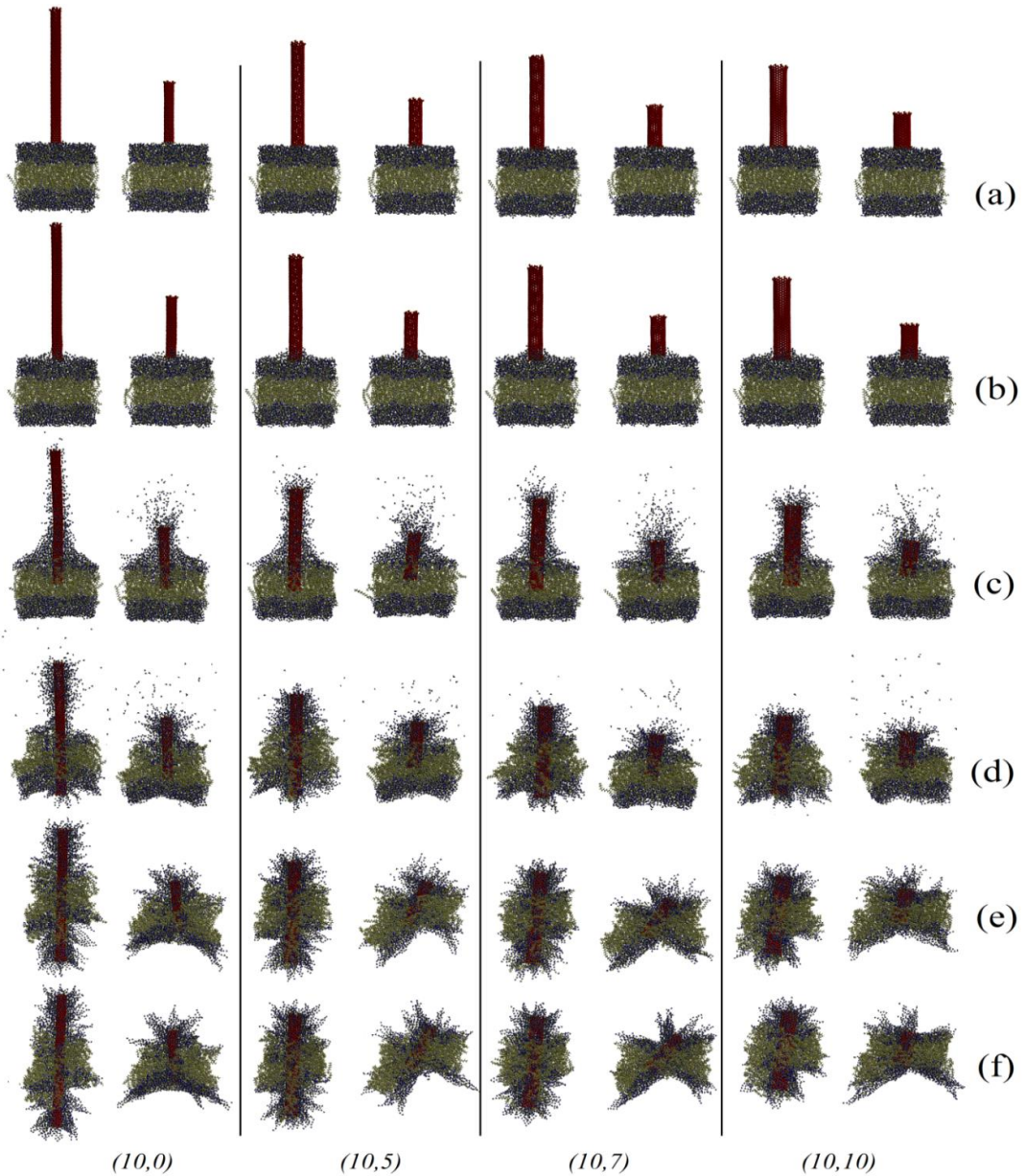


Figure 2.8. Sequential representation of SWCNTs penetration through cell membrane: (a) Initial configuration, (b) after 0.4 ps, (c) after 4 ps, (d) after 10 ps, (e) after 30 ps, and (f) after 60 ps.

2.5.2. Effect of the SWCNT Chirality

Long SWCNTs were chosen to probe the chirality effect. Figure 2.9 shows the trajectory of the bottommost carbon atom -of each SWCNT- from starting point (i.e $z = \sim 62 \text{ \AA}$) to complete insertion when the SWCNT lower end moves out the second layer of the membrane (i.e. $z = 0\text{\AA}$). The results suggest that SWCNTs with lower chirality indices and aspect ratio penetrate faster. On the other hand wider and shorter tubes, with larger surface interaction, tend to rotate.

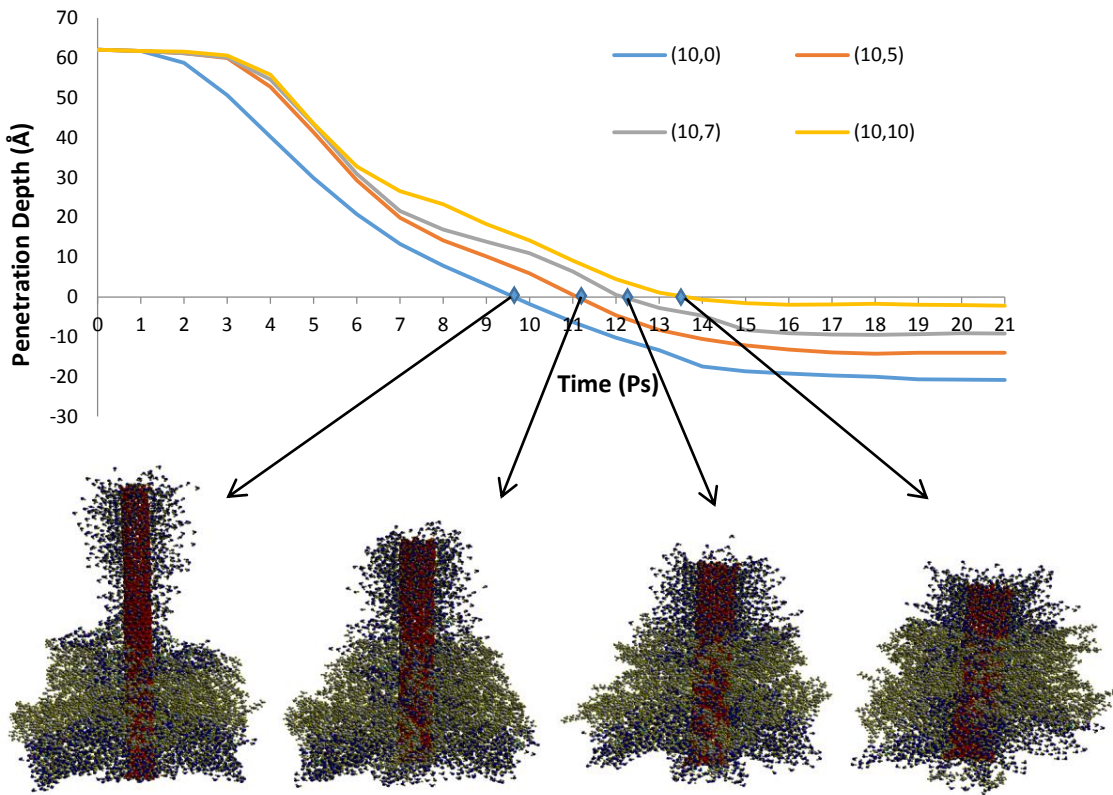


Figure 2.9. Molecular dynamic evolution of the z-coordinate of bottommost carbon atom in different chiralities.

2.5.2.1. Adhesion Energy

The adhesion energy is estimated as the difference between the potential energy of the SWCNT/membrane system and the sum of the potential energies for the membrane and the corresponding SWCNT: $\Delta E = E_{total} - (E_{CNT} + E_M)$, where E_{Total} is the total potential energy of the integrated cell comprising SWCNT/membrane at the end of equilibration, E_{CNT} is the energy of the nano tube alone, and E_M is the energy of the membrane alone. Both E_{CNT} and E_M were pre-calculated via separate MD simulations using the NVT ensemble to calculate the final potential energy after 60 ps.

Figure 2.10 depicts the adhesion energy per atom of the different membrane/CNT configurations versus the corresponding chirality of the nano tube. Obviously, for the same chiral indices, system based on longer SWCNTs will attain higher adhesion energy merely for the increased surface area. It is clear that the adhesion energy attains the highest value for the armchair nano tube system while the zigzag nano tube system achieves the least adhesion energy. These results can be better understood by referring to Figure.6. By the end of the 60 ps all the short nano tubes regardless of their chirality were completely surrounded by the membrane and thus all of them create more or less equivalent interactions with the membrane. However, upon doubling the lengths of the CNTs, nano tubes with higher chiral indices (e.g. (10,10) and (10, 7)) were completely surrounded by the membrane by the end of the 60 ps while those with lesser chiralities (e.g. (10, 0)) were partially encapsulated and thus encountered partial interactions with the membrane leading to lesser adhesion. Hence, a higher chirality SWCNT establishes more interaction (mostly VW and columbic) with the membrane leading to a better adhesion.

Interestingly, the (10, 5) chiral SWCNT seems to attain the lowest adhesion energy with the membrane regardless of the length of the SWCNT, which might suggest the existence of an optimal chirality/length combination. This will be explored further in a future investigation by trying other chiralities, analogous to the (10, 5) in diameter.

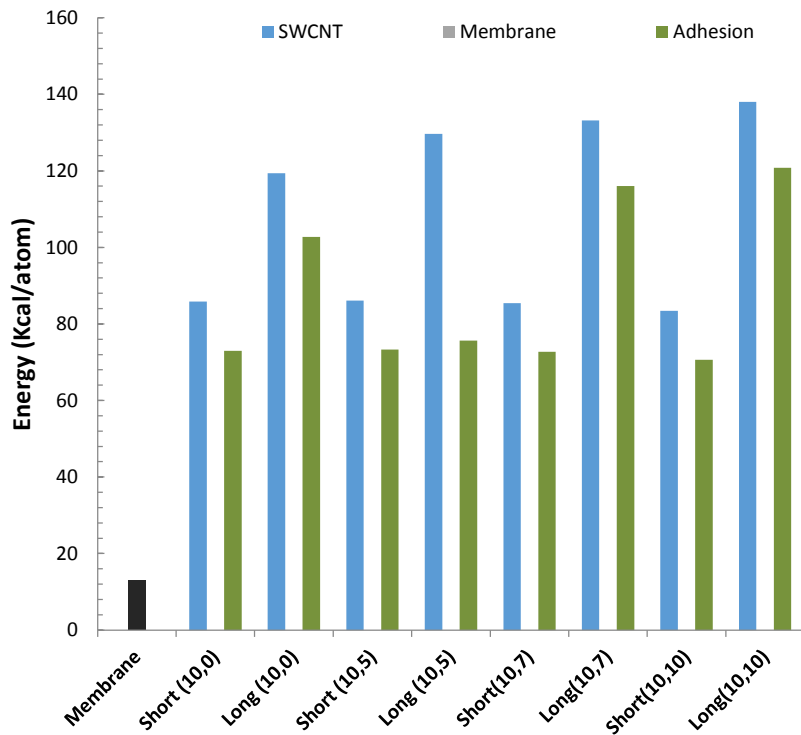


Figure 2.10. Adhesion energy of the different SWCNTs/membrane configurations.

2.5.3. Effect of Surface Functionalizing

Figure 2.11 depicts the potential energy per atom of each configuration calculated throughout steepest decent minimization algorithm. Adding the PEG functionalizing ligands

increased the energy per atom of the system for the as constructed system and they maintained their higher energy after the minimization as well.

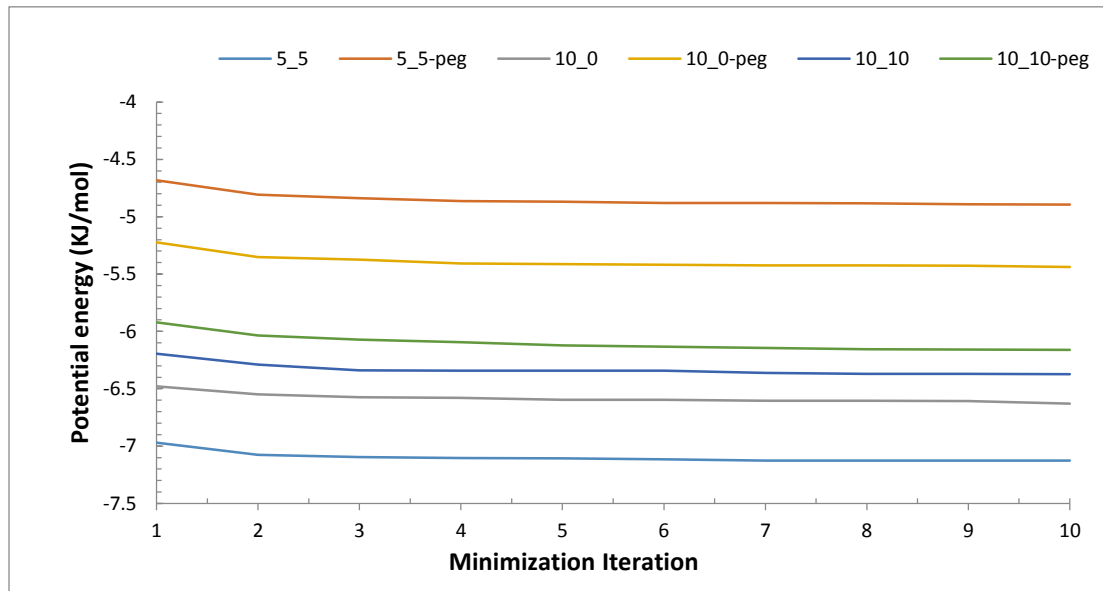


Figure 2.11. Energy minimization evolution for different configurations.

The geometrically optimized SWCNT/membrane and f-SWCNT/membrane systems were further equilibrated by running dynamic steps utilizing NVT ensemble and equilibrating the whole system with an external thermal bath at 320 K. Figure 2.12 shows both the total (potential +kinetics) energy per atom of the systems as well as their temperature evolution during the 100 ps of dynamic run. The f-SWCNT with (5, 5) chirality-which is a representative of a narrow diameter tube- has the highest energy peak followed by the greatest energy level in minimization step as well (Figure 2.11). Energy plots for the studied cases reflect a relatively stabilized regime with a narrow variation interim after almost 50 ps where it reaches the convergence criteria of 0.001-0.01 kcal/atom⁷³.

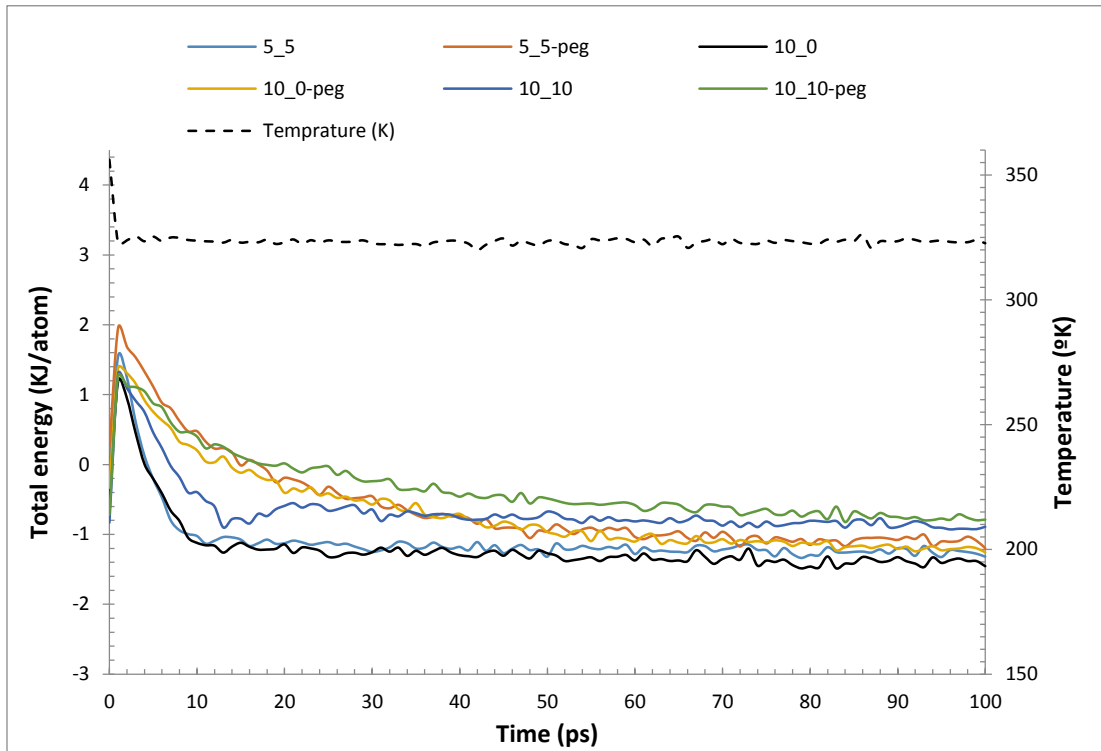


Figure 2.12. The evolution of total energy during the MD run.

Trajectories of the different configurations at different time intervals are investigated to reveal the governing mechanism(s) of SWCNT and f-SWCNT internalization through bilayer lipid membrane. The schematic represented in Figure 2.13 for all three examined chiralites at 5, 10, 15, 50 and 100 ps snapshots verifies the chirality dependence of SWCNTs penetration which we have previously reported with much smaller system and shorter time⁷³. The lower chiral tubes find their ways through bilayer lipid faster in a given length and electrostatic charge, this is similar to the behavior of varying length SWCNT made of equal number of atoms⁷³. Figure 6 illustrates another set of snapshots at 30, 40, 45, 50 and 100 ps from the f-SWCNTs penetrating through membrane.

It can be inferred that the similar pattern governs the precedence of f-SWCNTs trafficking as it reigns the SWCNTs.

Comparison of SWCNT and f-SWCNT side by side at a given chirality highlights the interesting/fundamental differences in their internalization phenomena. Both SWCNTs and f-SWCNTs enhance multiple mechanisms to find their way through the lipid membrane, which consists of penetration in the early stages to endocytosis-dominated insertion in the last stages.

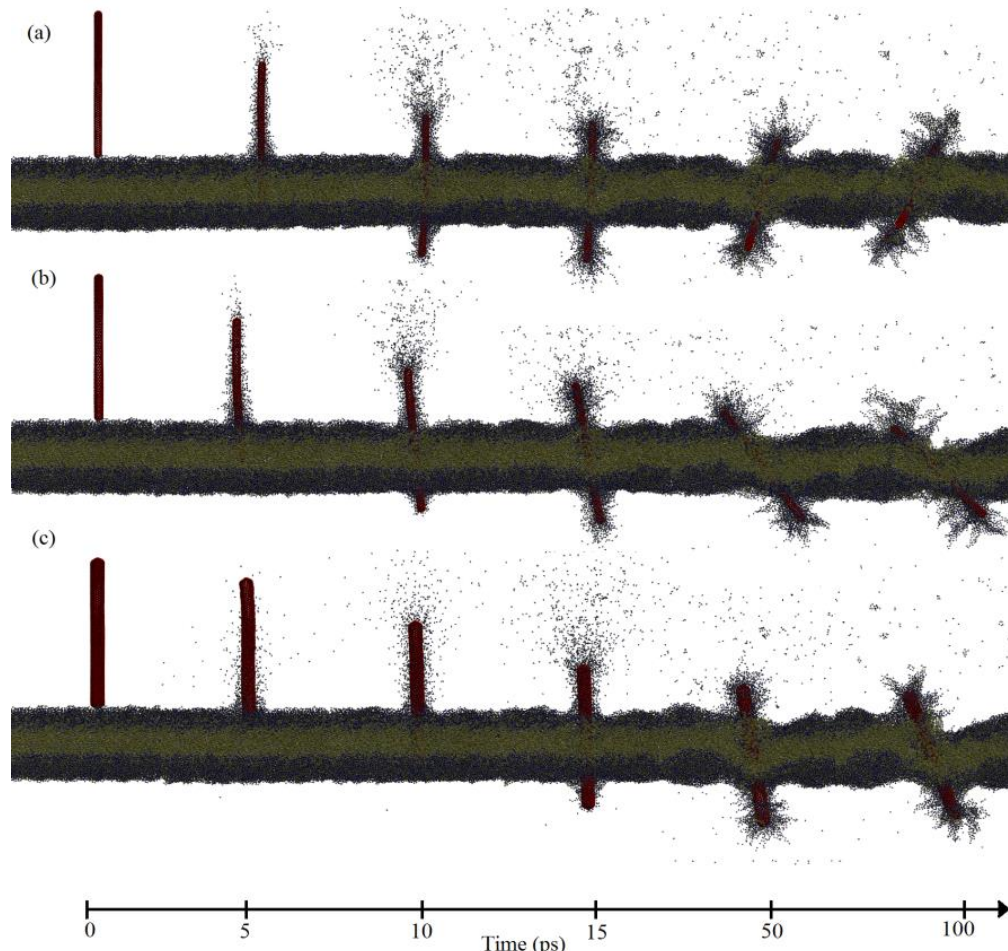


Figure 2.13. Schematic representation of SWCNTs penetrating into lipid membrane, a) (5, 5), b) (10, 0), c) (10, 10) chiralities.

However, revisiting Figure 2.13 and Figure 2.14 can help us shed more light on the infiltration mechanism(s) of SWCNT vs. f-SWCNT. It can be perceived that SWCNT tends to exhibit a more penetration-like internalization, whereas the f-SWCNT follows a prevailing endocytosis path. Less destruction and more bending and stretching is imposed to membrane by f-SWCNTs than SWCNT counterparts.

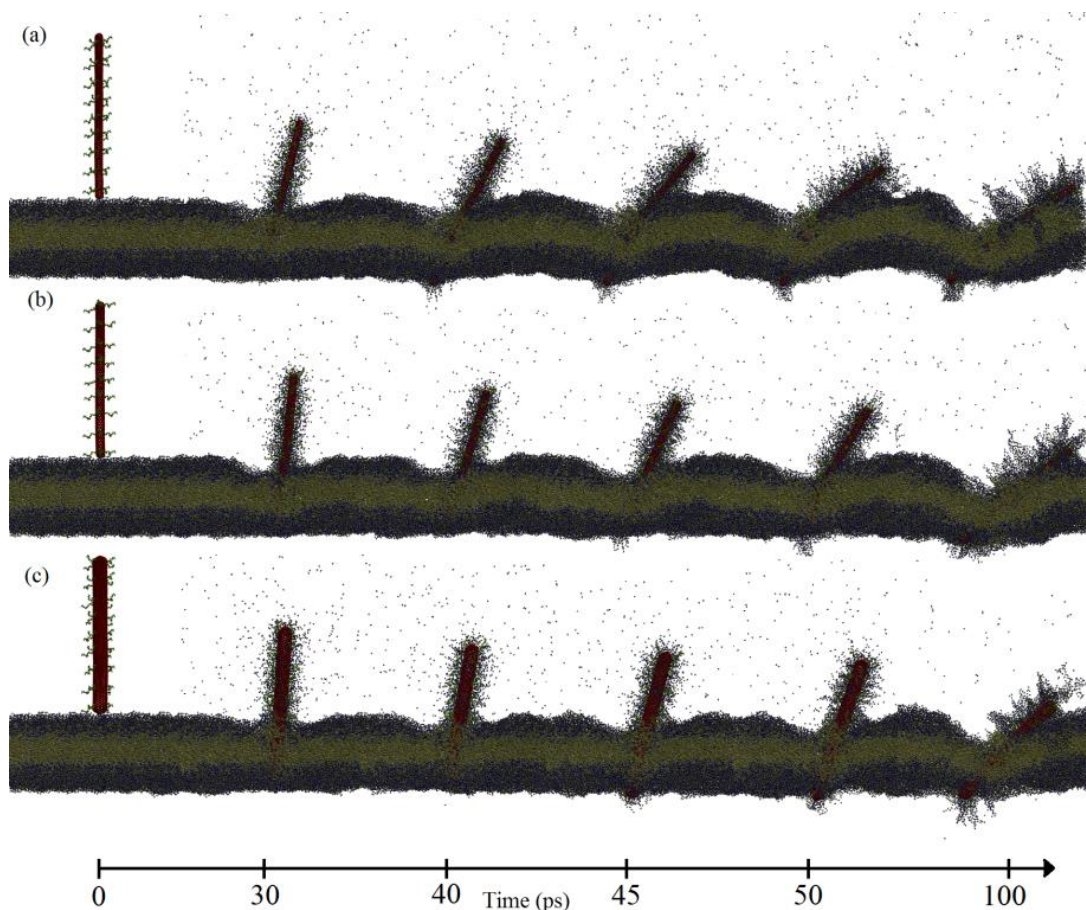


Figure 2.14. Schematic representation of f-SWCNTs penetrating into lipid membrane, a) (5, 5), b) (10, 0), c) (10, 10) chiralities.

The tendency towards more bending and stretching of the membrane by f-SWCNTs can be explained in two ways. First, the presence of PEG ligands by themselves acts as physical obstacles which prevents the SWCNT to penetrate easily and makes the probe bulkier and blunter. Second, the hydrophilic functionality of PEGs modifies the surface properties of the probe in a way that less segregation happens to the lipids so that they can maintain their surface tension and stretch considerably without rupture.

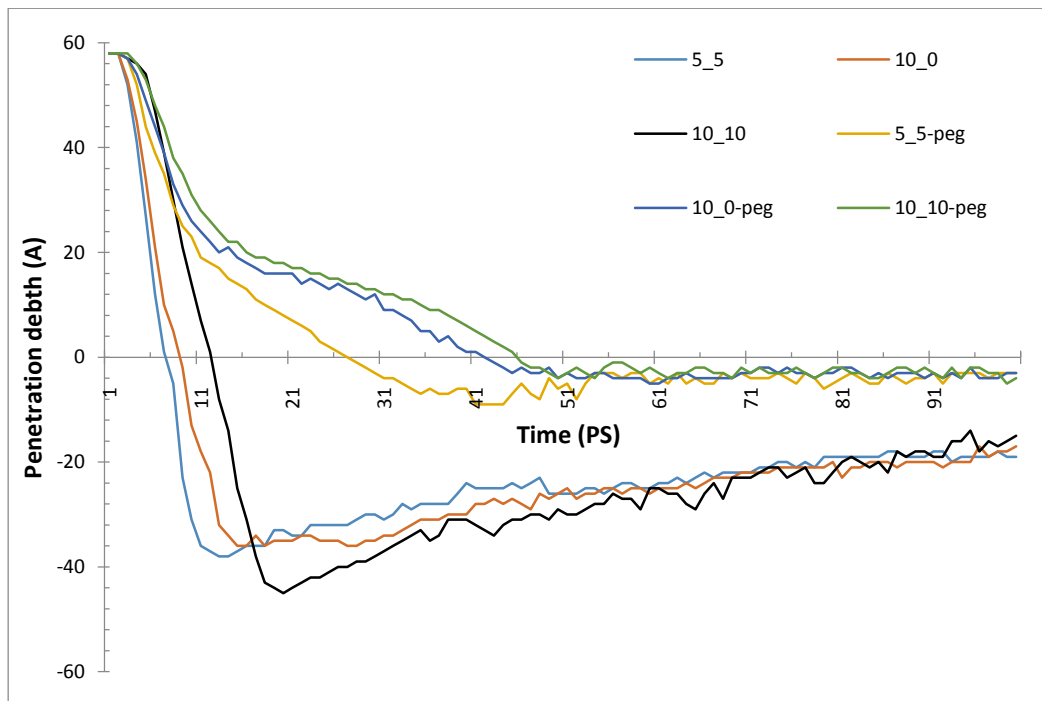


Figure 2.15. Molecular dynamic evolution of the trajectory of the Z coordinate of the bottommost carbon atom for all studied systems.

For the sake of kinematic analysis, Figure 2.15 is plotted to show the trajectory of the bottommost carbon atom versus the simulation time. It can be seen that the elapsed time for the f-SWCNTs to complete their transfection process is considerably greater than that for SWCNTs

while the chirality dependent precedence stayed the same. This observation simply means that functionalizing did not change the chirality dependent uptake of SWCNT into lipid cell membrane. On the other hand, the fast insertion of the SWCNTs follows by a bounce back while the f-SWCNTs exhibit less rebound and a much shallower penetration depth.

2.5.3.1. Adhesion Energy

As discussed earlier in the introduction part, the importance of functionalizing mostly arises from the fact that opsonins attack the pathogens simply by adhering to them. So merely calculating the adhesion energy can disclose significant information about the mechanism(s) based on which a functionalizing agent can help a therapeutic nano particles to maintain a high blood circulation life time. The adhesion energy is calculated as the difference between the potential energy of the SWCNT/membrane or f-SWCNT/membrane system and the sum of the potential energies for the membrane and the corresponding SWCNT/f-SWCNT: $\Delta E = E_{total} - (E_{CNT} + E_M)$, where E_{total} is the total potential energy of the whole system at the end of the dynamic evolution and E_{CNT} & E_M are the potential energy of SWCNT/f-SWCNT and membrane respectively. A 100 ps separate MD simulation was conducted on all SWCNTs, f-SWCNTs and the membrane under NVT ensemble to calculate the proper E_{CNT} & E_M for each case. Plotted in Figure 2.16, the adhesion energy can be compared side by side for each configuration. It can be concluded that higher chiralities ends up with less adhesion energy when functionalized with small number of PEG chains. However, the lowest chirality (5, 5) tends not to be affected too much with slight PEG assist functionalizing. The 0.79% increase for the case of (5, 5) chirality can be neglected due to the randomness of the initial velocities in the first step of dynamic run. These findings are in a

good agreement with the discussed experimental observation where PEGs helped the nano particles to circulate more and easier in the blood without being attacked by blood cells.

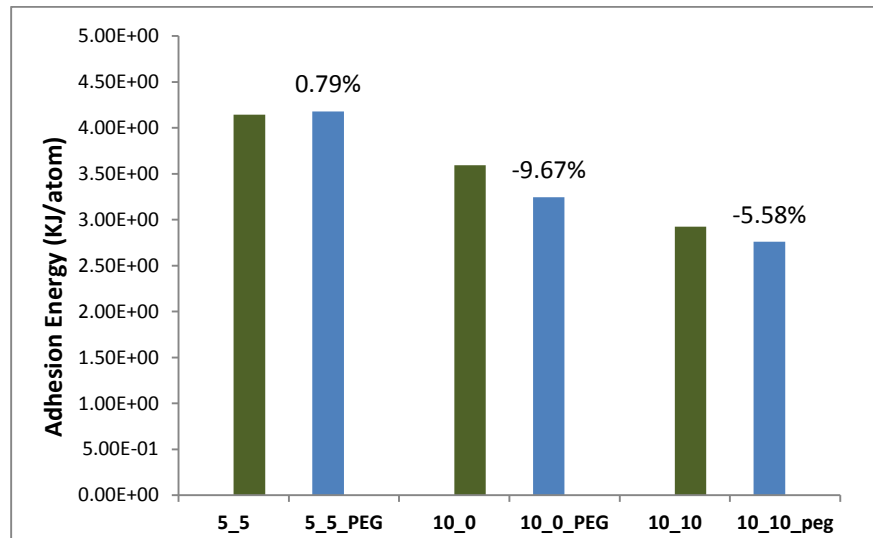


Figure 2.16. Changes in the adhesion energy after PEG functionalizing. Red bars represent the adhesion energy for different chirality SWCNTs and the adjacent blue bars are the PEG functionalized counterparts.

2.6. Conclusions

In this study molecular dynamic simulations were employed to understand the effect of chirality and length on the translocation of SWCNTs into a lipid bilayer cell membrane as well as surface functionalization. The simulations revealed that at the earliest time spans the mechanism of interaction between the SWCNT and the membrane is pure penetration. As time evolves, penetration is accompanied by endocytosis and almost halfway through 60 ps, endocytosis becomes the dominant form of interaction. Also they showed that the presence of the (PEG) molecules enhanced the penetrability of the SWCNTs in the lipid membrane. The studies also

showed that shorter nano tubes -with length shorter than the thickness of the membrane- undergo significant rotation during the endocytosis stage. By doubling the length, all of SWCNTs did penetrate through the membrane and the chirality showed its effect vividly. Lower chirality (higher aspect ratio) assisted the SWCNT to cross through the membrane faster. This was also concluded from the lesser adhesion established between the membrane and the SWCNT with lowest chirality; (10, 0). As little of the SWCNT energy was consumed to establish adhesion with the membrane it was capable of translocating through the membrane from the other side faster than the other nano tubes. The results of the (10, 5) nano tubes suggest that there is an optimal aspect ratio/chirality value at which the adhesion to the membrane attains a minimum. Furthermore, the aspect ratio of the SWCNTs plays a major role in defining the mechanism by which the SWCNTs penetrate through the lipid membrane. The higher chiral tubes inserts slower with/without surface functionalizing PEG chains which reveals marginal contribution of PEG ($n=1$) to the potential energy of the overall system. Schematic observations divulge a significant difference in the penetration mechanisms of f-SWCNTs versus SWCNTs where the PEGlayted ones tend to penetrate with less energy dependent mechanism and imposing more deflection to the membrane. It was shown that even a small percentage of water soluble PEG chains when attached covalently to the SWCNT can slow down the penetration process regardless of the chirality. This property can be utilized for incorporating the SWCNTs in a much smarter way for selective targeting of desired cells. Also, PEG chains even in a small proportion reduced the adhesion energy up to 10% which concur with the experimental findings about the circulation time of PEGlayted particles in the blood serum.

|Chapter 3

3. Nano Mechanical Characterization of the Negative Stiffness of a Ferroelectric Material using Nano Indentation[†]

Abstract: Phase changing materials such as ferroelectric materials can exhibit negative stiffness under certain thermo mechanical environments. This negative stiffness is embodied by the means of a deflection along the opposite direction of the applied load. So far negative stiffness materials are investigated with the morphology of embedded inclusions in stiff matrices then the resulting composite is studied to measure the behavior of each constituent indirectly. In this study a modified nonisothermal nano indentation method is developed for to measure the negative stiffness of triglycine sulfate (TGS) single crystal directly. This *in situ* method is intended to first demonstrate the feasibility of detecting the negative stiffness via nano indentation and nano creep

[†]The content of this chapter is an extended version of :

A. Alipour Skandani, R. Ctvrtlik, M. Al-Haik, Appl. Phys. Lett. 105, 082906 (2014).

Reprinted with permission from APL. Copyright 2014, AIP Publication.

of a ferroelectric material at its Curie point and then to quantify the negative stiffness without the need for embedding the crustal within a stiff matrix.

3.1. Introduction

Most mechanical and structural systems are subjected to loading and operating conditions that may result in vibrational motions. A strategy for vibration mitigation involves incorporating a material with controllable behavior into the system and limiting the vibration levels in its response. For instance, by increasing the product of the storage modulus (given by the stiffness, E) and the damping capacity (given by the loss tangent; $\tan\delta$) of the material, the vibration can be reduced. The product of these two quantities is the loss modulus, which can be treated as a figure of merit for vibration attenuation ability ¹⁰⁶. As for stiffness improvement, the bounding theorems state that no composite can be stiffer than the Voigt bound ¹⁰⁷ and no macroscopically isotropic composite can be stiffer than the Hashin– Shtrikman ¹⁰⁸ upper bond. In proving these theorems, positive definiteness of the strain energy density was assumed. Moreover, based on the Voigt upper bound, it would seem that no composite could be stiffer than the stiffest constituent. That is true if each phase has a positive stiffness. This limitation can be overcome if one component with negative stiffness is embedded in the composite.

Ordinarily, the deformation is along the same direction as the applied force and the stiffness is then labeled as positive. Negative stiffness implies a reversal of this usual directional relationship between load and deformation. Such irregularity was first observed in constrained bi-

stable structures such as buckled beams^{21, 22}. The importance of such phenomenon can be expressed in terms of elevated vibrational damping²³, composites with infinite stiffness^{24, 25} and acoustical absorbers²⁶. Further applications are still evolving ranging from meta-materials to seismic protection of structures²⁷ and strings with negative stiffness and hyperfine structure²⁸.

While the evaluation of bi-stable structures as negative stiffness elements has been studied in several cases^{21, 27} the investigation for materials with negative stiffness remains limited to the proof of the concept. Lakes *et al.*^{24, 29} showed that materials undergoing certain structural changes, mostly phase transformations, when embedded within a constraining matrix can display negative stiffness. They also showed that the concept of the negative stiffness is fundamentally different from the negative Poisson's ratio materials. Lakes and Drugan³¹ showed that if one phase has the appropriate negative stiffness, the overall mechanical stiffness of the composite can be made dramatically large when the stimulating factors (temperature in the case of a phase change) reaches the threshold. They also showed that in the presence of a small nonlinearity, extremely high stiffness could be achieved without singularity of the elastic fields. Lake *et al.*²⁴ reported an infinitely stiff composite of VO₂ 1% –Sn around the phase transition temperature of VO₂ (~66 °C). Furthermore, based on their observation the damping coefficient ($\tan \delta$) showed a peak at the same temperature range with a value much greater than best naturally damping materials such as rubber. They concluded that this extraordinary material response, in the temperature range where inclusions show abnormalities, arises from their elastic constants switching from regular behavior (positive) to an irregular unstable mood (negative). However, they could only claim the stiffness of the inclusions to be negative for the limited morphology of spherical inclusions polydispersed in an isotropic composites through the Hashin-Strickman shear modulus formula²⁴:

$$G_L = G_2 + \frac{V_1}{\frac{1}{G_1 - G_2} + \frac{6(K_2 + 2G_2)V_2}{5(3K_2 + 4G_2)G_2}} \quad 3.1$$

Where K_1 and K_2 , G_1 and G_2 , and V_1 and V_2 are the bulk moduli, shear moduli and volume fractions of the inclusion and the matrix, respectively. The combined shear modulus G_L attains its maximum value when the inclusions have a value of about -1.1 (negative) times that for the matrix. This means that the negative stiffness materials are unstable and can be stabilized by embedding them in a rigid matrix.

Negative stiffness can be obtained through structural phase transformations associated with temperature induced shape change. Vanadium dioxide (VO_2) is a strongly correlated electron oxide, which exhibits an abrupt first-order metal-insulator transition (MIT) at a Curie temperature of 68 °C with a change of few orders of magnitude of electrical conductivity. The drop in conductivity is accompanied by a ferroelastic tetragonal-to-monoclinic lattice structure transformation that evidences the significant lattice contribution in the formation of the electronic band gap. Such change in crystallographic parameters yields two distinct phases pre and posts the Curie temperature with different mechanical and physical properties such as stiffness, thermal expansion coefficient and optical properties. This multifunctionality makes VO_2 an excellent candidate for numerous applications in optical, electronic, and optoelectronic devices.

In this study triglycine sulfate (TGS) ($\text{NH}_2\text{CH}_2\text{COOH}$)₃· H_2SO_4 was chosen over VO_2 because of its rationally higher stability in the presence of the oxygen and none toxicity whereas VO_2 is toxic and tends to convert to higher order oxides under atmospheric environment. Furthermore, TGS possesses a reported Curie temperature around 47°C which is one of the lowest phase transforming temperatures among ferroelectric materials ¹⁰⁹. The dielectrics, optical and

thermal properties of TGS at different thermal environments, particularly near its Curie point, are well documented¹¹⁰⁻¹¹³.

In this study, for the first time, we demonstrate the feasibility of utilizing instrumented nano indentation techniques to directly capture the negative stiffness of a ferroelectric material quantitatively rather than the qualitative indirect approximation with respect to a stiff matrix.

Continuous depth sensing nano indentation tests provide load–displacement plots, which act as mechanical fingerprint. During a typical nano indentation test a diamond tip of known geometry is pressed into the sample surface, while the indentation load and depth are continuously recorded. Hardness and elastic modulus are measured in most cases, but other phenomena like pressure-induced phase transformations ¹⁷, incipient plasticity ¹⁸ or time dependent effects ¹⁹ can also be studied by analyzing the indentation loading-unloading hysteresis. Furthermore, it is possible to perform nano indentation tests at elevated temperatures and study the temperature-dependent behavior of the materials ²⁰.

3.2. Materials and Experiments

Single crystal TGS was grown from an aqueous solution of sulfuric acid, containing three-fold excess of glycine ¹¹⁴. After complete evaporation of the water phase, part of the resultant crystals were crushed into powder and X-ray diffraction analysis (XRD) was performed to verify the crystallinity and chemical composition of the produced powder.

Nano indentation and nano creep tests were carried out using a NanoTest® 600 system (Micro Materials Ltd., Wrexham, UK) in load control mode. A schematic diagram of the

instrument is shown in Figure 3.1.a. A Berkovich diamond indenter tip is attached to a pendulum that rotates freely around a virtually frictionless pivot. The indenter is loaded against the sample by passing a current through the coil, which is then drawn to the permanent magnet. Displacement of the indenter into the sample is measured by the variation in voltage between the capacitance plates. The NanoTest 600 is equipped with a hot stage indentation module, which allows reliable measurements at temperatures as high as 750 °C¹¹⁵⁻¹¹⁷. The heating element only has localized effects so that minimal heat flow and thermal drift occur during indentation at high temperatures. As shown in Figure 3.1.b, an aluminum thin shield is placed in front of the pendulum to prevent any thermal interference with the electronics and depth sensing equipment. The indenter and its heater are passed through the thermal shield. The sample is mounted on a ceramic thermal insulator and the heater is embedded inside the thermal insulator block.

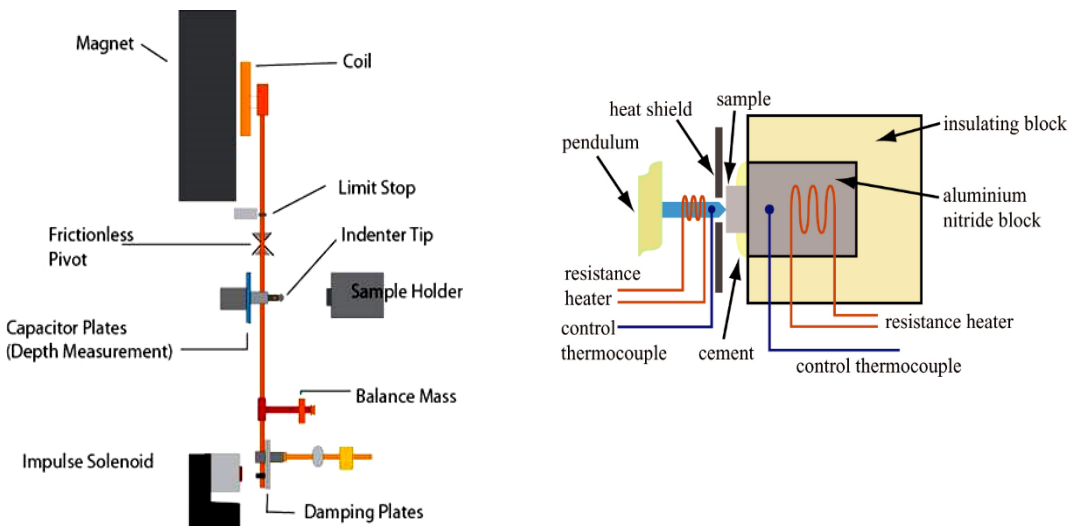


Figure 3.1. Schematics of the (a) NanoTest system and (b) hot stage feature.

TGS crystal with dimensions of 5mm × 5 mm and a thickness of 2 mm was mounted on the hot stage, using a conductive silver adhesive, aligning the (001) crystallographic direction of the crystal with the loading direction. The temperature of the specimen was monitored and controlled with two thermocouples mounted beneath and on the surface of the sample. The sample was heated to 60 °C at a rate of 2.3 °C/min. Upon reaching this temperature the sample was loaded using a diamond pyramidal Berkovich nano indenter tip at a loading rate of 5 mN/s to a maximum load of 50 mN. The sample was left to creep isothermally at this maximum load for 60 s. After the dwell period, the sample was unloaded at a rate of 0.064 mN/s while transiently cooled from 60 °C to 37 °C. This temperature range was chosen to include the anticipated phase transition temperature of approximately 47 °C. The thermo mechanical history of the sample is illustrated in Figure 3.2.a.

During the isothermal loading cycle, the recorded nano indentation depth comprises of elasto-plastic deformation. While throughout the unloading/cooling cycle the sample is exposed to thermal expansion/shrinkage, deformation due to phase transition and the elastic/plastic deformation due to loading. In order to isolate the deformation due to phase transition from the other types a separate nano indentation creep test was conducted.

In this nano creep test, using a spherical diamond indenter tip (50 µm radius) the sample was loaded to a maximum load of 0.5 mN within 10s. The sample was left to creep for 60s at this maximum load under 60 °C. Then, while holding the load constant the sample was cooled down to 37 °C within 780s, Figure 3.2 (b). The large spherical tip minimizes amount of plastic deformation and hence the creep depth reflects primarily the thermal shrinkage and expansion above and below phase transition temperatures, respectively. Thus, by subtracting the depths

obtained from the constant load creep/cooling using the spherical indenter from the unloading curve measured at the high load using Berkovich indenter we can obtain the depth data relevant to the mechanical loading and phase transition of the sample; which is needed for the stiffness analysis.

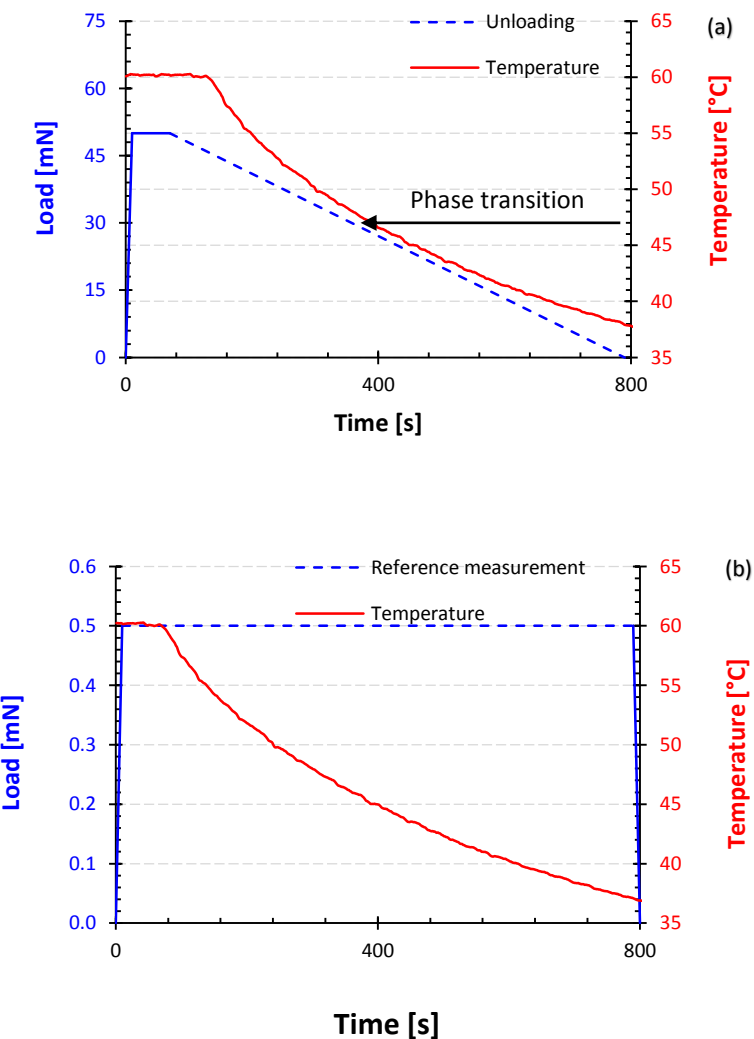


Figure 3.2. (a) Nano indentation thermomechanical history of the sample using a Berkovich indenter and **(b)** The thermomechanical record of a nano creep test performed using spherical indenter at low load to account for deformation due to sample thermal expansion.

Finally, to investigate the creep deformation while the sample undergoing phase transition a nano creep test was conducted by loading the sample to maximum load of 50 mN in 10s using a Berkovich indenter then holding the load constant and the temperatures at 60 °C for 60 s, finally allowing the sample to cool down to 37 °C while unloading for 780 s as shown in Figure 3.3 .

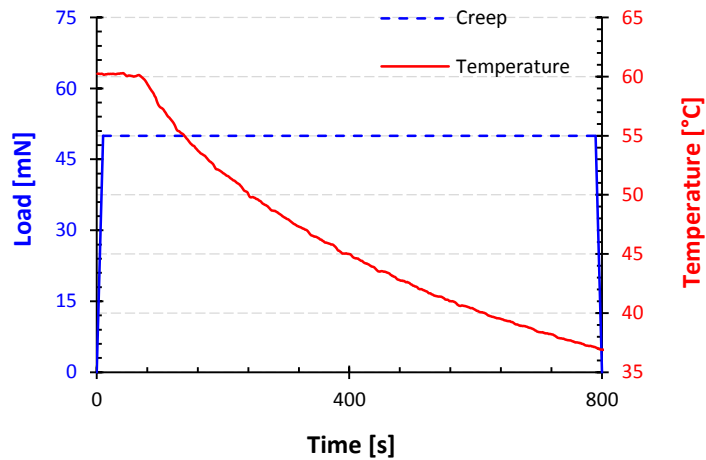


Figure 3.3. The load-temperature evolution during the nano creep test using a Berkovich nano indenter.

3.3. Results and Discussion

Figure 2.4 depicts the XRD pattern of the synthesized TGS powder where, the characteristic peaks indicate high degree of crystallinity of TGS. Furthermore, the diffraction pattern indicates that the room temperature crystal of TGS takes the rhombohedra shape.

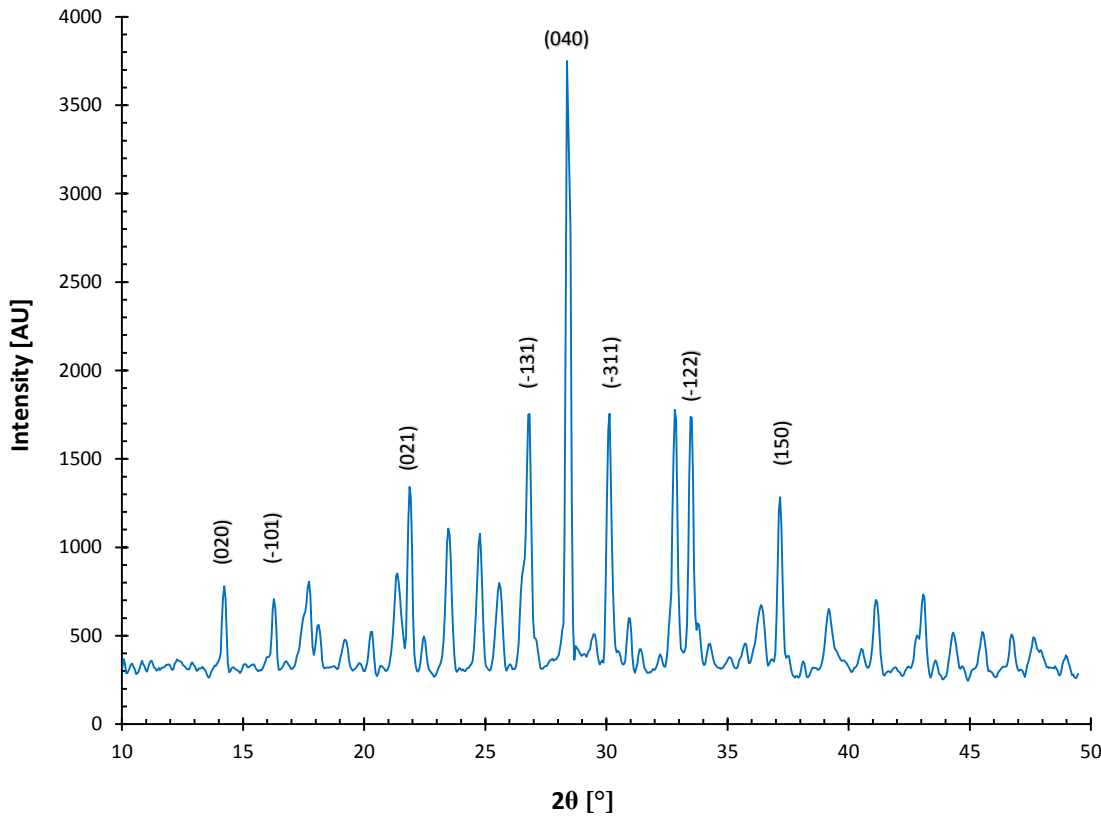


Figure 3.4. Measured XRD pattern for TGS.

The measured indentation hysteresis is shown in Figure 3.5. As can be seen the shape of the unloading/cooling portion of the indentation cycle is very different from the standard isothermal curve. The unusual shape of unloading curve is a synergistic result of several effects and processes. The directly measured curve (labeled as uncorrected in Figure 3.5) comprises not only the elasto-plastic indentation response of the material but it also includes deformations due to nonlinear thermal drift, change in the sign of coefficient of thermal expansion and phase transition from the rhombohedral system with $P2_1/m$ symmetry to the ferroelectric phase with the non-centrosymmetric monoclinic point group $P2_1$ ¹¹⁸. Therefore, the standard Oliver-Pharr method

¹¹⁹ to evaluate the stiffness of TGS as it undergoes these phenomena is not readily applicable and appropriate corrections should be imposed on the unloading curve.

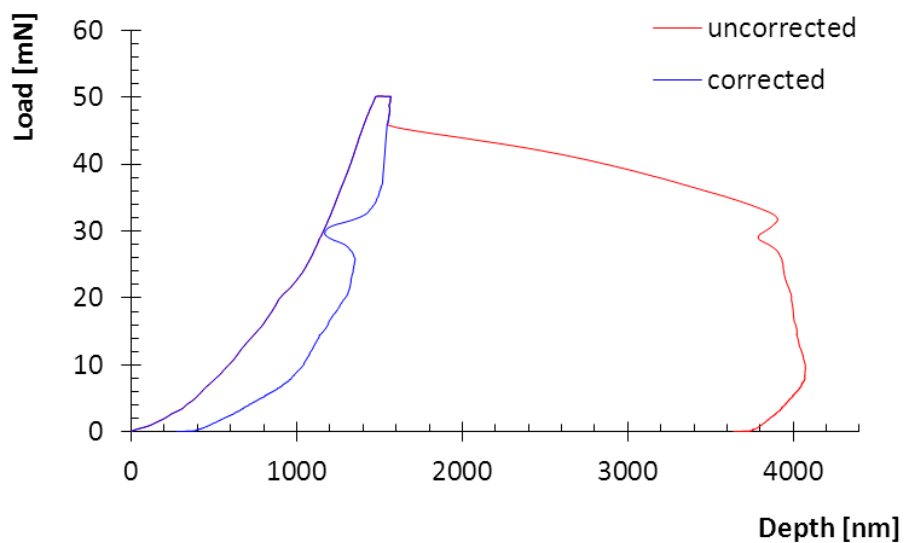


Figure 3.5. Indentation hysteresis pre and post unloading depth corrections. The unloading cycle was performed in the temperature range of 60-37 °C¹²⁰.

Standard indentation tests are fundamentally performed under isothermal conditions and any thermal drift correction is based on the assumption of its linear and monotonous character. This does not hold for the case when the temperature changes nonlinearly in a wide range. Another deviation from standard indentation analysis arises from the fact that the coefficient of thermal expansion of TGS crystal alters its sign upon passing through the transition temperature ¹¹². In order to compensate for the thermal drift and the change in the coefficient of thermal expansion the reference data were acquired at the same experimental conditions under constant and very low load of 0.5 mN (obtained via spherical indenter) during the 780 s dwell indentation creep

experiment illustrated in Figure 3.2. The change in depth due to TGS crystal volume changes during the temperature sweep is much larger than the change in depth due to the time dependent low load creep effects. Therefore, the considerably low load for the correction dataset asserts that it contains all depth penetration data for the thermal drift rather than the depth as the material response to loading. With the considerably small applied load and slow cooling rate, one can take the two constituents of the depth penetration to be linearly independent and hence subtract one part from the total recorded depth to get the other part. Subtracting the reference data from the as-measured unloading part of the indentation curve allows obtaining the corrected unloading curve. The corrected unloading curve comprises only the elastic deformation and deformation due to phase transition and can be further analyzed using the standard methods^{119, 121}.

As the TGS phase transition is temperature-dependent, the indentation depth is plotted together with the corresponding temperature of the TGS crystal during the experiment with respect to time in Figure 3.6. It is clear that the corrected unloading curve possesses the usual shape at the beginning of unloading/cooling portion until the crystal reaches temperature of ~ 50 °C. At this point the sudden change occurs and the unloading curve kinks out as a result of the TGS phase transition from rhombohedral to non-centrosymmetric monoclinic phase. Using the conventional analysis of nano indentation curves based on approximation of the unloading curve by power law fit (Oliver and Pharr¹¹⁹) or linear fit (Doerner and Nix¹²¹) the contact stiffness can be estimated using the slope of the upper portion of the fitted unloading curve. Providing that the indentation contact area A is known the reduced elastic modulus E^* can be deduced from its relationship with contact stiffness S .

$$S = 2\beta E^* \sqrt{\frac{A}{\pi}}$$

3.2

Where β is a dimensionless parameter that equals 1.034 for Berkovich indenter and 1.0 for spherical indenter tip. The indentation hardness H is defined as the ratio of the peak force P_{\max} and projected area A

$$H = \frac{P_{\max}}{A}$$

3.3

In order to extract the values of the mechanical properties from the corrected indentation curve, the linear approximation of the upper part of the unloading curve was employed as can be seen from Figure 3.7. The linear fit in the range 99-72% of maximum depth (indentation load of 50-36 mN) gives a contact stiffness of 0.223 mN/nm that corresponds to a reduced modulus of 27.2 GPa and indentation hardness of 1.0 GPa. The interaction of the diamond indenter with the TGS crystal undergoing the temperature induced phase transition results in a change in slope of the unloading curve from positive to negative. Using the approach utilized for analyzing the upper portion of the unloading curve, the slope of the negative portion of the unloading curve corresponds to 29-27 mN, which yields a contact stiffness of -0.012 mN/nm. This change of slope suggests that the magnitude of the negative stiffness is approximately 5% of the regular (i.e. positive) contact stiffness.

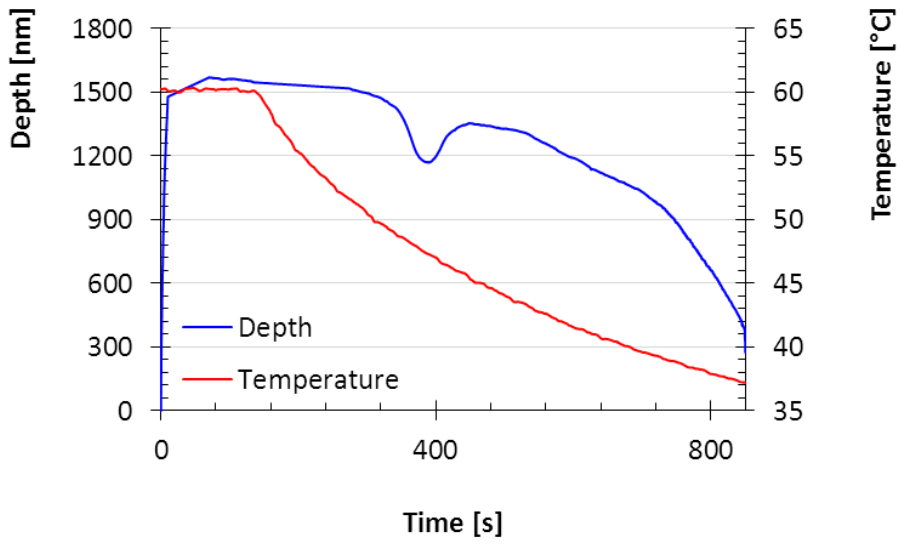


Figure 3.6. The time/temperature evolution of the corrected indenter penetration depth during the indentation experiment performed using a Berkovich indenter in the range of 37-60 °C.

Analysis of the corrected indentation curve using the power law fit of its upper portion (99-73%) results in contact stiffness of 0.237 mN/nm that corresponds to reduced modulus and hardness values of 27.2 GPa and 0.99 GPa, respectively. Comparison of results of both fits suggests a very good feasibility of the linear approximation and justifies its application in this particular case. In both cases the actual diamond area function was used.

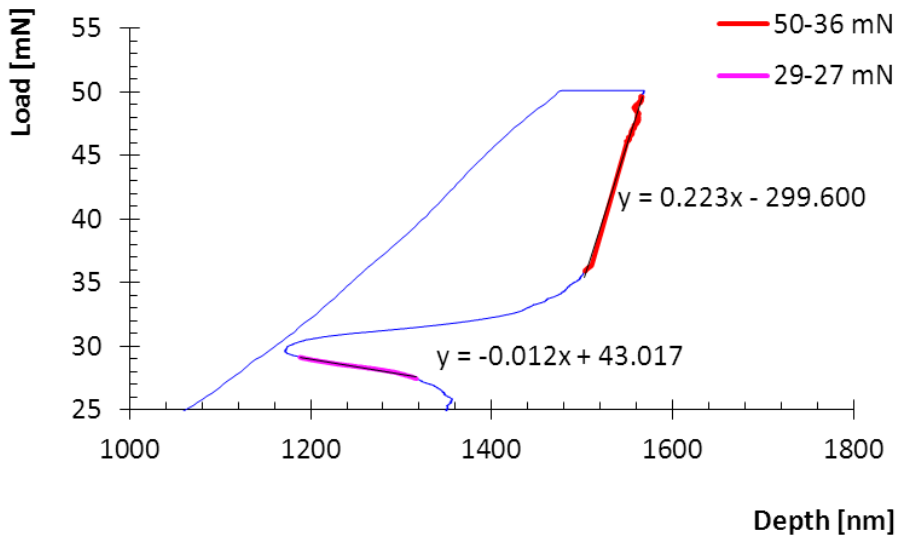


Figure 3.7. Upper part of the corrected indentation curve with the linear fit of its positive and negative sloped sections¹²⁰.

Besides the regular nano indentation test, nano creep tests can also detect the presence of the phase transition. The nano creep load-temperature evolution were introduced in Figure 3.3. Figure 3.3. The load-temperature evolution during the nano creep test using a Berkovich nano indenter. The measured creep depths were corrected using an identical approach to that utilized for correcting the nano indentation unloading curve. The evolution of the corrected creep curve together with TGS crystal surface temperature during the dwell period is presented in Figure 3.8. The creep depth increases with time as expected until the temperature reaches the phase transition temperature (~47°C).

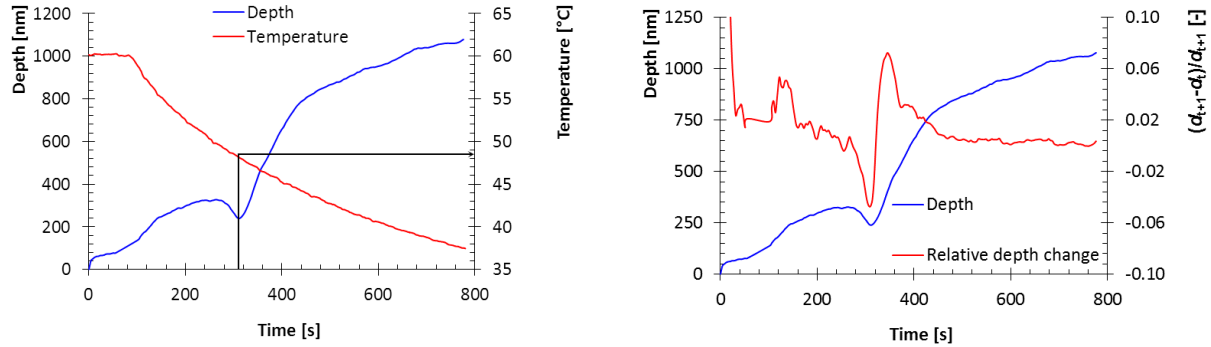


Figure 3.8. Time evolution of the corrected creep curve for the TGS crystal with (a) corresponding temperature and (b) depth change rate during 780 s duration creep test measured in the temperature range of 60-37 °C.

By definition the constant stress during creep relates to the varying (normally increasing) strain with creep compliance

$$\sigma = C\varepsilon.$$

On the other hand the instantaneous strain under indentation loading at time t is proportional to $(d_{(t+1)} - d_{(t)})/d_{(t+1)}$, where d denotes the penetration depth and it is taken to be positive in the load direction. It can be inferred from Figure 8(b) that when the material undergoes phase transformation $d_{(t+1)} < d_{(t)}$ and hence the sign of ε becomes negative. As the stress is always constant (positive) throughout the test, the sign of the creep compliance coefficient should also be negative in order for σ to remain positive.

3.4. Conclusions

The negative stiffness for ferroelectric materials undergoing phase transformation are typically explored while these materials are embedded in a stiff constraining media. However, this morphology deems the negative stiffness material inaccessible and thus no direct measurement of its stiffness is possible. . In this study the stiffness and creep behavior of a low Curie temperature ferroelectric material were measured in-situ utilizing a novel non-isothermal nano indentation technique at the onset of its phase transformation. Triglycine sulfate (TGS) single crystals were grown by evaporating the water phase from the mixture of its constituents (i.e. sulfuric acid and glycine in stochastic ratio). A single crystal of TGS was mounted on a hot stage along the (001) direction aligned with the indentation loading direction. Different nano indenter tips geometries were utilized to mimic the effect of constraining media (in the direction of the applied load) while the tests were carried out in a temperature range of 60 °C to 37 °C. Assuming a large ratio of the overall crystal volume to the sample/indenter contact area and slow cooling rates the thermally induced displacement of the nano indenter was eliminated by imposing proper corrections. It was shown that the TGS crystal, around it transformation temperature (47°C), exhibits both a negative stiffness (in the order of -1.5 GPa) and a negative creep compliance. This study provides a nondestructive methodology to examine the presence of negative stiffness and to quantify the change of the stiffness around the phase transition temperatures.

Chapter 4

4. Vibrational Damping and Viscoelastic Characterization of Hybrid Carbon Fiber/ZnO Nano Rods Polymer Composite[‡]

Abstract: *The insufficient viscoelastic resistance of fiber reinforced plastics (FRPs) can be retrofitted by the addition of more rigid nano fillers to the polymer based matrix. Also increasing the interfacial frictional energy dissipations utilizing 1D nano structures and consequently improving structural properties of composites is well known. In this study, carbon fibers plies were grafted with zinc oxide (ZnO) nano rods and the hybridized reinforcement was utilized in laminated composites. Flexural creep tests were carried out using dynamic mechanical analysis (DMA) and for accelerated testing the time/temperature superposition principle (TTSP)*

[‡] The following chapter is an extended version of the following articles:

- (a) A. Alipour Skandani, A Yari Boroujeni, R Kalhor, SW Case, M Al-Haik, Polymer Composites, Article in press.
Reprinted with permission from Polymer Composites. Copyright 2014, Wiley.
- (b) A. Alipour Skandani, SW Case, DJ Leo, M Al-Haik, Applied Physics Letters 101 (7), 073111(2012).
Reprinted with permission from APL. Copyright 2013, AIP Publications.

was applied. To verify the applicability of TTPS, prolonged stress relaxation tests were also carried out in flexural mode. Data from the DMA flexural creep tests revealed that the whiskerization of carbon fibers with ZnO nano rods reduces the creep compliance by 23% at elevated temperatures and prolonged durations. Also, the relaxation data confirmed the applicability of TTPS to these hybrid composites. The stress relaxation modulus improved by 65% in comparison to composites based on neat carbon fibers. The resultant composites were then tested for vibrational attenuations using dynamic mechanical analysis (DMA). Results revealed that the growth of ZnO nano rods on top of carbon fiber increases the damping performance by 50% while causing a slight decrease (~7%) on the storage modulus. The enhanced damping of the hybrid composites can be related to the frictional mechanisms between the ZnO nano rod/epoxy and nano rod/nano rod interfaces combined with piezoelectric effect of ZnO.

4.1. Introduction

Due to various cost and processing impediments, several investigations departed from introducing nano materials directly into polymeric hosts¹²². Alternatively, the concept of hybrid fibers has emerged. These fibers comprise standard structural fibers (e.g. carbon, fiberglass, aramid or SiC) with surface grown nano fibers or nano tubes (e.g. carbon nano tubes^{7, 123} or ZnO nano rods). The motivation of growing 1D metal oxide nano structures in general and ZnO nano rods in particular over structural and conductive fibers commences from their contribution to a wide range of applications such as smart materials for energy scavenging^{124, 125}, improved mechanical behavior through better matrix-to-fiber adhesion , gas sensors¹²⁶, field emission¹²⁷, photo-electrochemical cells¹²⁸, surface polarity shielding¹²⁹ and improved damage resistance¹³⁰.

Fiber reinforced plastics (FRPs) are the constituents of wide range of structures from civil to naval edifices. Certain applications entail exposing these materials to higher temperatures for during their life cycles. The exposure to high temperatures and/or prolonged loading of these composites makes them prone to viscoelastic deformations that could hamper their durability.

Creep and stress relaxation tests are the most utilized experiments to manifest the time/temperature dependent changes in different materials. These tests dictate their importance even further when the strength and the durability of structures made of FRPs vary dramatically with their viscoelastic behavior. The time-decaying stresses should be considered in the design of polymer matrix composites where stress relaxation takes place under constant displacement condition and makes the whole structure prone to failure in an unexpected mode. From the several mechanisms that trigger stress relaxation, the intrinsic viscoelasticity of the polymeric matrix and the straightening of the reinforcing fibers from their possible initial weaves are of significant importance. Also, the slippage mechanisms between the fibers and the matrix can contribute as another source of the viscoelastic behavior of FRPs. While there have been few attempts on investigating the effect of ZnO nano particles addition on the viscoelasticity of polymers¹³¹⁻¹³³, the effect of surface grown ZnO nano rods on the time dependent mechanical behavior of hybrid composites haven not been demonstrated yet.

The time-temperature dependent behavior of conventional FRPs has been depicted utilizing different constitutive models that were originally designed for polymers^{32, 134-137}. Creep tests require prolonged testing time as the rate of change can be very slow (in some cases several years). Hence, different accelerated methods have been developed to predict the long-term creep behavior of polymeric materials using data from tests at elevated temperatures with considerably

shorter durations. The time–temperature superposition (TTSP), Findley’s model ¹³⁸, Schapery’s model ¹³⁹ and polymer modified thermal activation energy theory ¹⁴⁰ are some of the widely utilized accelerated creep testing schemes. Viscoelasticity of FRPs has been studied utilizing standard short-time creep tests at different temperatures to predict their long-term creep behavior ^{135, 141}. Like many other mechanical properties, the creep compliance and the stress relaxation modulus (as two governing material parameters for viscoelasticity) are much weaker along the transverse direction to the fiber orientation ¹⁴². This heightens the importance of studying the flexural creep properties in orthotropic or transversely isotropic FRPs where the axial direction is designated as the fiber direction, which exhibits the least deformation, imposed by time or temperature variations. Flexural creep tests for thin-layered FRPs can be carried out with a 3-points bending fixture in dynamic mechanical analysis (DMA) instruments. Application of DMA as one of most convenient load/displacement controlled testing tools are practiced extensively both for static and dynamic analysis of polymeric materials. Studying the viscoelastic behavior of polymeric composites in general and creep and stress relaxation in particular utilizing DMA have been reported in several investigations ^{141, 143}.

In this investigation we studied the creep and relaxation of ZnO nano rod/carbon fiber hybrid nano composites - prepared with a low temperature hydrothermal method- utilizing DMA.

A simple, yet an effective, definition for creep compliance is given by

$$J(t) = J^0 e^{\frac{t}{\tau} \beta} \quad 4.1$$

Where J^0 , τ , β are the initial compliance, retardation time and shape factor, respectively. In order to exchange the data between the temperature and time domains, the compliance should be a function of temperature as well:

$$J = J(T, t) \quad 4.2$$

The superposition principle between the time and temperature requires the compliance at different temperatures to be related to the reference temperature T_0 via a factor $a_T(T)$ through reduced time; $\rho = t/a_T(T)$ making the compliance a function of both the reference temperature and reduced time.

$$J = J(T_0, \rho) \quad 4.3$$

Upon expressing the reduced time (ρ) in the logarithmic scale, $a_T(T)$ becomes a shift factor spanning over a wider range of time through a linear combination of $\log \rho$ and $\log t$ ¹⁴¹:

$$\log \rho = \log t - \log a_T(T) \quad 4.4$$

The creep compliance data can be normalized with respect to the applied stress such that it can be expanded to all stress levels within the linear viscoelastic range^{141, 143}. Typically, the obtained master curve from the TTSP analysis can be verified against long-term creep experiments⁴². In the current study, to verify the validity of the obtained creep master curves, the inverse proportionality of the creep compliance with the relaxation modulus is utilized in this study. Fiber reinforced polymer (FRP) composites can dissipate some energy on their own due to the fiber and matrix elastic/viscoelastic behaviors. However, traditional FRPs suffer from insufficient vibrations attenuation¹⁴⁴⁻¹⁴⁶. Consequently, an enormous interest is exalted to boost the vibration damping properties of FRPs while retaining their lightweight and in-plane structural properties. Energy

dissipation mechanisms can be elevated by embedding a viscoelastic layer between the laminates at the cost of lowering the strength and stiffness¹⁴⁷, fibers' surface treatment¹⁰⁶, addition of nano fillers^{147, 148} and matrix modification via viscoelastic particles¹⁴⁹.

The slippage and frictional mechanisms at the filler/matrix interfaces are the main culprits for improving the FRPs' damping and for the case of nano scale high-aspect ratio fillers (e.g. carbon nano tubes) these mechanisms are even more pronounced¹⁵⁰⁻¹⁵³. How efficient these nano fillers are in improving the FRP damping is a function of their volume fraction, morphology and distribution within the matrix. Carbon nano tubes for instance showed maximum damping improvement when their volume fraction exceeded the mechanical percolation threshold. However, reported improvement of damping utilizing CNTs showed considerable discrepancies from zero to 700% due to unresolved agglomeration and poor dispersion of the nano tubes^{154, 155}. The high surface areas together with the van der Wall forces between the tubes compel them to entangle and form micron-sized agglomerates. Various mechanical techniques such as sonicating, calendering^{156, 157} and prolonged shear mixings were utilized to obtain reasonable dispersion of CNTs within polymer matrices.

Interfacial reinforcement through whiskerization by growing a secondary reinforcing material directly on the fiber surface is proven to have several advantages over regular surface modification methods. Selective growth of nano tubes on designated surfaces yielded better damping where up to 1400% improvement in the damping figure of merit was reported¹⁵⁸.

4.2. Experimental Methods

4.2.1. Samples Preparation

ZnO nano rods were grown on the surface of commercial PAN-based carbon fibers using a low temperature hydrothermal technique in an aqueous solution of Zn⁺² cations. To ensure the removal of polymeric sizing coating, the as received carbon fibers were initially heat treated at 550°C under inert atmosphere for 30 mins. As the ZnO nano rods tend to grow better on a substrate of identical material or another material with similar lattice parameters, a 75 nm thick amorphous ZnO film was predeposited using a magnetron sputtering system (ATC Orion high vacuum sputtering system, AJA International Inc.) on both sides of the un-sized carbon fabrics. Zinc cations in the aqueous growth solution were generated from mixing equimolar zinc acetate dihydrate ($\text{Zn}(\text{O}_2\text{CCH}_3)_{22}\text{H}_2\text{O}$) and HMTA solutions in deionized (DI) water (40 mM each). While water provides continuous supply of O⁻² anions, the role of HTMA remains undetermined¹³¹. After preparing the substrate carbon fiber cloth, several 13cm×13cm specimen were soaked in the growth solution at 80°C for 6 hrs. Three layers composites were fabricated using the dried carbon fibers with a polymeric matrix comprising two parts epoxy resin/ hardener AeropoxyTM manufactured by PTM&W Inc. The three layers layup was placed in a vacuum bag and then inside the bottom half of a composite fabrication mold connected to a vacuum line while the top half has an airway allowing the flow of compressed air up to 70 psi. The upper and lower parts of the mold were separated by means of a flexible gasket. The whole setup was placed in a hydraulic press operated at 25 tons and heated up to 65 °C for four hours. Both vacuum and hydraulic pressing were applied simultaneously to keep the carbon fibers intact under high pressure and to degas the

epoxy while curing. Resultant composites were post cured at 90 °C for an additional 2 hours to ensure complete curing of the epoxy matrix. A separate set of composites sample was fabricated using fibers with ZnO sputtered layer and identical hydrothermal exposure (i.e. DI bath for 6 hours at 80 °C), to probe the effects of both the sputtered ZnO amorphous layer and the ZnO growth environment on the carbon fibers.

4.2.2. Sample Characterization

To examine the crystallinity of the grown ZnO nano rods, chopped fibers of all three configurations were studied utilizing an X-ray diffraction (Philips Xpert Pro with Cu-K α lamp and Ni filter). To study the morphology and adhesion of the grown ZnO nano rods to the carbon fibers, electron scanning microscopy (LEO (Zeiss) 1550 field emission SEM) was employed. Rectangular coupons of 12.0 mm × 26.0 mm (0.7mm thick) were cut and tested utilizing a DMA Q800 machine (TA Instruments, Inc.). A three-point bending fixture was installed on the DMA machine and flexural creep tests were carried out over a 20.0 mm span length. First, the linear viscoelastic range of the material response was determined using a method described in ^{159, 160}, this helped to facilitate the stress normalization described earlier and kept the test away from viscoplasticity regime. Based on the linear range of the viscoelastic response a constant stress of 20 MPa was applied to all the FRP samples for the creep test. Using the flexure test data, the corresponding strains to this stress level (for each sample) were utilized for the relaxation tests. The flexural creep tests duration were set for 30 min under temperatures ranging from 35 °C- 65°C with 5 °C increment. After each temperature interval, the samples were recovered for 15 min before starting the creep test at the next temperature regime. The maximum creep temperature was

chosen to be 65 °C; far from the epoxies glass transition (~80 °C) to avoid unexpected rheological behavior. To verify the applicability of TTSP for the hybrid composites, using the DMA machine relatively long term (720 min) relaxation tests were conducted under the flexural loading mode while maintaining an initial strain that corresponds to 20 MPa stress at 35 °C. For the frequency sweep tests rectangular coupons of 12×60×0.4 mm were cut and tested with DMA following the ASTM D4056-06 standard. Tests were performed following ASTM D5418-07 under a frequency range of 1-25 Hz, 0.1% strain and room temperature with dual cantilever clamps.

4.3. Results and Discussion

Figure 4.1 depicts the X-ray diffraction pattern for all three fibers configurations. It can be seen that neat and ZnO-sputtered samples share identical characteristic peaks which represents the onion like structure of the carbon in carbon fibers. Also it can be interpreted that the sputtered layer of ZnO does not exhibit any crystallinity and thus is amorphous. The configuration comprising hydrothermally grown ZnO nano rods, shows all the characteristic peaks for ZnO.

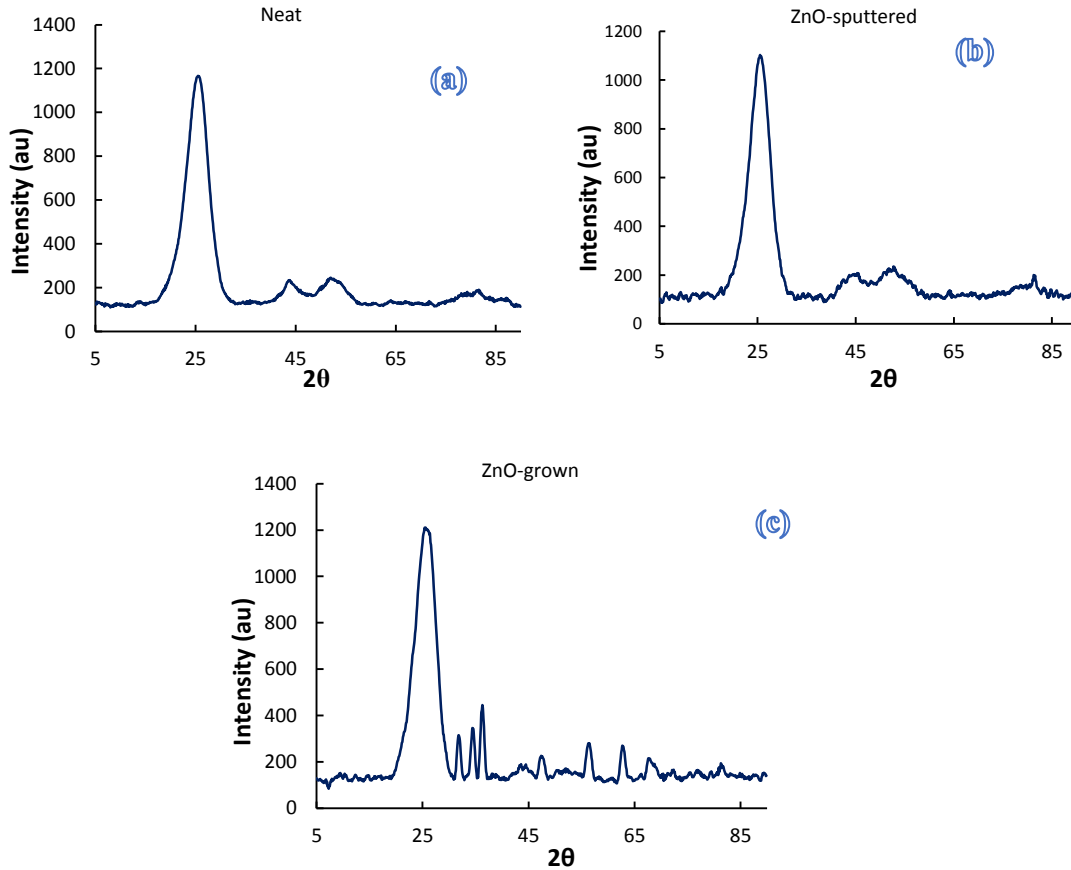


Figure 4.1. XRD patterns for a) Neat carbon fiber, b) ZnO film sputtered on carbon fiber and c) ZnO-grown nano rods on carbon fibers.

The appearance of the ZnO characteristic peaks in this configuration verifies that the hydrothermal synthesis technique yields fully crystalline ZnO nano rods, unlike the amorphous layer out of the sputtering deposition. Figure 4.2 depicts SEM fractographs for the composites cross sections. It is clear that the hydrothermal synthesis technique yielded relatively long nano rods with uniform distribution. Also it can be observed that despite the high vacuum applied during the layup fabrication, the ZnO nano rods maintained good attachment to the carbon fibers surfaces.

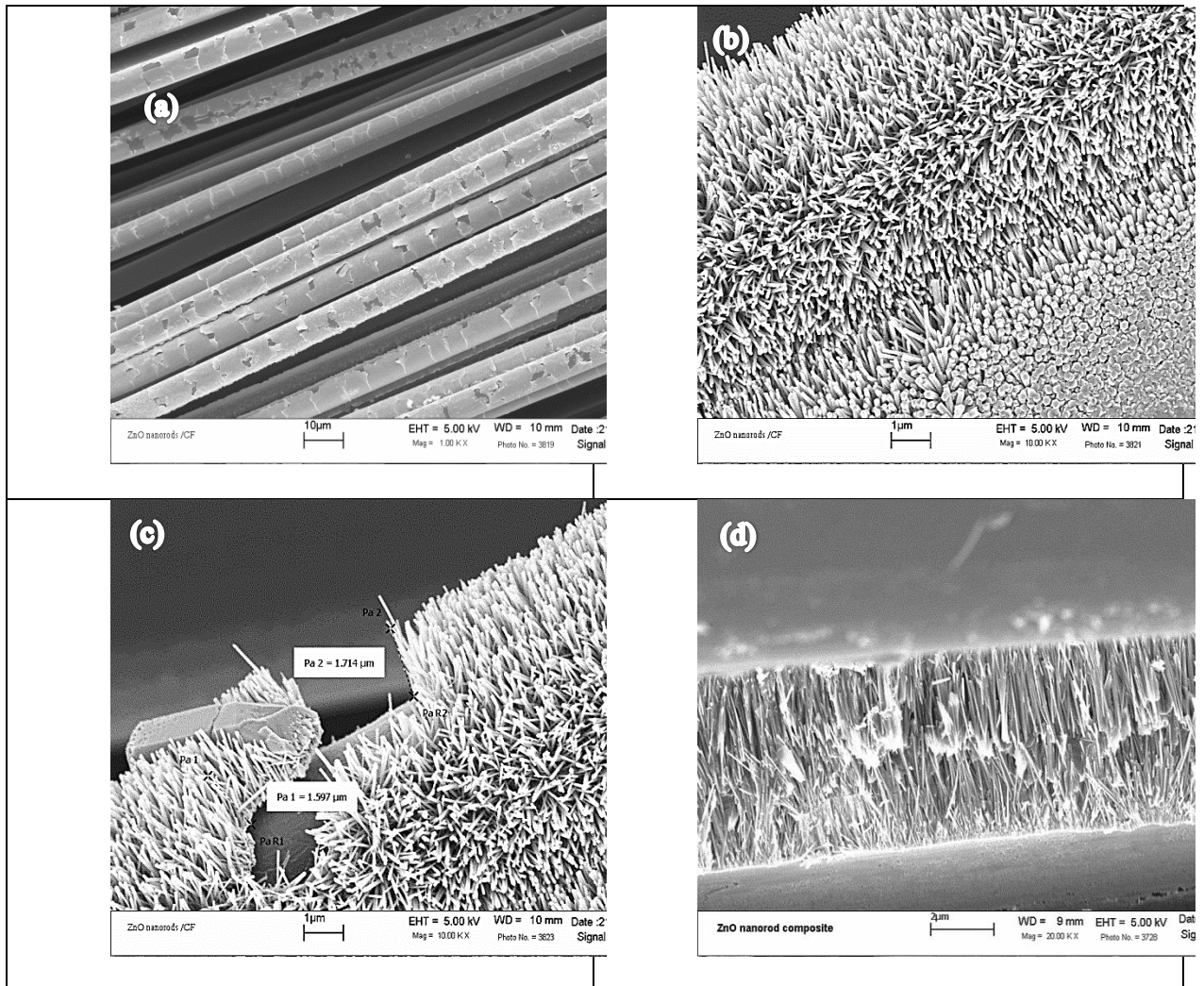


Figure 4.2. SEM micrograph of hydrothermally grown ZnO nano rods a-c) before and d) after hand lay-up process.

Figure 4.3 shows the linear viscoelastic stress-strain regimes for the three configurations: composite samples based on neat carbon fibers are denoted by “Neat”, samples based on carbon fibers sputtered with amorphous ZnO layer and undergone water soaking are labeled as “ZnO-

sputtered” and the composites based on carbon fibers with both sputtered ZnO layer and hydrothermally grown ZnO nano rods are identified as “ZnO-grown”.

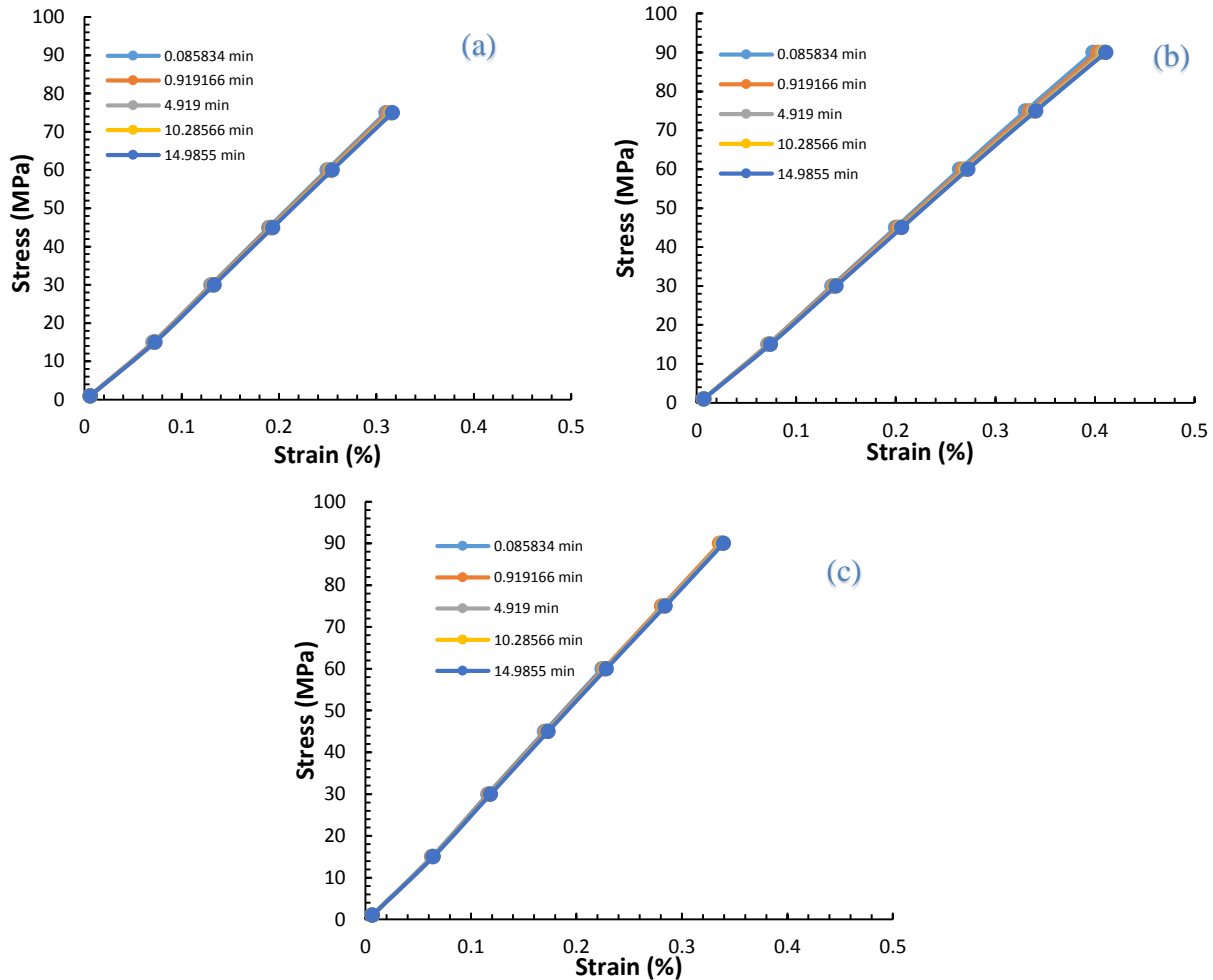


Figure 4.3. Linear viscoelastic regimes of a) Neat, b) ZnO-sputtered & c) ZnO-grown composite samples.

To determine the linear viscoelastic regimes for the different composites, they were subjected to varying stress/strain levels in incremental time steps ranging from 0.09 min to 15 min then the corresponding stress/strain curves were plotted. After determining the linear elastic range

of each sample, 15 min creep tests were performed under 20 MPa stress and the results were superposed to form the final master curve shown in Figure 4.4. To show the repeatability of the results, each curve in Figure 4.4 is an average of the data obtained from five different samples and the corresponding standard deviation is reported in Table 4.1.

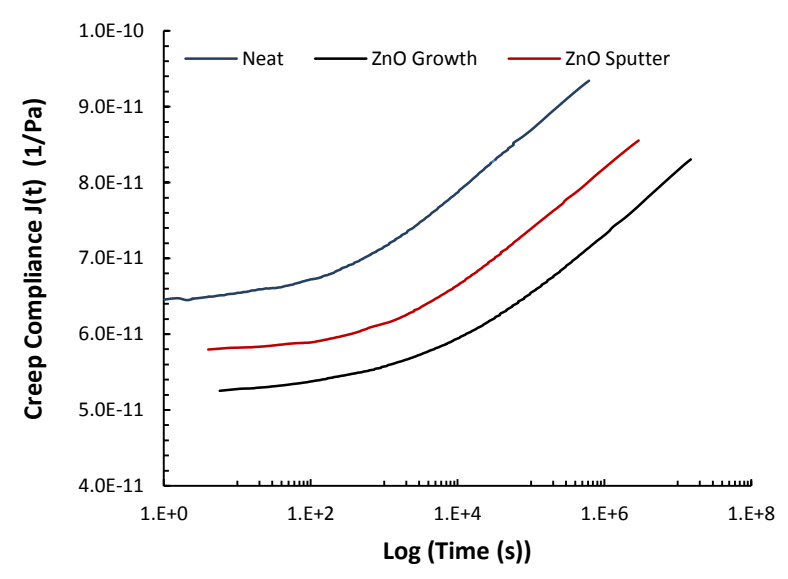


Figure 4.4. Creep compliance master curves for the different composites.

By examining Figure 4.4 it can be interpreted that the neat composite sample attained the highest creep compliance compared to the two other configurations. The presence of the ZnO amorphous layer in the ZnO-sputtered samples (including soaking in 80 °C water bath for 6 hrs with no nano rods growth) improved the creep resistance of the samples. Furthermore, the addition of ZnO nano rods decreases the creep compliance of the sample significantly without altering the weight or density of the samples. Table 4.1, summarizes the improvement of the creep compliance for each configuration. The amount of shifts, which were applied to superpose the data from short

isothermal creep tests to the final master curve, were analyzed to obtain the shift factors (a_T) as a function of temperature. Two well documented models are available for describing the (a_T) as a function of temperature; the Williams-Landel-Ferry (WLF) and Arrhenius models^{161, 162}. In this study, the shift factor data from all three configurations attained better fit using the WLF model; for example Figure 4.5 establishes the suitability of the WLF model for fitting the data of the ZnO-grown sample. Equation 4.5 describes the WLF model where logarithm of a_T is related to each temperature (T) and the reference temperature (T0) where C1 and C2 denote empirical constants for a given reference temperature.

$$\log_{10}(a_T) = \frac{-C_1(T - T_0)}{C_2 + (T - T_0)} \quad 4.5$$

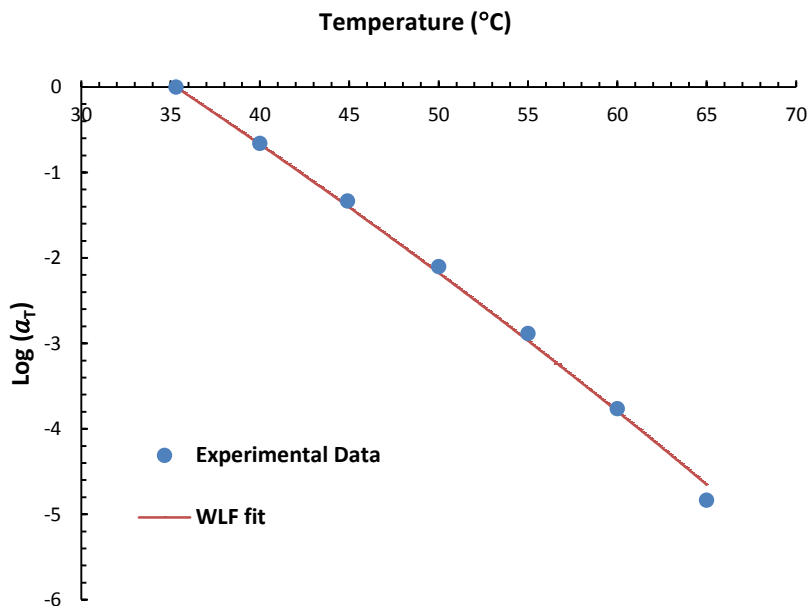


Figure 4.5. Shift factor evolution for composites based on carbon fiber with ZnO grown nano rods, experimental data were fitted using WLF model with C₁=-40, C₂=-285K.

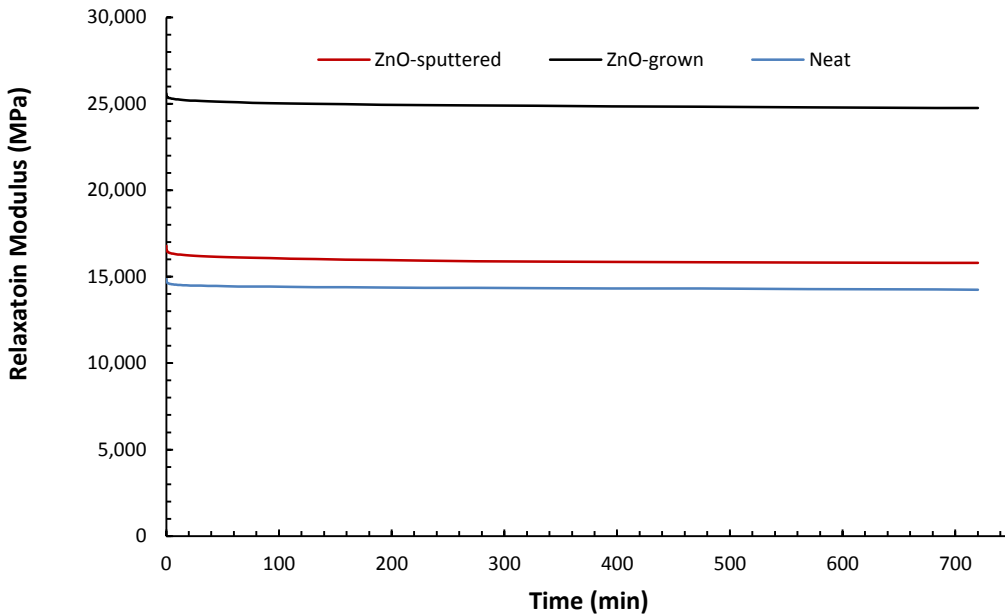


Figure 4.6. Prolonged stress relaxation data for all configurations.

Figure 4.6 depicts the measured stress relaxation curves for the three composites configurations, it can be seen that the neat sample possess the lowest relaxation modulus while the ZnO-sputtered shows a slight increase (10%) in the modulus. The ZnO-grown samples attained the highest stress relaxation modulus by far; over 65% more than that for the neat sample. Table 4.1 summarizes the amount of improvement of the relaxation modulus for the ZnO based samples with respect to the neat sample.

Sullivan reported the dependence of the sing of C_1 and C_2 on the test temperature range; for temperatures higher than T_g , C_1 and C_2 are expected to be positive whereas at lower temperatures they acquire negative values¹⁶³. One way to validate the superposed master curves is through real time prolonged relaxation experiments. In this study we utilized the inverse

proportionality of the creep compliance and relaxation modulus to ensure the validity of the creep master curves and also to compare the three composites configurations in terms of their relaxation moduli.

Table 4.1. Differences in creep compliance and stress relaxation modulus for each configuration with the standard deviation.

	Neat	ZnO-sputtered	ZnO-grown
Mean of relative standard deviation	5%	2%	4%
Reduction in creep compliance compared to neat sample	-----	14%	23%
Increase in relaxation modulus compared to neat sample	-----	10%	65%

Dynamic mechanical analysis (DMA) tests can provide the viscoelastic properties of a material such as the storage modulus (E') as measure of dynamic stiffness, loss modulus (E'') as a measure for energy dissipation and the tangent of phase angle between the stress and strain vectors linking these two moduli ($\tan(\delta) = \frac{E''}{E'}$). Figure 4.7 depicts the plots of the storage and loss modulus and $\tan(\delta)$ for all the samples in a frequency range of 1-25 Hz and strain of 0.1% at ambient temperature. It can be discerned that the storage modulus is not frequency-dependent whereas $\tan(\delta)$ varies dramatically with the frequency. The sputtered and growth samples exhibit identical storage moduli, however, they are slightly lower than that for the reference samples (raw).

On the other hand, $\tan(\delta)$ for the composites samples with ZnO growth is considerably higher in comparison with the other three samples. At lower frequencies the composites with ZnO

nano rods showed up to 50% improvement in passive damping compared to the other samples. The main contributors to this enhanced damping are the frictional and slippage mechanisms in the presence of high surface area/high aspect ratio ZnO nano rods.

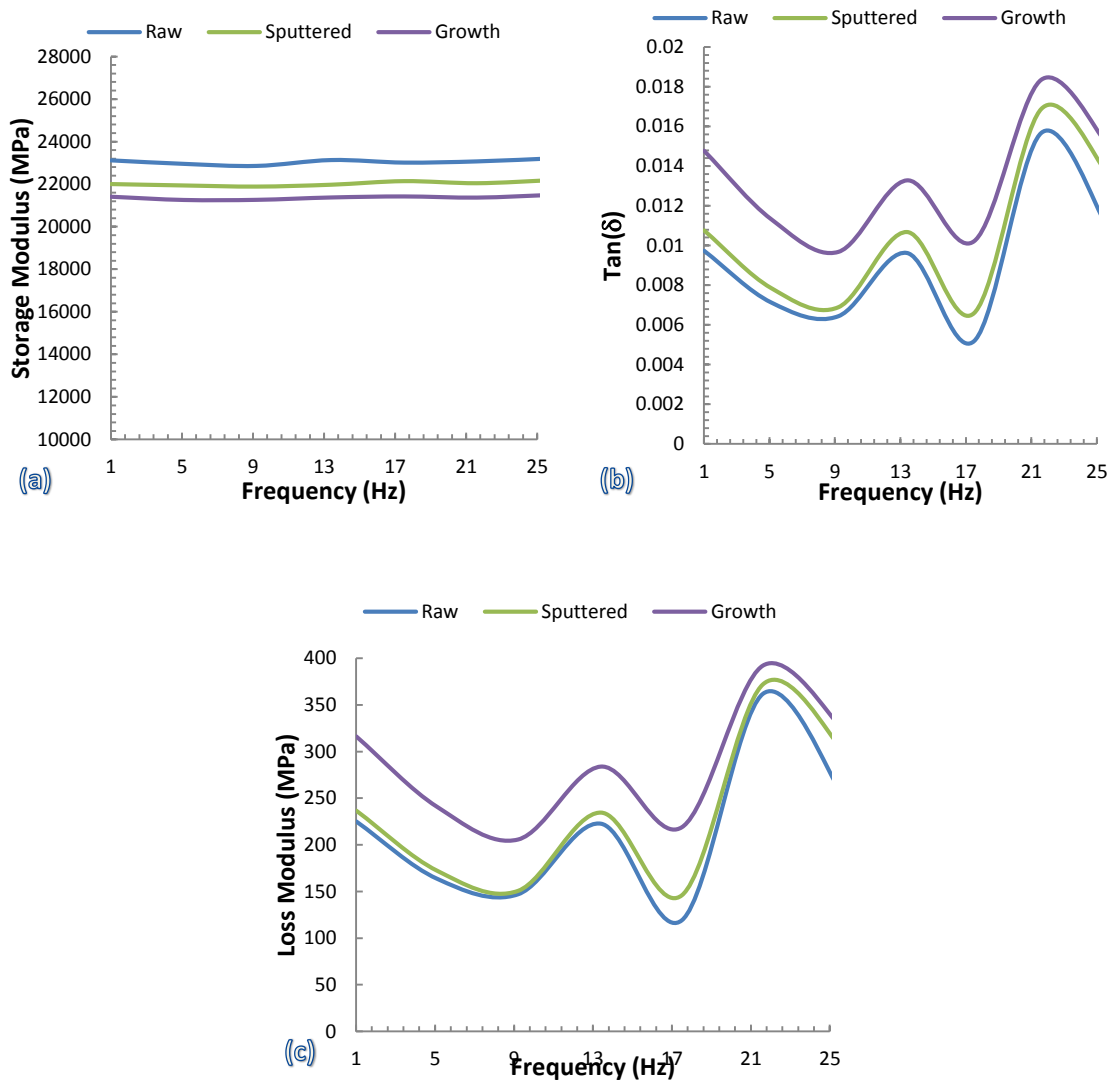


Figure 4.7. a) Storage modulus, b) $\tan(\delta)$ and c) Loss modulus for composites made out of raw (non-processed), sputtered (ZnO coated and soaked in solution) and growth (with surface grown ZnO nano rods) woven carbon fibers.

A slighter portion of this damping can be attributed to the piezoelectric effect of ZnO which is in agreement with several reports on the damping properties of ZnO particulates when embedded in polymer matrices as a result of their electromechanical coupling¹⁶⁴⁻¹⁶⁶. It is also observed that the samples sputtered with ZnO but with no nano rods growth showed improved damping over the raw sample, which can be attributed to the increased interfacial surfaces between the fibers and the sputtered ZnO layer.

4.4. Conclusions

In this study it was shown that fully crystalline ZnO nano rods could be grown on the surface of carbon fibers utilizing hydrothermal synthesis with minimal degradation of the fibers. The viscoelastic behavior of the hybrid ZnO nano rod/carbon fiber composites were investigated using both accelerated and prolonged methods. It was shown that accelerated methods such as the TTSP could be successfully applied to these composite in spite of their hierachal architecture with acceptable repeatability.

The DMA flexural creep tests revealed that the whiskerization of carbon fibers with ZnO nano rods reduces the creep compliance by 23% in comparison to composites based on neat carbon fibers. The better viscoelastic response of hybridized composites can be explained in terms of several micro and macro scale mechanisms. The dominant effect of ZnO nano rods on reducing the creep compliance comes from the fact that they serve as physical obstacles slowing down the rearrangement and slippage of polymeric chains (main mechanism for creep and relaxation of polymers). Moreover, modifying the interfacial area via the addition of ZnO nano rods enhances the polymer/fiber adhesion and thus hampers the creep deformation in the CFRPs.

The obtained creep data was also verified utilizing the inverse proportional relationship between the creep compliance and the stress relaxation modulus. Long term relaxation tests disclosed a considerable high relaxation modulus for composites with surface grown ZnO nano rods; the stress relaxation modulus improved by 65%, which is in agreement with the low creep compliance obtained from the TTPS master curves. Also DMA tests proved them to be advantageous for structural damping applications. The enhanced damping properties of the hybrid composites are attributed to the frictional sliding mechanisms of the high surface area/high aspect ratio ZnO nano rods grown uniformly throughout the FRP. This attenuation can also be related in part to electromechanical coupling of ZnO as well.

|Chapter 5

5. Viscoplastic Characterization of Hybrid Carbon Fiber/ Nano Phase Reinforced Composites

§

Abstract: *To date, the impact of surface grown ZnO NWs on the FRPs visco-elastoplastic deformation has not been investigated yet. The goal of this chapter of the dissertation is to demonstrate the applicability of whiskerization of ZnO nano rods, MWCNTs or a combination of both on conventional woven carbon without degrading the fibers structural properties. The resultant hierachal reinforcement was utilized to fabricate laminated FRPs. The hybrid composites were investigated toward characterizing their viscoelasto-plastic behaviors and ultimately compare the benefits of the hybrid composites against standard FRPs with neat carbon fibers. The major contribution is to shed some light on the phenomenological aspects of carbon FRPs in the presence of the nano phase. The collected data from the proposed extensive*

§ Article under preparation

experimental tests were utilized to both construct and validate the viscoelasto-plastic constitutive behaviors of the hybrid FRPs through phenomenological modeling scheme.

5.1. Introduction

Structural composites including those reinforced with high performance fibers (glass, carbon, aramid or their combinations)- due to their elevated specific strengths and moduli - have long been considered as alternative materials for structural applications ¹²⁹. However, the migrating applications of fiber reinforced plastics (FRPs) from conventional applications to high temperature applications, where both longer life cycles and durability are desired, make it crucial to investigate their time/temperature dependent properties further. As embodiments of temporal thermo mechanical behaviors of FRPs creep and stress relaxation are of particular importance as they directly affect the strength and durability of parts or structures made by FRPs. These deformations or changes in the material properties derived or amplified by exposure to prolong times are referred to as viscoelasto-plastic deformations. Polymer matrix composites are prone to growing deformation under constant loads (creep) and bare lesser load under constant displacement (stress relaxation) in long time periods. The time dependent deformations should be accounted for in the design of FRP structures as it could affect the load bearing capability and might induce structural instabilities. The main source for the viscoelasto-plastic deformations in FRPs is the polymeric matrix itself where the constituent chains tend to slide against each other and straighten. This initially small deformations and rearrangements pile up to generate a measurable deformation and stress relaxation.

Although the addition of carbon fibers extemporize the mechanical properties of the polymers considerably -including their viscoelasto-plastic resistance-; some other phenomenological issues arise when these micro-scale fibers, which contributes to the time/temperature driven viscos deformations, are added. Straightening of the fibers from their possible initial waviness and more notably the slippage mechanisms between the fibers and matrix are the major contributing factors to viscoelasto-plastic deformations in FRPs.

The insufficient viscoelastic resistance of fiber reinforced plastics (FRPs) can be mitigated by the addition of more rigid nano fillers to the polymer based matrix. Nano particle fillers applied extensively to modify the viscoelasto-plastic behavior of polymer matrix composites ¹³³. The existence of nano particle fillers can compensate for the viscous properties of polymers up to an extent; however it brings about other changes such as increasing the weight, reducing the ductility, altering the electrical/thermal insulation properties. The amount of change depends on the volume fraction of the particles, their morphology and ultimately their adhesion to the matrix. In the case of nano particles with high Van der Waals type forces between them (such as carbon nano tubes), the lack of dispersability becomes detrimental if the volume fraction exceeds a certain metric called the percolation threshold. The percolation threshold is considered to be the minimum volume fraction at which a filler can uniformly be dispersed in a matrix properly to form a 3D connected network throughout the matrix without agglomeration. Most research to date focuses on using CNTs as reinforcements, or as fillers, in a polymeric matrix by dispersing and perhaps subsequently aligning single- or multi-walled CNTs in the matrix ^{167, 168}. Alignment and dispersion are critical factors that are difficult to control experimentally using oft-repeated mixing methods. Carbon nano tubes embedded in a polymeric matrix form aggregates of themselves that are not

only poorly adhered to the matrix, but also concentrate stresses, compromising the contribution of the CNTs as reinforcement. Sonication¹⁶⁹ and calendaring¹⁵⁷ have been used to mitigate this problem, but are not effective beyond ~3% CNT volume fraction due to the formation of aggregates¹⁷⁰. The extreme difficulty in uniformly dispersing CNTs in polymer matrices arises from the large surface area of CNTs¹⁷¹. Dispersion and extrusion techniques have been reported in the literature for producing CNT composites¹⁷². However, in both dispersion and extrusion techniques, producing uniform and well-dispersed CNTs reinforced composite is difficult because of the small amount of solid ‘powder’ (carbon) compared with the large amount of liquid polymer (matrix) in early mixing stages. This often leads to phase separation due to the strong van der Waals forces between CNTs compared with that between CNTs and polymer¹⁶⁸.

Several remedies were suggested to enhance the fiber/matrix interface and thus hinder the slippage mechanism between the fibers and the matrix encountered in visco-elastoplastic deformations. The chemical treatment approach utilizes acidic reagents (e.g. chlorosulfonic acid, nitric acid, etc...) to attach functional groups such as carboxyl, ether or hydroxyl to the fiber to improve the load transfer and adhesion between the fiber and the matrix. It was demonstrated that the chemical treatment improves the wettability and the surface roughness of the fibers, which, in return, increase the tensile strength, and the interlaminar shear strength of the composite. However, the chemical treatments might induce excessive erosion to the fiber leading to a reduced composite strength. In return, the in-plane mechanical properties of the composite could be compromised to improve the interface strength.

A simple, yet practical, remedy to hinder the slippage mechanism between the fibers and the matrix can be achieved via the creation of well-attached, small-scale physical obstacles on the fibers (whiskerization). Whiskerization can resolve the dispersability and agglomeration issues discussed earlier as no physical mixing is needed. The whiskers could be high aspect ratio crystalline silicon carbide, silicon nitride or carbon nano tubes (CNTs) grown on the surface of the fibers. The growth of high aspect ratio nano tubes on the fiber surface induces less stress concentration in the fiber since they introduce stiffness gradient from the fiber to the matrix¹⁷³. The growth of 1D carbon nano structures (multi and single wall carbon nano tubes) and ZnO nano rods on commercially available carbon fibers has been demonstrated at different studies^{123, 131, 132}. Carbon nano tubes were grown on carbon yarns and carbon fabrics surface using the catalytic chemical vapor deposition (CCVD) with different catalysts such as nickel, cobalt and iron at high temperatures (600°C to 1000°C). Zhang et al¹⁶⁶ have grown high density multiwall carbon nano tubes (MWCNTs) using the CCVD process at high temperatures 700-800°C on the surface of sized and un-sized carbon fibers. The results showed a 40% decrease in the tensile strength of the sized carbon fibers when exposed to 700°C growth environment. Identical results were observed for the un-sized fibers but at temperatures higher than 800°C which contrasts the important role played by the fibers sizing. Like CNTs, zinc oxide (ZnO) nano wires (NWs) can be grown on carbon fibers' surface to enhance the interface between the fibers and the matrix. Zinc oxide possesses semiconductor and piezoelectric properties which makes it well-suited for variety of applications from solar cells, sensors, structural applications, to energy harvesting devices¹⁷⁴⁻¹⁷⁷. Different synthesis protocols were developed to grow ZnO nano structures such as vapor-phase transport, metalorganic chemical vapor deposition (MOCVD), sputtering, molecular beam epitaxy (MBE),

thermal evaporation and vapor-liquid-solid (VLS)¹⁷⁸. These techniques are time-consuming and/or require elevated synthesis temperatures, which limit their use for industrial applications.

Despite their extraordinary physical properties, there are few reports on the effect of ZnO as interfacial reinforcement for FRPs. Lin *et al.*¹⁷⁹ tested the shear strength of a single carbon fiber wrapped with ZnO NWs and reported 113% increase in the interfacial shear strength. Ehlert *et al.*¹⁸⁰ utilized identical ZnO growth process on aramid fiber and suggested that the carboxylic acid group is responsible for the good interfacial shear strength between the ZnO NWs and the carbon fiber. While these results highlight the compatibility of ZnO NWs as reinforcing whiskers in composite structures, they are limited to a single isolated fiber surrounded with an epoxy matrix. Since the carbon fibers and the grown 1D nano whiskers are of different size and nature, the term “hybrid nano composite” is used throughout the text to address the whiskerized carbon FRPs.

5.2. Materials, Processing and Experimental Techniques:

5.2.1. Samples Preparation

5.2.1.1. Sizing Removal from Fibers

PAN-based carbon fibers with 3k bundles from Thorne[®]l T650 (Cytec, Inc.) were utilized as the reinforcement throughout this dissertation. The sizing on the fibers was removed by placing the as received sized fibers in a tube furnace at 550 °C for 30 mins under inert environment (nitrogen). The de-sized fibers are afterward employed in a three-layer polymer matrix composite to further investigate the effect of the sizing removal on the mechanical properties of the

composite. Figure 5.1 summarizes the mechanical properties of the composites made of fibers exposed to 550 °C for different duration to measure the amount of the degradation which is imposed to the fibers. It can be seen that exposure to 550 °C for 30min under inert atmosphere did not alter the mechanical properties of the fibers considerably while scanning electron microscopy (SEM) images did not show any trace of polymeric sizing leftover on the fibers (Figure 5.3(a)).

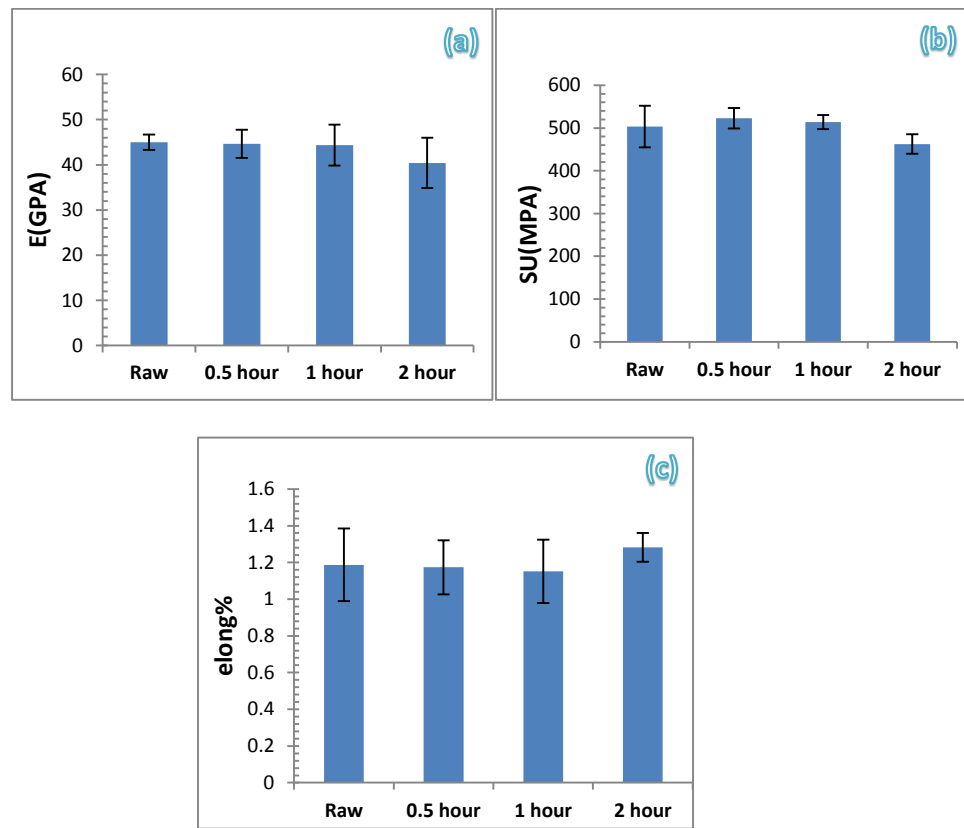


Figure 5.1. Effect of the duration of exposure to high temperature on the fibers a) Elastic moduli, b) Ultimate strength and c) Elongation at failure.

5.2.1.2. Growth of ZnO Nano Rods and CNTs

ZnO nano rods were grown via an aqueous solution of zinc acetate $\text{Zn}(\text{O}_2\text{CCH}_3)_2$ as the source for Zn^{2+} ions in water where H_2O molecules supply the O^{2-} ions as described earlier in details in chapter 3. Carbon nano tubes were grown utilizing the GSD method. The carbon yarns were placed, separately, inside a quartz tube furnace. Three mass flow controllers were required for the three input gases: an inert gas (UHP N_2), a hydrocarbon (C_2H_4), and Ultra High Purity H_2 . The synthesis processes consisted of three steps: (i) a reduction step, at 550 °C under N_2/H_2 environment, was carried out for 2 hours under atmospheric pressure to break the nickel film into nano meter sized particles and to remove any nickel oxides, (ii) flushing of the system with nitrogen to remove the reduction byproducts and, (iii) the introduction of the “deposition mixture,” which consisted of $\text{N}_2/\text{H}_2/\text{C}_2\text{H}_4$ while maintaining the temperature at 550 °C. The growth time was set to 30 minutes. A more detailed description of the GSD is explained by the inventors¹²³.

5.2.1.3. Composites Fabrication

The hybrid fabrics with surface grown ZnO, CNT and patterned-CNT were utilized to fabricate three layered composites via standard hand lay-up process. The layup arrangement was 0°/45°/ 90°. The middle layer orientation was chosen to further increase the matrix contribution to the overall mechanical properties. The matrix material was a resin-based epoxy, Aeropoxy™ manufactured by PTM&W Industries, Inc.

The mold used for fabrication consisted of two aluminum parts with a flexible rubber sheet separating them. The setup comprised a vacuum bag, peel ply release fabric, stacked carbon fabrics were impregnated with the epoxy (using a roller), another peel ply film, perforated release film,

and breather cloth, consecutively. The 3 layers layup was placed inside the bottom half of the mold, which is connected to the vacuum line, and the top part that has an airway (which is lastly connected to compressed air line) remained empty. While the layup being vacuumed, compressed air (480 KPa) was applied to it by the means of flexible separator. To seal the mold from the ambient, it was placed in a hydraulic press (operated at 30 tons). Simultaneous use of the vacuum, compressed air, and press assures degassing of the resin while the carbon fabrics were kept intact under high pressure. The composites were left for 24 hours to ensure full curing of the epoxy and then post cured at 85 °C for an additional 4 hrs to ensure complete curing of the samples.

5.2.2. Samples Characterization

5.2.2.1. Scanning Electron Microscopy (SEM), Thermal Gravimetric Analyzer (TGA)

Electron scanning microscopy (LEO (Zeiss) 1550 field-emission SEM) was utilized to study the size and morphology of the grown ZnO nano rods and CNTs as well as the possible effects of solution environment and heat-treating on the sizing of fibers. SEM was also used after hand lay-up process to study the inter-laminar space of composites in terms of delamination and other defects. To measure the weight/volume fraction of the fibers in different samples TGA (TA Q50) was employed.

5.2.2.2. Mechanical Testing

Tensile testing: An Instron testing frame was employed (with an environmental chamber mounted on it) to conduct the tensile tests and stress relaxation tests at 25°C, 45°C, 65°C, 85°C. To best probe the effect of the temperature on the viscoelastic properties of the polymeric matrix

of the samples, application of polymeric tabs was avoided and a flexible aluminum sheet was used to best grip the samples without imposing additional viscoelastic behavior to the samples. Also to minimize the heat latency of the metallic parts, smaller mechanical grips were chosen over their bigger hydraulic counterparts. The tensile and stress relaxation tests were performed according to the ASTM D3039/D3039M and ASTM D6048 standard methods.

Creep testing: A standard dead weight creep frame was augmented with pneumatic power, 5k lb load cell and data acquisition system. An air cylinder with both compression and expansion capabilities was installed on a dead weight frame and compressed air was supplied to air cylinder through high pressure piping system and a 0-30 psi manual regulator (Figure 5.2). A high temperature extensometer was utilized to record the elongation of the samples throughout the loading and creep processes. The data acquisition system consisted of a 4 channel full/half bridge NI USB-9481 National Instruments DAQ system. A LabView in-house code was developed to communicate with the DAQ system and do the calibration and data recording. A ± 10 DCV was supplied to the bridge as an input and the resultant output signal was scaled to their physical quantities via the information provided from the manufacturers of extensometer and load cell.



Figure 5.2. The fortified creep frame with pneumatic air cylinder and 5klb load cell.

5.3. Results and Discussion

The following terminology are used throughout the dissertation to identify different composites configurations:

- Neat (NT): Composite samples prepared from de-sized T650 fibers, Figure 5.3 (a) shows them after sizing removing.
- Heat Treated (HT): Composite samples prepared from de-sized T650 fibers, undergone the 4 hrs of 550 °C heat treatment to mimic the effect of CNT growth process (Figure 5.3 (b)).
- Substrate (SUB): Composite based on de-sized fiber cloth and sputtered with a 70 nm of ZnO amorphous layer using magnetron sputtering and water soaked for 4 hrs at 85 °C and after that kept 4 hrs at 550 °C to mimic the effect of CNT growth process (Figure 5.3(c)).
- ZnO-Growth (ZnO-G): Composites based on de-sized fibers, sputtered and then soaked in the growth solution for 4 hrs at 85 °C and then undergone the heat treatment similar to CNT growth process for 4 hrs at 550 °C (Figure 5.3(d)).
- CNT-Growth (CNT): Composite based on de-sized fibers, sputtered with a 70 nm ZnO amorphous layer and water soaked for 4 hrs at 85 °C are then coated with 2 nm of Ni layer all over the fibers and undergone CNT growth process for 4 hrs at 550 °C (Figure 5.3(e)).
- Patterned-CNT-Growth (Pat-CNT): Composite based on de-sized fibers, sputtered with a 70 nm ZnO amorphous layer and water soaked for 4 hrs at 85 °C are then coated with 2 nm of patterned Ni layer where Ni covers the fibers partially. The patterning were conducted utilizing a woven wire cloth, 316 SS, 90X90 Mesh, .0035" Wire Dia, masking the sample during the sputtering. The patterned Ni sputtered samples are then undergone CNT growth process for 4 hrs at 550 °C to get CNTs (Figure 5.3 (f)).

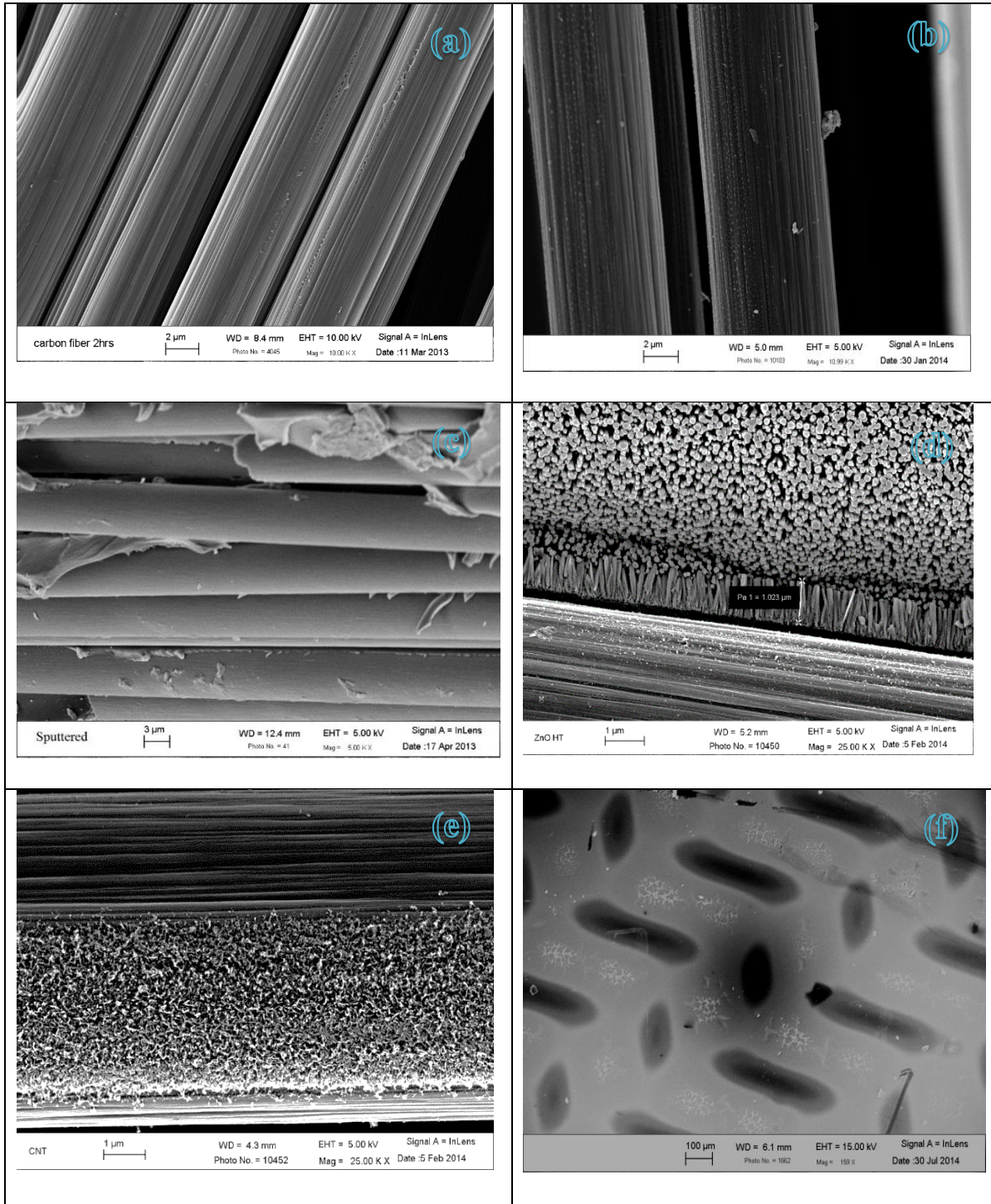


Figure 5.3. Different configurations of samples a) Neat, b) heat treated, c) Substrate, d) ZnO-G, e) CNT-G and f) patterned-CNT-G.

5.3.1. Thermo Gravitational Analysis (TGA)

Shown in Figure 5.4, the volume fraction of the polymeric matrix is extracted for each composite configuration. Disk shaped composite samples with 4mm diameter were cut randomly from different locations of the composite plates and tested in a TGA by ramping the temperatures at a rate of 20 °C per minute temperature from room temperature to 500 °C. The loss of weight from 150 °C to 500 °C is taken to be the amount of polymeric matrix which burns away during the heating. The weight loss prior to 150 °C can be related to the humidity absorbed in the composites. All of the samples contained a ~ 2 wt% moisture. It can be seen that the Sub sample has the lowest matrix portion while the patterned CNT sample attained the highest one. Later on the data for matrix volume fraction is going be used to normalize the viscoelastic/plastic properties as the major response to time/temperature dependent response of material arises from the polymeric matrix.

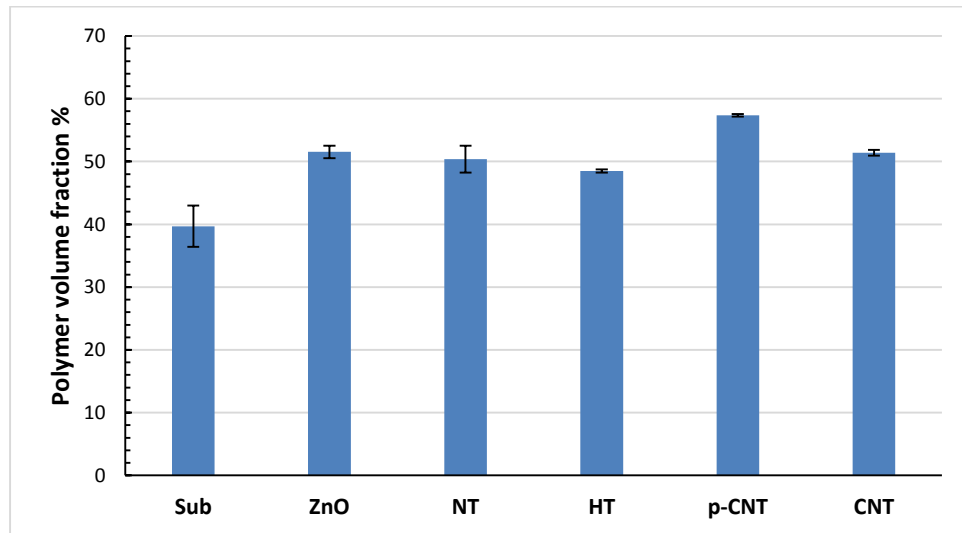
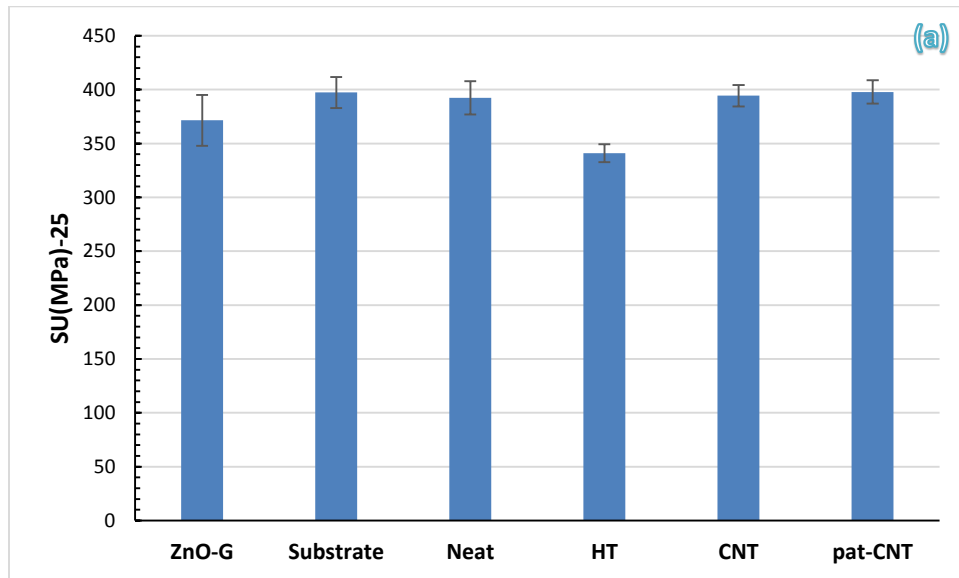


Figure 5.4. Volume fraction of the epoxy matrix in the different composite samples obtained via TGA.

5.3.2. Tensile Tests

Figure 5.5 to Figure 5.8 depicts the data from tensile tests at four different temperatures comparing different samples. It can be seen that HT samples pose the lowest ultimate strength and elastic modulus whereas CNT and Pat-CNT have the highest strength and elastic modulus. 6 tensile tests were done at each temperature and the average is reported including the standard deviation. It can be interpreted from the data that HT samples have the lowest strength while substrate and pat-CNT samples have the highest ultimate strength and elastic modulus almost at any temperature. The high strength of substrate samples can be explained by higher fiber fraction of these samples while the pat-CNT samples although high in matrix volume fraction, they still have comparable stiffness and strength.



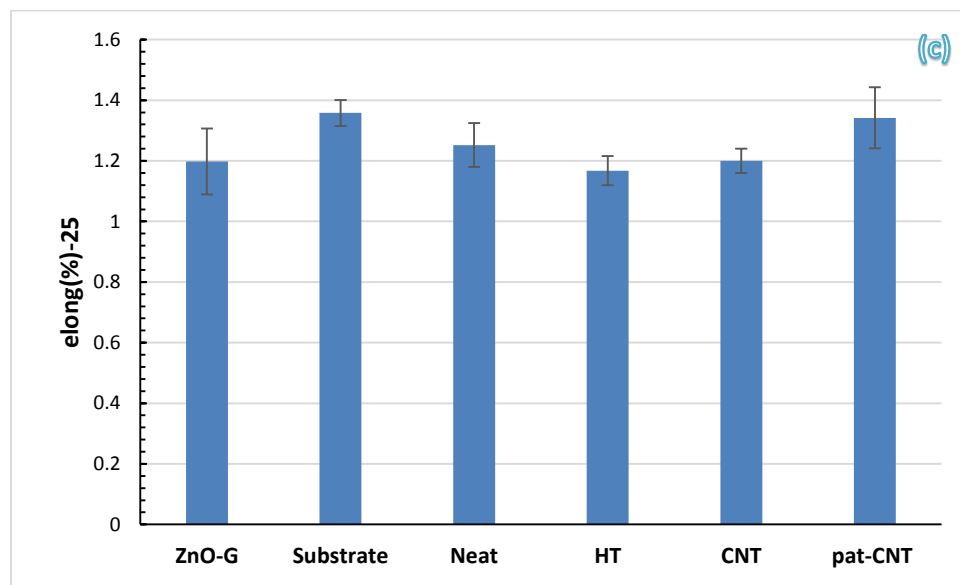
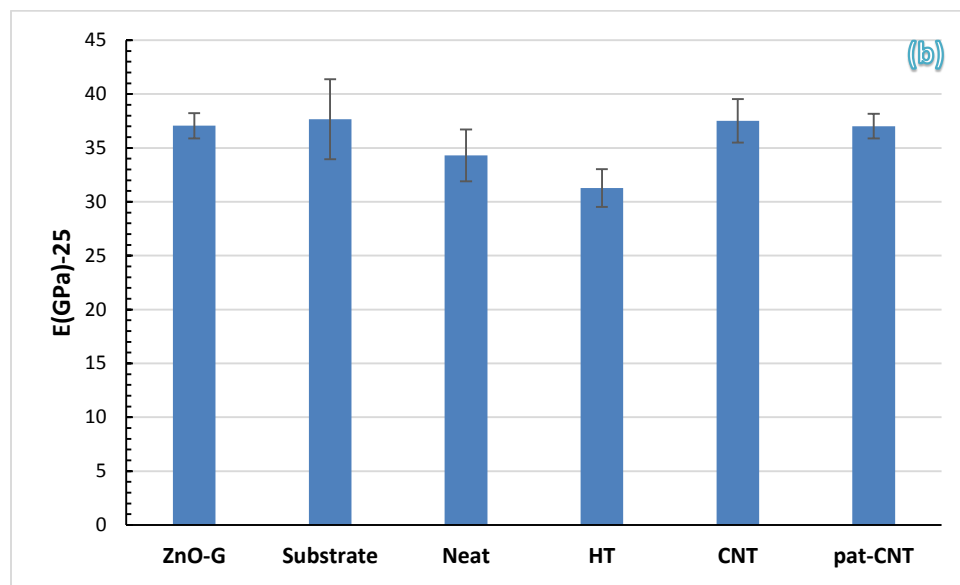
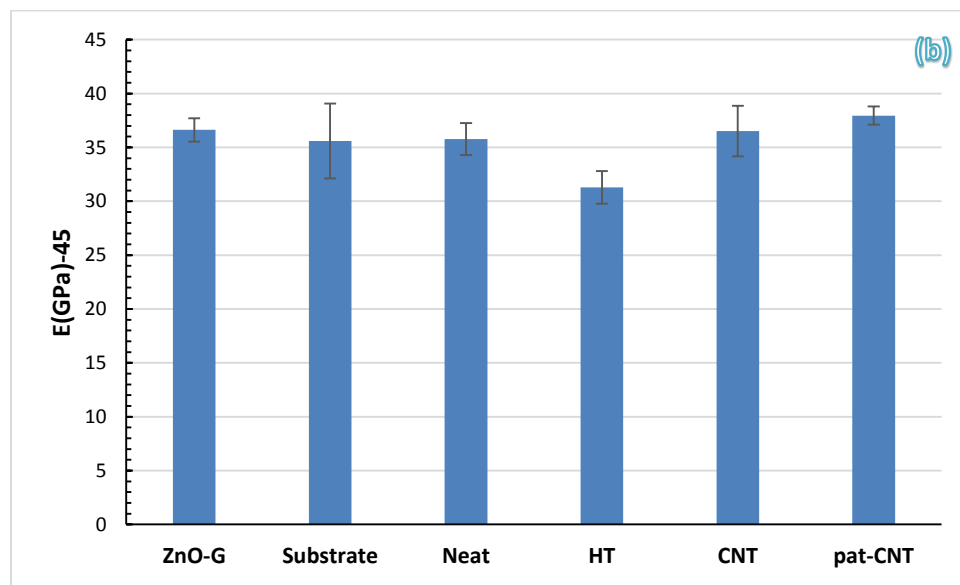
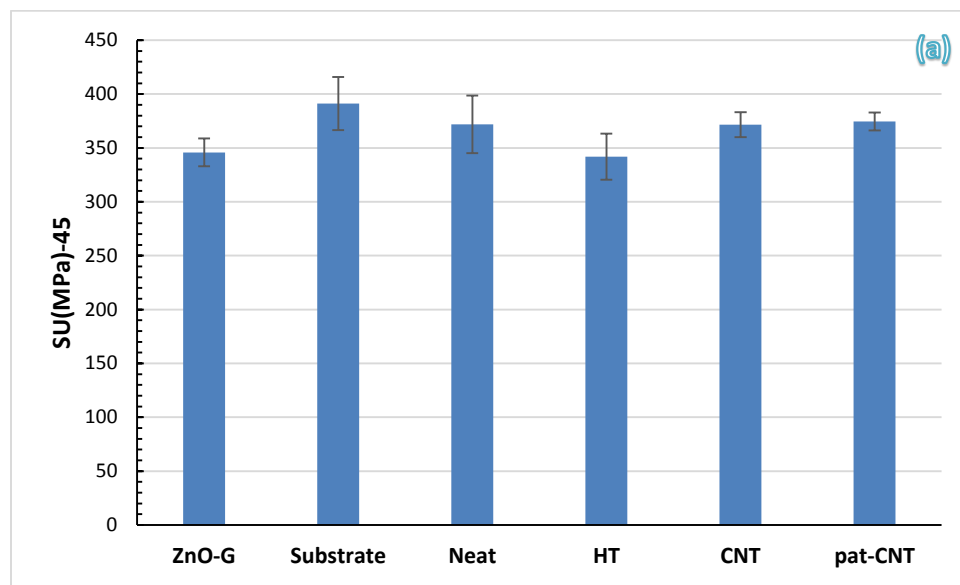


Figure 5.5. Mechanical properties of different composites configurations at 25 °C, a) Ultimate Strength, b) Elastic modulus and c) Elongation to failure.



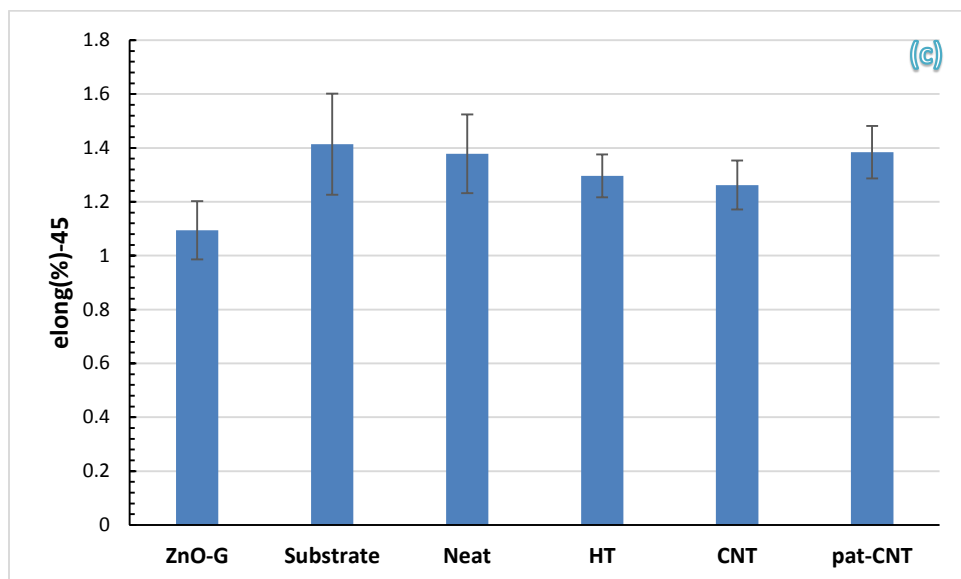
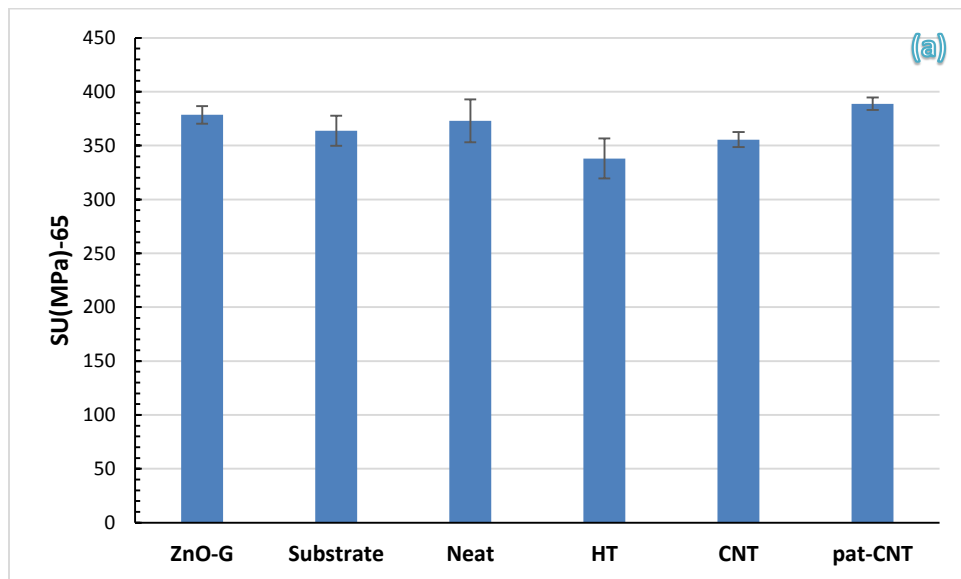


Figure 5.6. Mechanical properties of different composites configurations at 45 °C, a) Ultimate Strength, b) Elastic modulus and c) Elongation to failure.



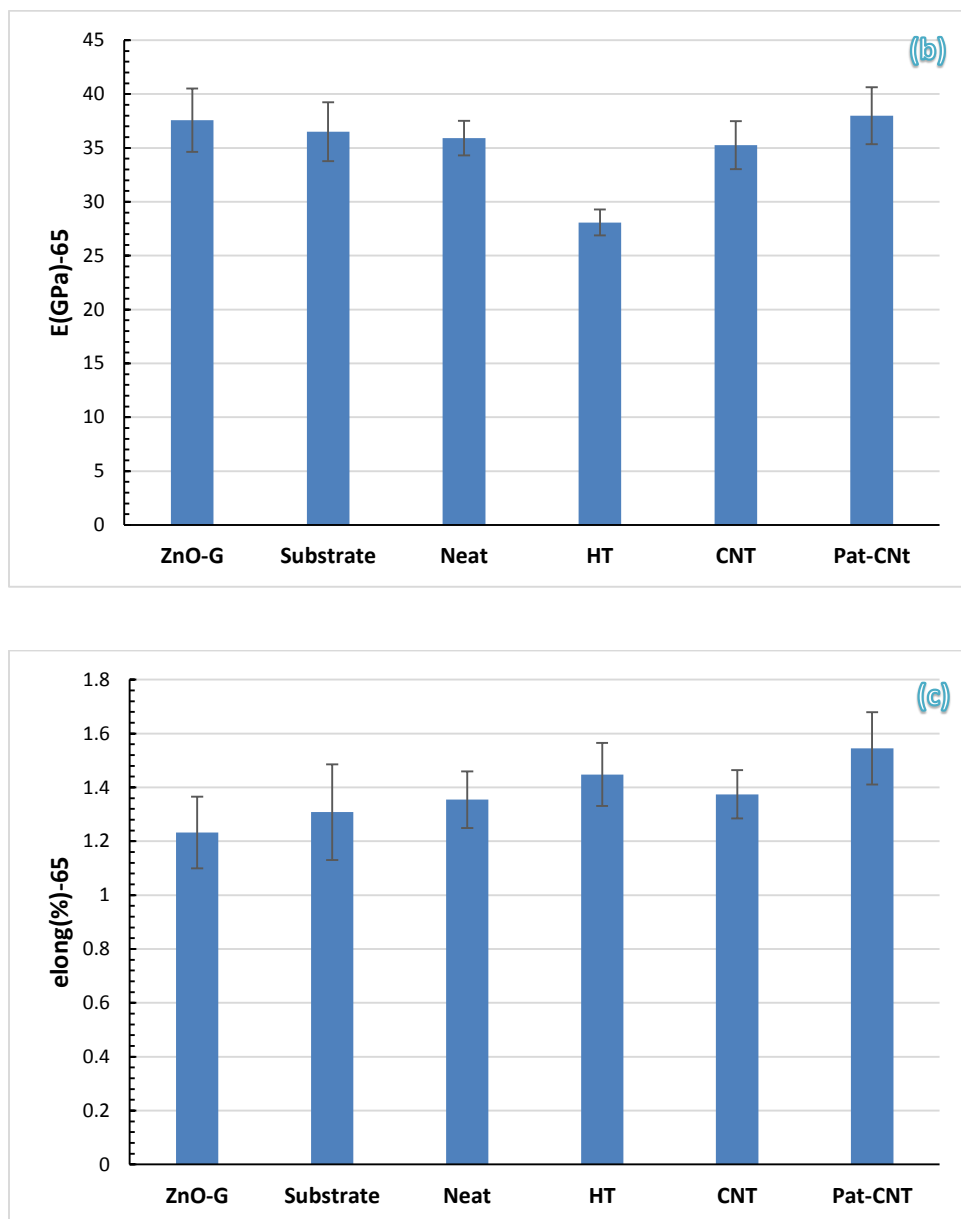
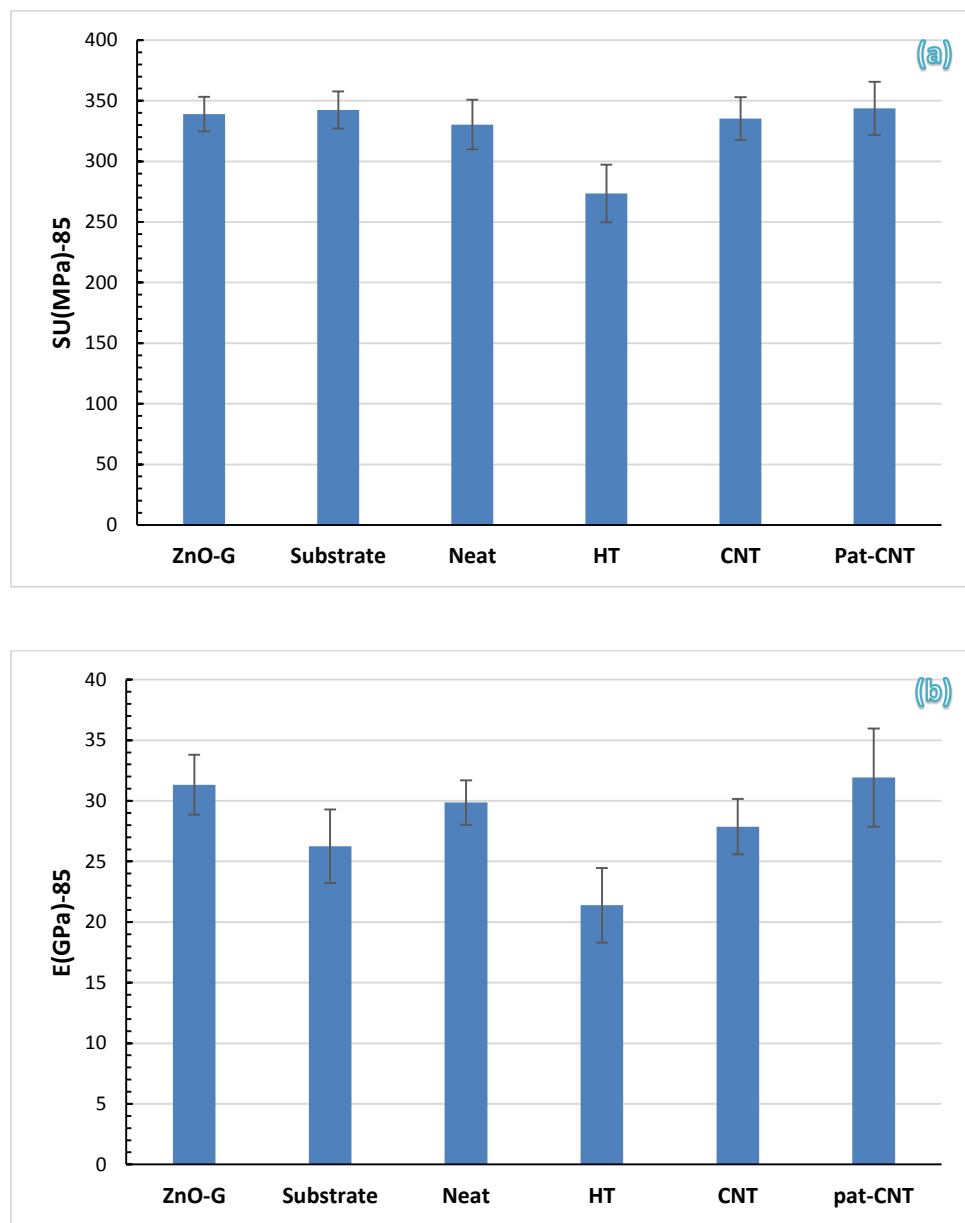


Figure 5.7. Mechanical properties of different composites configurations at 65 °C, a) Ultimate Strength, b) Elastic modulus and c) Elongation to failure.



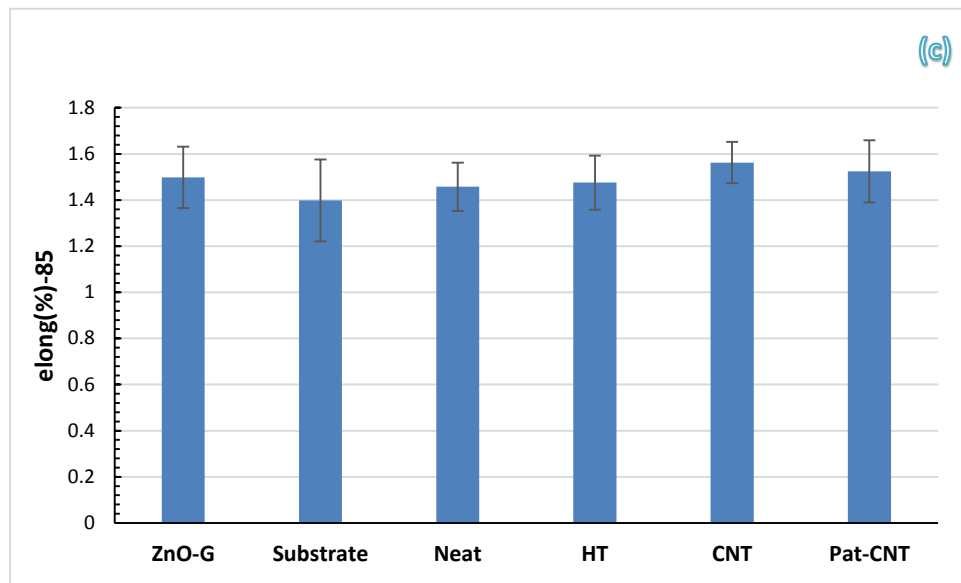


Figure 5.8. Mechanical properties of different composite configurations at 85 °C, a) Ultimate Strength, b) Elastic modulus and c) Elongation to failure.

5.3.3. Stress Relaxation

Stress relaxation tests were carried out at four different (strain levels) levels at each temperature. We took 20%, 40% 60% and 80% of the ultimate strength to be the four stress levels to determine the constant strain levels for relaxation tests at each temperature so that strain levels are a function of temperature as well. Figure 5.9 to Figure 5.14 show the stress relaxation at each stress level for all of the configurations. It can be inferred that at the combination of elevated temperatures and higher load levels the amount of relaxation in stress increases significantly.

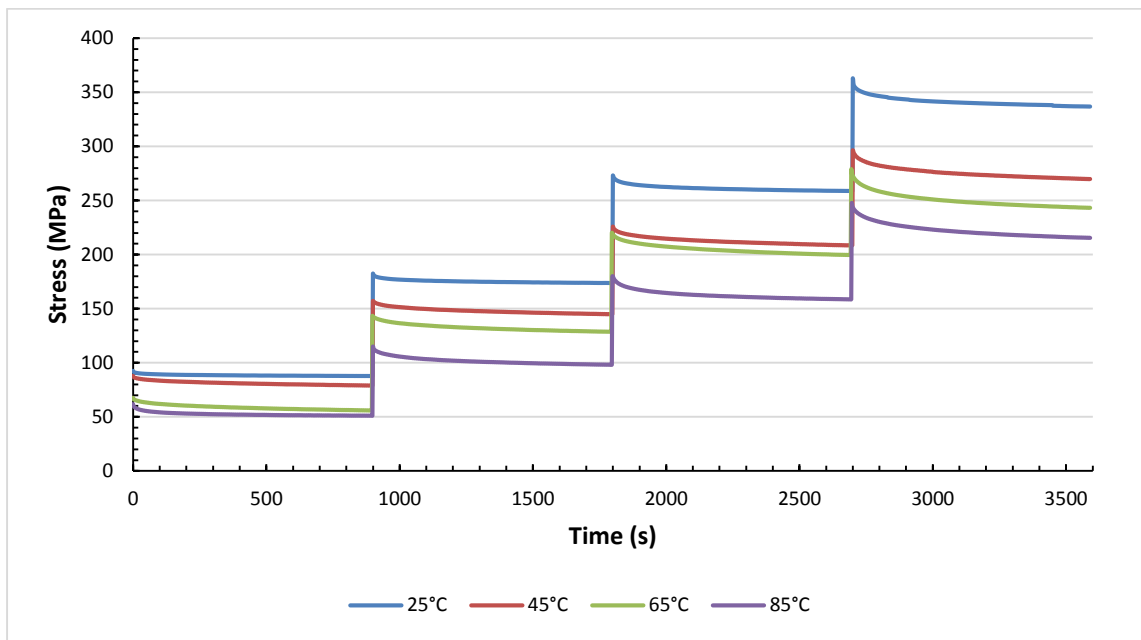


Figure 5.9. Stress relaxation curves for the Neat composite samples at different temperatures.

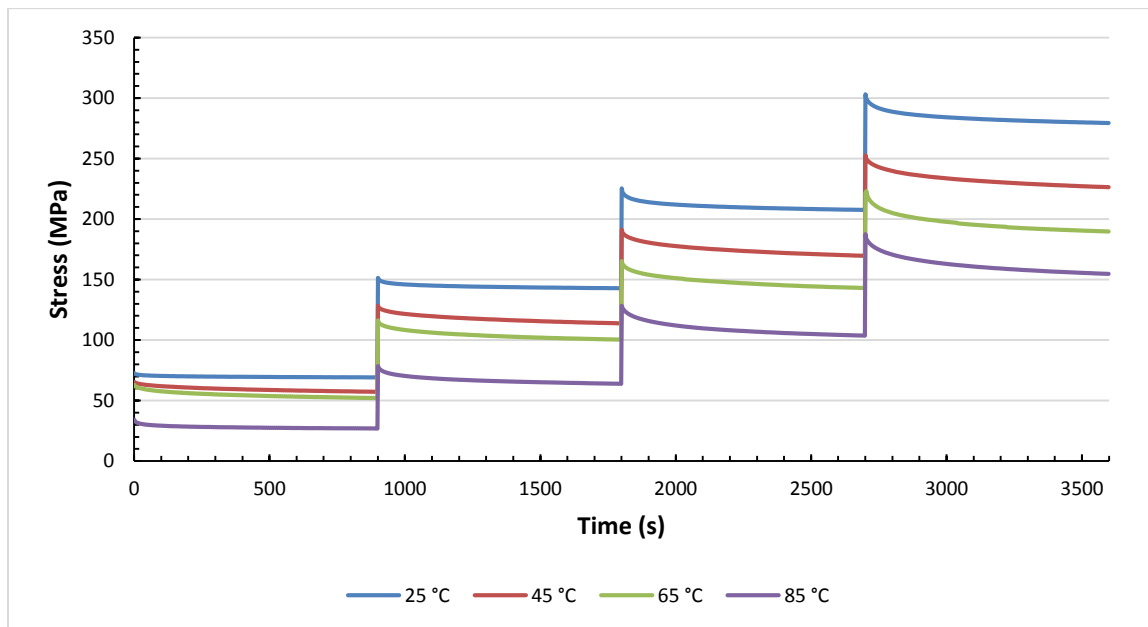


Figure 5.10. Stress relaxation curves for the HT composite samples at different temperatures.

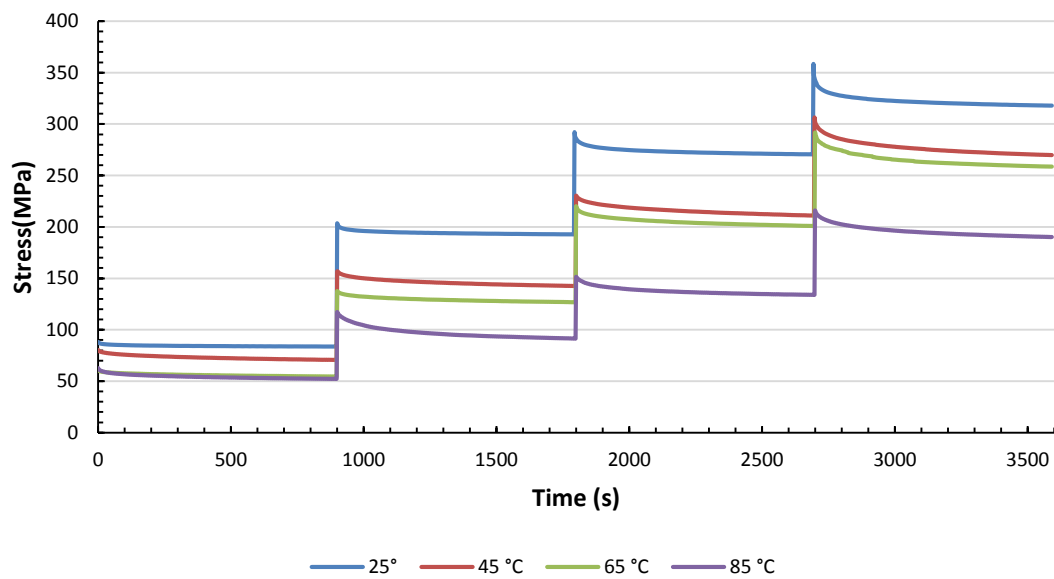


Figure 5.11. Stress relaxation curves for the Substrate composite samples at different temperatures.

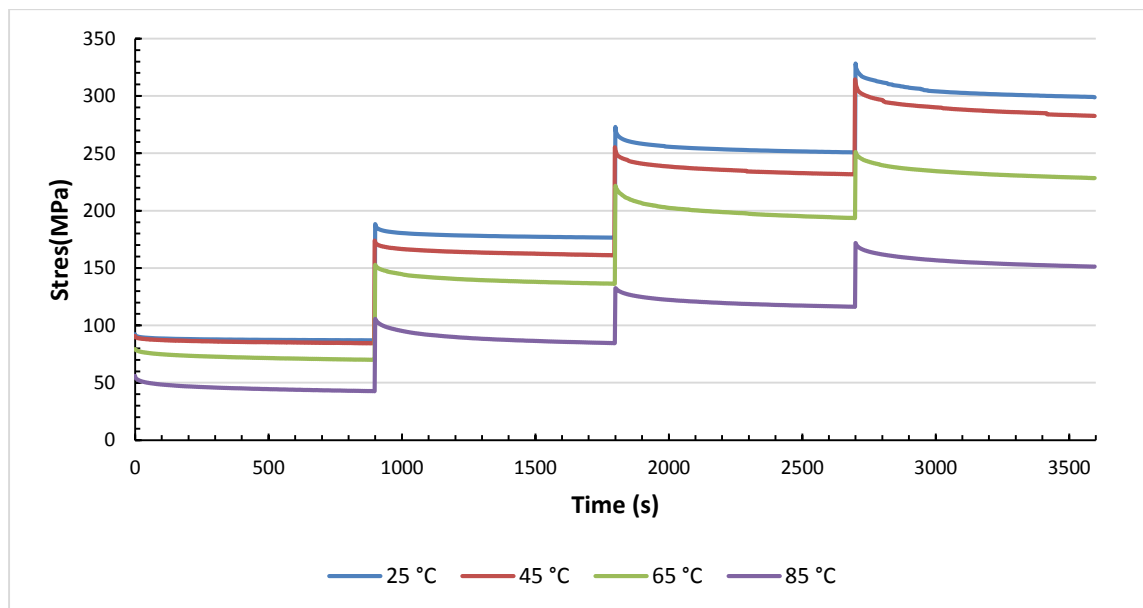


Figure 5.12. Stress relaxation curves for the ZnO composite samples at different temperatures.

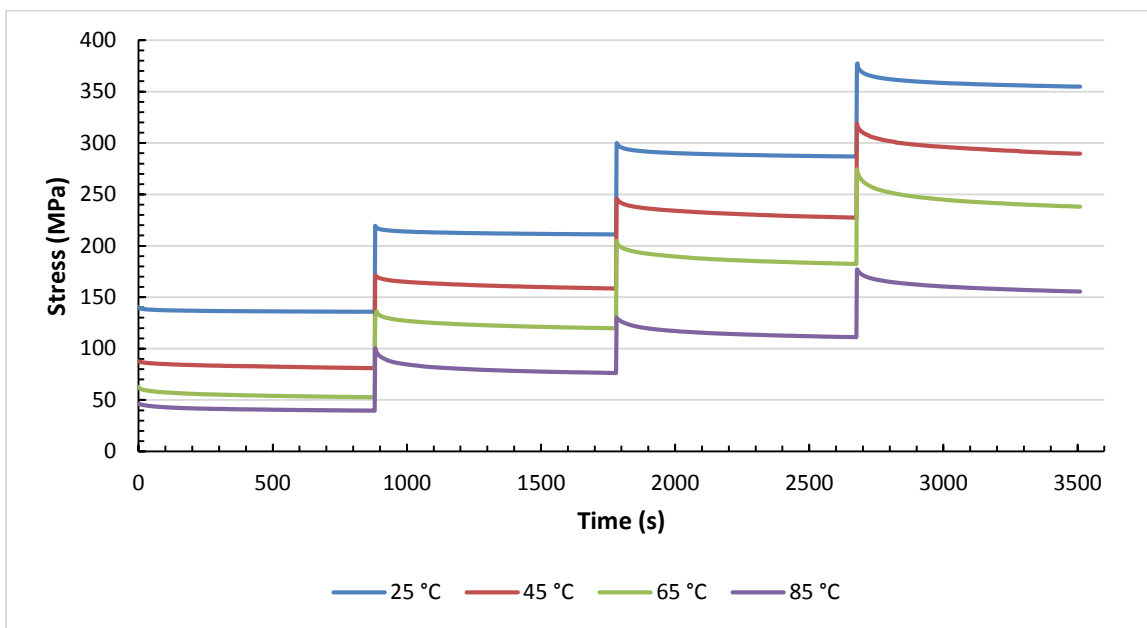


Figure 5.13. Stress relaxation curves for CNT composite samples at different temperatures.

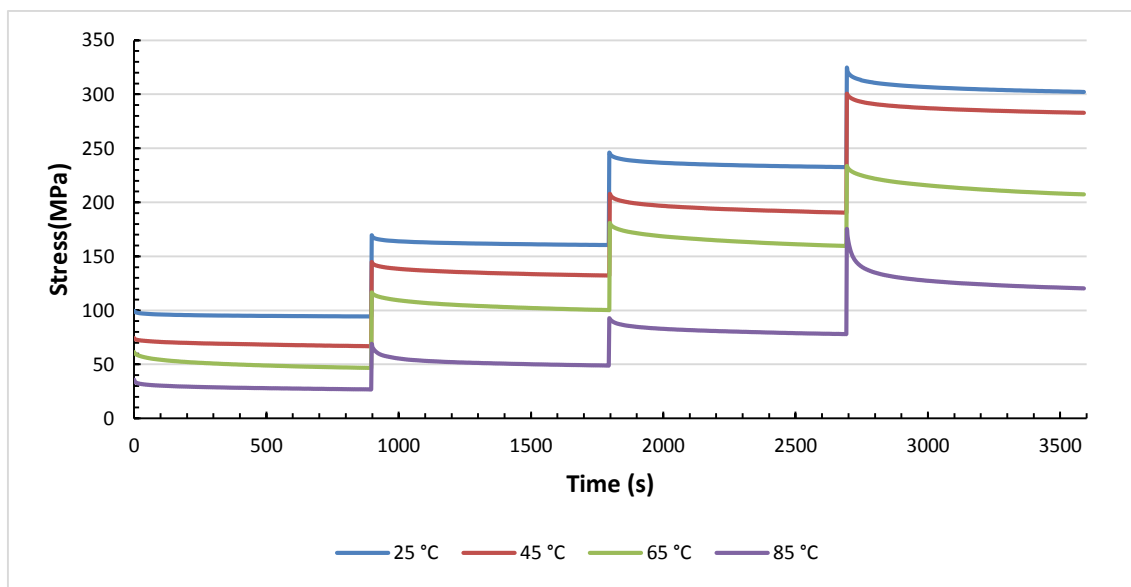


Figure 5.14. Stress relaxation curves for Pat-CNT composite samples at different temperatures.

Table 5.1 summarizes the percentages of stress reduction relative to the corresponding ultimate strength of each composite at different temperatures. To fair the comparison and since the majority of viscous alternation in the FRPs come from polymeric matrix the data shown in Table 5.1 are also normalized with respect to the minimum volume fraction of the matrix.

Table 5.1. Normilized percentage of stress reduction after 15 mins for the different composites configurations.

25°C	NT	p-CNT	Sub	ZnO	CNT	HT
20%	1.059342	0.668275	1.11975	0.866573	0.918513	0.868584
40%	1.766245	1.362406	2.710048	2.04619	1.433585	2.058689
60%	3.556796	2.151806	5.437709	3.748239	2.41281	4.263741
80%	4.814638	3.398118	10.20608	4.509082	3.842479	5.696185
45°C						
20%	1.913202	1.434373	1.758871	1.449862	1.608852	1.607032
40%	2.652005	2.15709	3.205849	2.877453	2.592039	2.651244
60%	4.229969	3.285414	5.93619	5.273846	3.841289	4.595969
80%	5.713981	4.837782	11.63207	7.102321	5.793113	6.950715
65°C						
20%	2.296914	1.905199	2.152696	1.807146	2.487673	2.47688
40%	4.361795	2.736171	5.193413	3.02819	3.995485	3.883592
60%	5.715676	3.568918	8.641025	5.250491	6.420151	5.103873
80%	5.990284	5.236189	16.82842	6.766621	5.757496	7.542014
85°C						
20%	4.026611	2.836245	3.672515	3.690051	2.923179	4.097273
40%	6.227166	3.52668	7.327485	4.203568	4.650827	7.090168
60%	7.896453	4.845896	12.40643	8.975187	6.581185	9.289945
80%	9.385748	5.924324	23.77193	9.584136	6.954356	12.39058

As it can be seen at all temperatures/ load levels the p-CNT sample outperformed the other samples whereas substrate sample showed the weakest resistance against time induced changes.

5.3.4. Creep

Creep tests were carried out at the load levels and temperatures identical to the relaxation tests and the results are plotted for each configuration in Figure 5.15- Figure 5.20. It can be interpreted from the creep data that increasing both temperature and load level causes more time induced deformation.

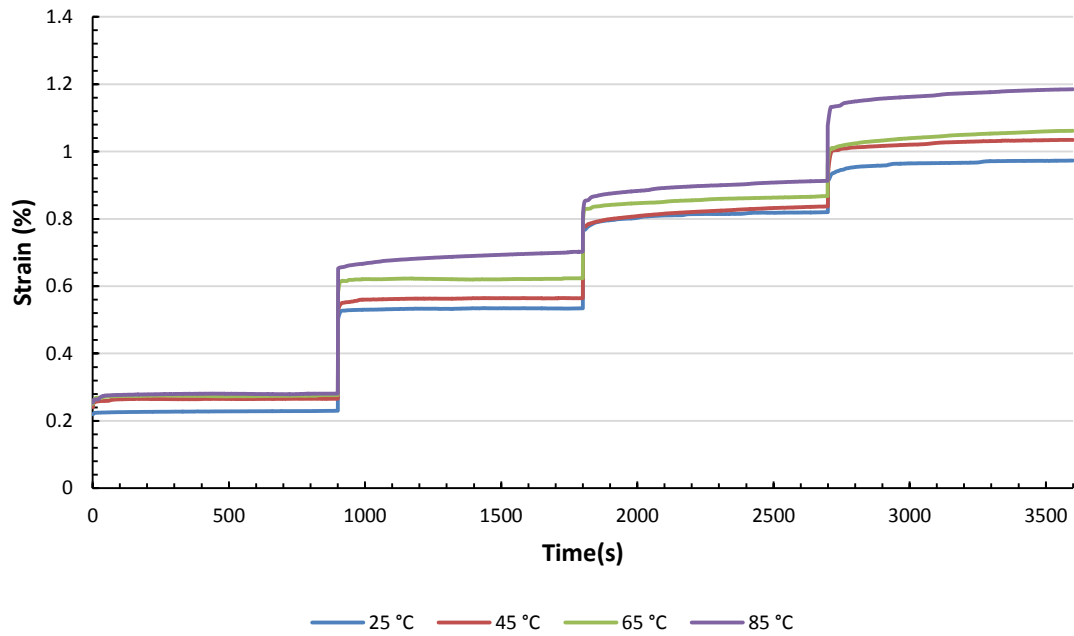


Figure 5.15. Creep curves for Neat composite samples at different temperatures.

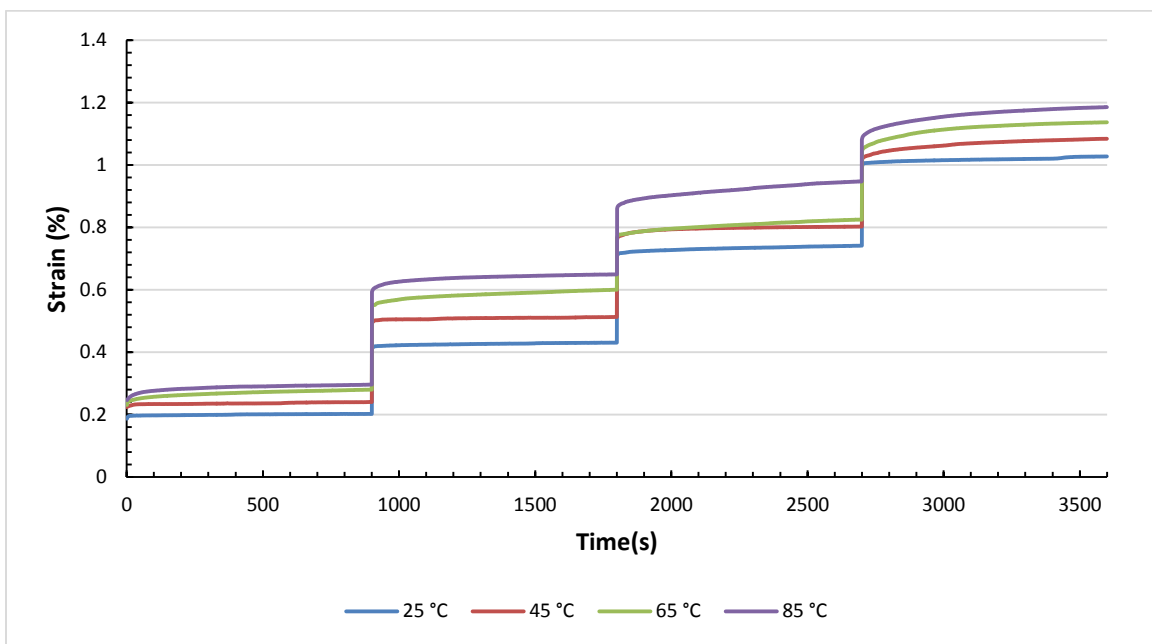


Figure 5.16. Creep curves for the HT composite samples at different temperatures.

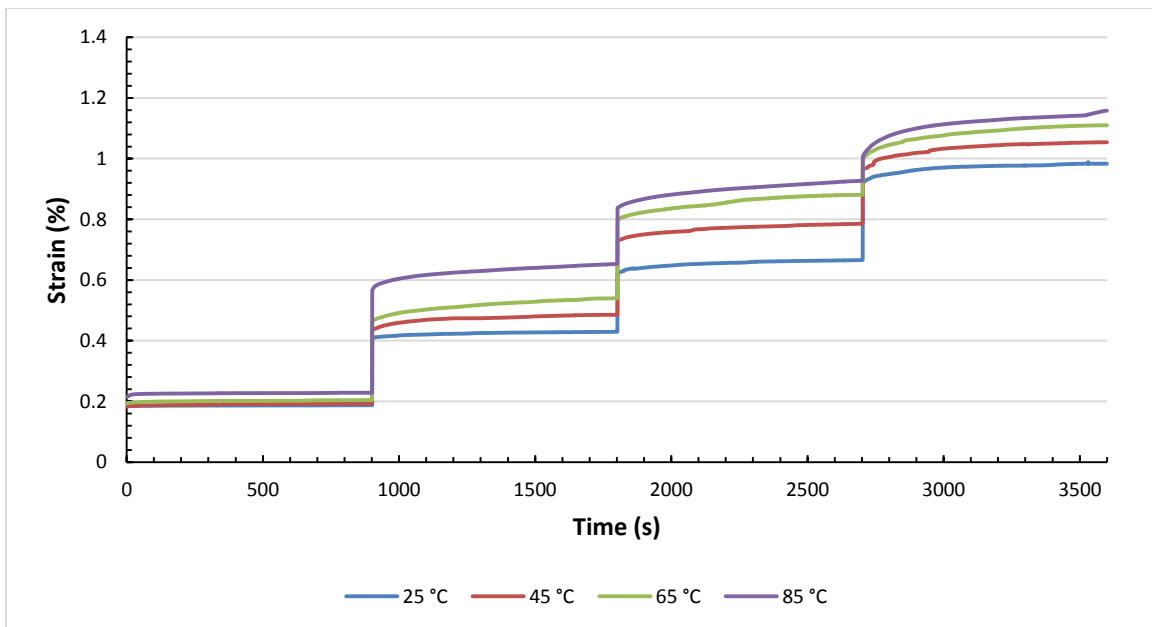


Figure 5.17. Creep curves for Substrate composite samples at different temperatures.

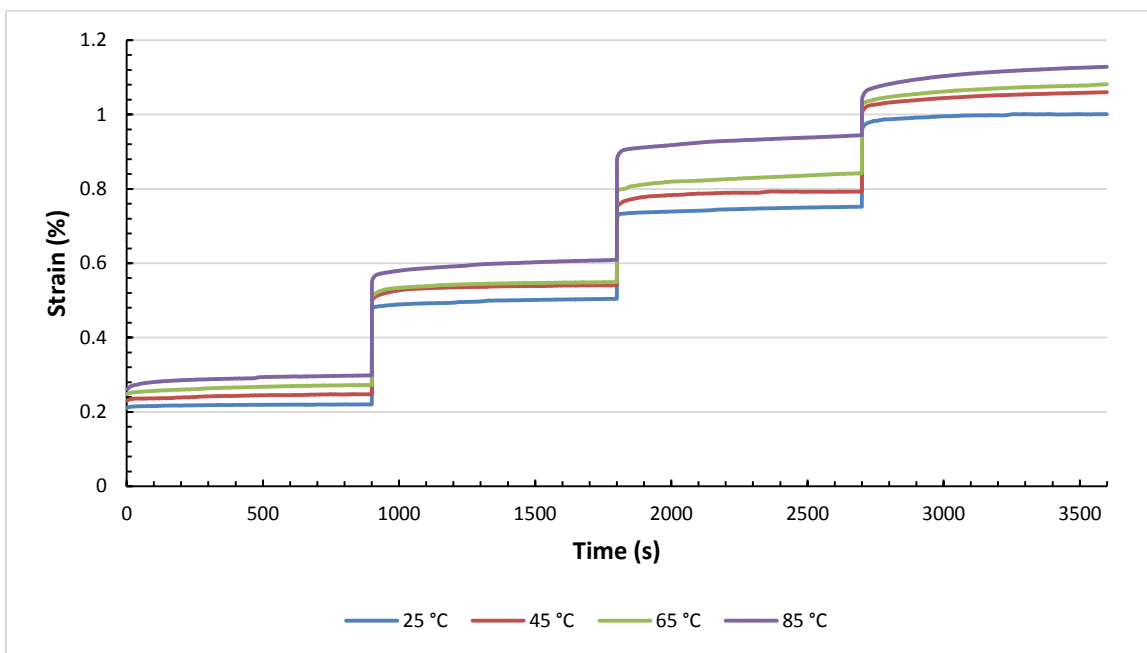


Figure 5.18. Creep curves for ZnO composite samples at different temperatures.

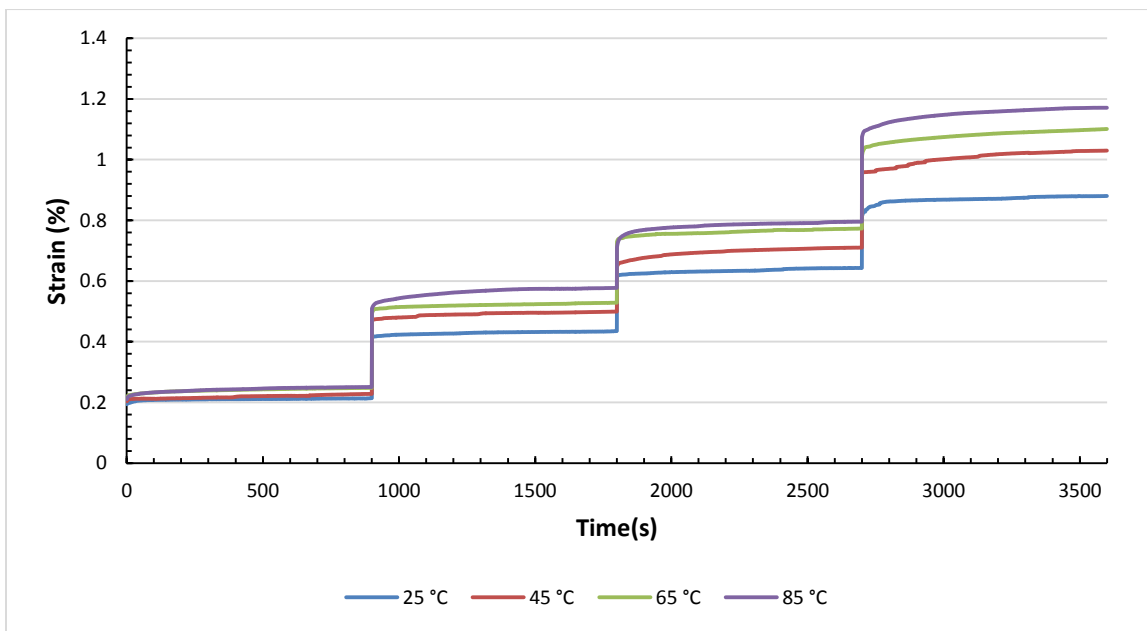


Figure 5.19. Creep curves for CNT composite samples at different temperatures.

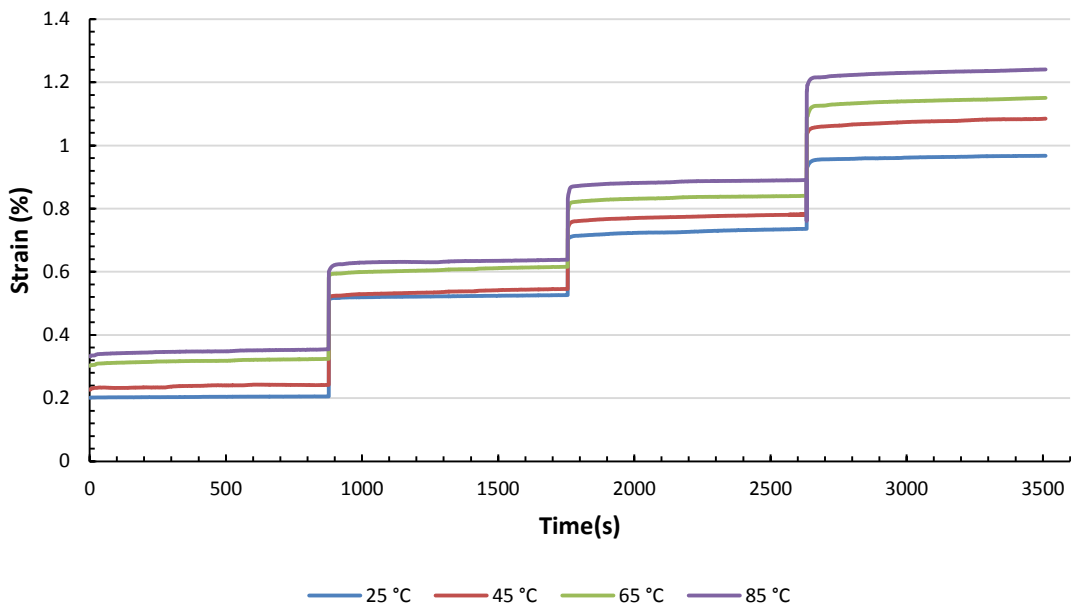


Figure 5.20. Creep curves for pat- CNT composite samples at different temperatures.

Table 5.2 summarizes the creep percentages normalized with respect to the volume fraction of the polymer to fiber content. As it can be seen the pat-CNT showed the maximum resistance against creep deformation. Also samples with ZnO NWs and CNTs showed improved viscoelastoplastic behavior compared to HT and Sub samples. Concluding from both creep and stress relaxation data, the presence of the nano filler reduced the viscoplastic deformation of the composites. The better adhesion of the nano fillers due to their high surface area and the presence of the Van der Waals forces between them and the polymer matrix are the main mechanisms that prevents the fibers from slipping against the matrix and finally detaching. On the other hand, the nano fillers themselves, when embedded in the polymeric matrix, improve the viscous properties considerably. However, when dense forests of nano fillers are grown on the surfaces of the carbon fibers, particularly in the case of CNTs, the wettability of fibers by the polymer becomes a concern.

In order to facilitate the infusion of the polymer in to the forest of the CNTs grown on the surface of the carbon fibers, enough space between CNT should be introduced by preventing the grow on all over the surface. Such spacing can be achieved by a topological growth like the patterned growth described earlier in this chapter. As it can be seen from all of mechanical testing the patterned CNT samples outperform the others considerably. The presence of the nano fillers in the interlaminar space provides the material with better resistance in terms of enhanced interlaminar shear strength (ILSS), the lack which is one of the main factors leading to delamination, delayed failure and creep properties of laminated composites.

Table 5.2. Normalized percentage of creep after 15 mins for the different composite configurations.

25°C	NT	p-CNT	Sub	ZnO	CNT	HT
20%	0.919422	0.857499	1.007407	0.648315	1.293726	0.933761
40%	2.225635	1.241896	1.481481	1.867918	1.383836	1.21874
60%	3.7728	1.827361	3.237037	1.989878	2.040353	1.934219
80%	3.84889	2.330033	5.192593	2.894952	4.267364	4.46265
45°C						
20%	1.440493	0.888466	1.375887	1.253448	1.499457	0.94134
40%	2.224122	1.718059	3.617021	2.793999	1.787108	1.27461
60%	3.797141	2.440607	4.212766	3.004075	3.831267	2.572607
80%	5.756212	2.531594	6.503546	3.879388	4.45553	4.677467
65°C						
20%	1.540948	1.080037	1.530769	1.510925	1.73784	2.511946
40%	2.534919	1.73595	5.776923	2.40563	2.002654	2.87518
60%	4.416993	2.520087	6.530769	3.122578	2.405392	2.9775
80%	5.857956	2.96887	8.707692	3.484015	4.888021	5.059704
85°C						
20%	2.098429	1.084969	1.748201	1.915418	1.950243	2.552874
40%	3.005857	1.903627	6.23741	3.014345	3.287415	2.880296
60%	5.540986	2.934348	6.42446	3.260833	4.14668	4.51741
80%	6.164843	3.304224	11.00719	4.462463	4.634241	5.402474

5.4. Phenomenological Modeling of Viscoplasticity

As described earlier in chapter 4, the model proposed by Sun and Gates^{32, 33, 181} is utilized to predict the creep behavior of different samples using data from stress relaxation and quasistatic tensile tests. Assuming uniaxial loading where the model considers the composites as a homogeneous orthotropic material the total strain for elastoplastic (time-independent) constitutive relation may be written as a combination of elastic and plastic terms.

$$\varepsilon^t = \varepsilon^e + \varepsilon^p \quad 5.1$$

Hooke's law provides the relation between elastic strain and stress, $\varepsilon^e = \frac{\sigma}{E}$, whereas, the plastic strain, ε^p , is expressed by a power law:

$$\varepsilon^p = A(\sigma)^n \quad 5.2$$

Where A and n are material constants found from experimental data. For a rate-dependent constitutive relation, the total strain rate is divided into elastic and viscoplastic components,

$$\dot{\varepsilon}^t = \dot{\varepsilon}^e + \dot{\varepsilon}^{vp} \quad 5.3$$

Where the elastic strain rate is

$$\dot{\varepsilon}^e = \frac{\dot{\sigma}}{E} \quad 5.4$$

While the viscoplastic strain rate is decomposed into two terms.

$$\dot{\varepsilon}^{vp} = \dot{\varepsilon}^{vp}' + \dot{\varepsilon}^{vp}''$$

5.5

Differentiating the plastic strain in elastoplastic constitutive relation, equation 5.6 gives the first part of the viscoplastic term, $\dot{\varepsilon}^{vp}'$.

$$\dot{\varepsilon}^{vp}' = \begin{cases} \{An(\sigma)^{n-1}\dot{\sigma}\} & \text{if } \dot{\sigma} > 0 \\ 0 & \text{if } \dot{\sigma} \leq 0 \end{cases}$$

5.6

Utilizing the “overstress” concept provides the second part of the viscoplastic term, $\dot{\varepsilon}^{vp}''$

as,

$$\dot{\varepsilon}^{vp}'' = \left[\frac{<H>}{K} \right]^{\vee_m}$$

5.7

Where H is the overstress, $<>$ are Macaulay brackets, and K and m are material constants found from experimental data. The overstress, $H = (\sigma - \sigma^*)$ is considered as a scalar quantity that relates the quasistatic stress, σ^* , to the dynamic or instantaneous stress, σ , at the same strain level, Ho and Krempel ¹⁸². Thus,

$$\dot{\varepsilon}^{vp}'' = \begin{cases} \left[\frac{\sigma - \sigma^*}{K} \right]^{\frac{1}{m}} & \text{if } \sigma > \sigma^* \\ 0 & \text{if } \sigma \leq \sigma^* \end{cases} \quad 5.8$$

The quasistatic stress is found by using previously defined elastoplastic equation 5.9, while the dynamic stress is the stress resulting from the time-dependent material behavior.

$$\varepsilon = \frac{\sigma^*}{E} + A(\sigma^*)^n \quad 5.9$$

5.4.1. Material Parameters

The temperature dependent material parameters K , m , A , and n are calculated from stress relaxation and quasistatic tensile experimental data. During the load relaxation, the quasistatic stress is constant, the total viscoplastic strain rate is zero and stress rate us negative; therefore from equations 5.5 and 5.3 it can be concluded:

$$\dot{\varepsilon}^{vp} = \dot{\varepsilon}^{vp}' = -\dot{\varepsilon}^e \quad 5.10$$

Combining equations

5.8 & 5.10 gives:

$$\dot{\varepsilon}^{vp} = - \frac{\dot{\sigma}}{E} = \left[\frac{\sigma - \sigma^*}{K} \right]^{1/m} \quad 5.11$$

To determine $\dot{\sigma}$ one can apply numerical differentiation to the stress-time data from load relaxation tests. To make the data from stress relaxation more comprehending and useful the $\log(\sigma) - \log(\dot{\varepsilon}^{vp})$ curves can be plotted from accelerated relaxation tests. This type of representation can generate an asymptotic value for the minimum or quasistatic stress. Figure 5.21 shows a sample of $\log(\sigma) - \log(\dot{\varepsilon}^{vp})$ plot for CNT samples at 85 °C.

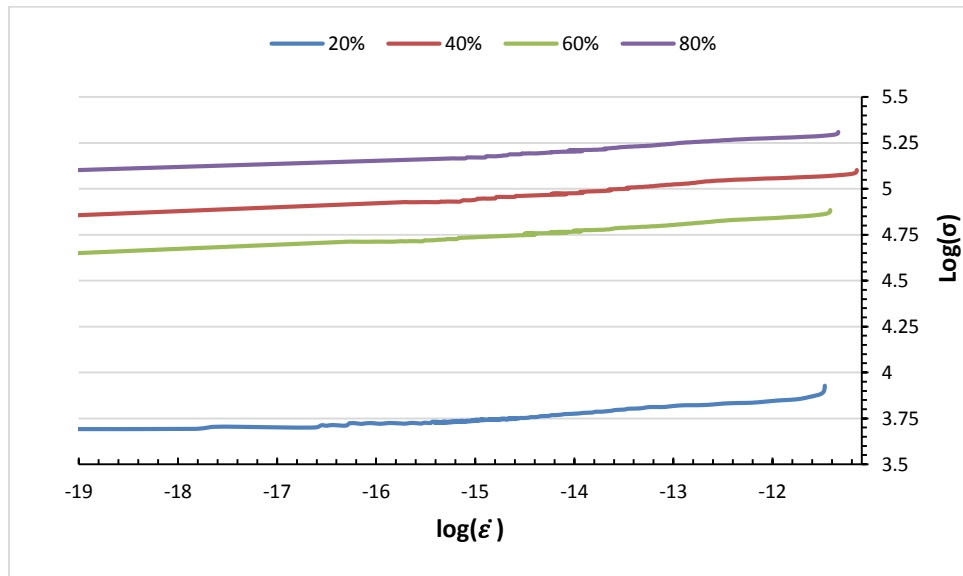


Figure 5.21. $\log(\sigma) - \log(\dot{\varepsilon}^{vp})$ Plot for CNT sample at 85 °C.

Upon obtaining σ^* by applying Gauss-Newton and nonlinear regression methods to equation 5.11, a logarithmic plot of the overstress versus the plastic strain rate can be plotted similar to the one demonstrated in Figure 5.22.

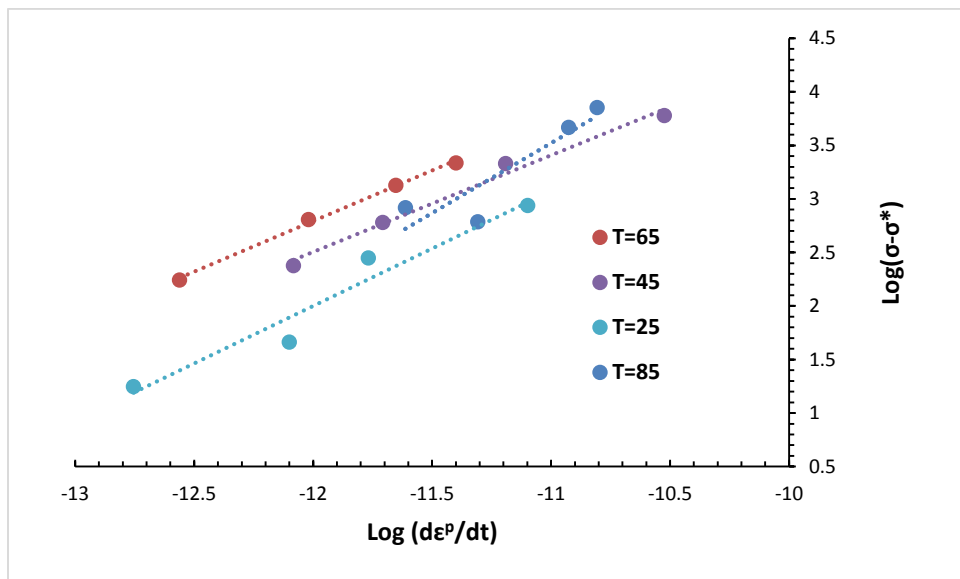


Figure 5.22. A sample plot of $\log(\sigma - \sigma^*) - \log(\dot{\varepsilon}^p)$ for CNT sample at different temperatures. These curves are used to determine the material constants K and m at each temperature (Overstress is in MPa).

Since different load relaxation tests were carried out at various load levels, a quasistatic stress-strain curve can be created at each temperature. Fitting the mentioned curve to equation 5.9 in logarithmic scale, material constant A and n can be calculated. A sample curve for logarithm of plastic strain versus quasistatic stress is shown in Figure 5.23.

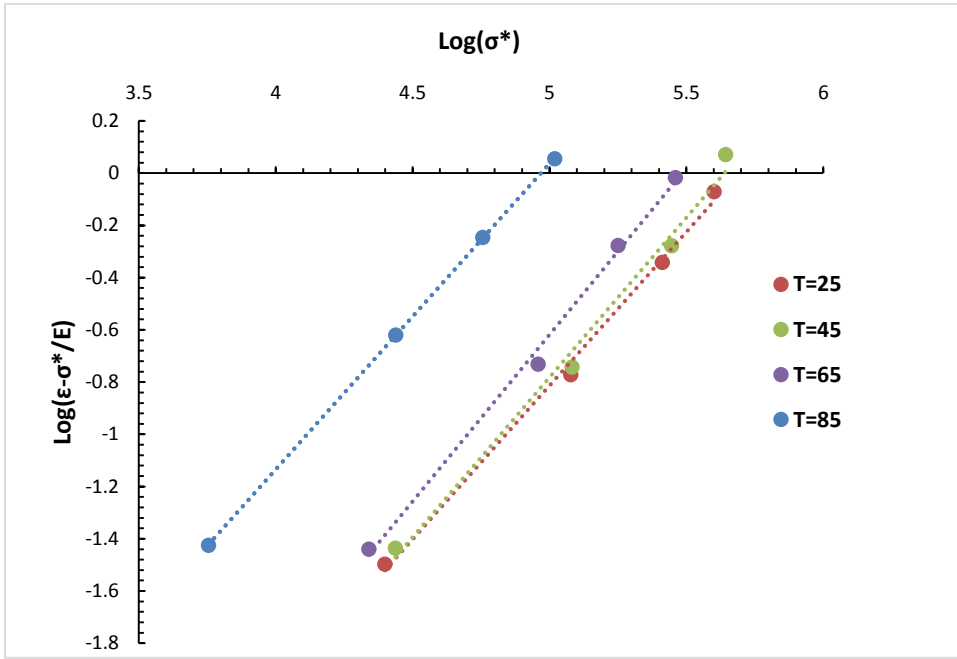


Figure 5.23. A sample plot of $\log(\epsilon - \sigma^*/E) - \log(\sigma^*)$ for CNT sample at different temperatures. These curves are used to determine the material constants A and n at each temperature (Quasistatic stress is in MPa).

Table 5.3 summarizes the four material's constants for all of the composites configuration.

It can be seen that at each temperature hybridized samples have relatively low m and k , while A and n vary slightly between the samples. Because k , A , and n do not exhibit significant temperature dependency and on the other hand m plays the most important role in the final determination of material viscoplastic response, to show the repeatability of the obtained parameters, each load relaxation test was repeated and the mean and standard deviation of m is repeated in Table 5.3 as well.

Table 5.3. Material Parameters m , K , n , and A for the different composite configurations.

25 °C	NT	HT	SUB	ZnO-G	CNT	Pat-CNT
m	0.9895	1.255	0.99	1.13	1.302	1.01
m_{stdv}	0.0265	0.145	0.1	0.02	0.062	0.13
K	.5E08	.6E08	1E08	6E07	4E08	.8E07
N	1.0	1.1	1.1	1.1	1.1	1.1
A	9E-07	5E-07	3E-07	4E-07	2E-07	6E-07
45 °C						
m	0.87	0.845	0.95	0.965	0.7735	0.796667
m_{stdv}	0.09	0.025	0.01	0.065	0.0495	0.08
K	0.1E06	0.3E06	1E06	4E06	0.2E06	0.2E06
n	1.1	1.0	0.9	1.315	1.1	1.1
A	5E-07	1E-06	5E-06	2E-07	4E-07	5E-08
65 °C						
m	0.88	0.795	0.715	1.12	1.04	0.395
m_{stdv}	0.18	0.125	0.075	0.09	0.06	0.065
k	3.2E06	.6E06	1E05	2.5E7	1.2E08	1E04
n	1.0	1.0	1.5	1.1	1.0	1.0
A	8E-07	5E-06	2E-09	3E-07	1E-06	1E-06
85 °C						
m	1.415	1.405	1.09	1.21	0.616	0.565
m_{stdv}	0.265	0.105	0.12	0.09	0.164	0.065
k	2.5E08	1.6E08	1.7E06	6.6E07	.9E05	.2E05
n	0.9	0.7	1.0	1.0	1.0	0.9
A	1E-05	6E-05	2E-06	1E-06	6E-06	1E-05

5.4.2. Model Validation

Throughout the creep process, the stress rate is zero so that the total strain rate can be written from equations 5.5 and 5.8 as:

$$\dot{\epsilon}^{vp} = \dot{\epsilon}^{(i)vp} = \left[\frac{\sigma - \sigma^*}{K} \right]^{1/m} \quad 5.12$$

Equation 5.12 is a first order nonlinear differential equation and can be solved numerically coupled to the nonlinear expression of quasistatic (equation 5.9). In this study Newton method was utilized together with Runge-Kutta to solve the coupled nonlinear differential equation with nonlinear equation of quasistatic stress. Figure 5.24 depicts a plot of model prediction results versus the experimental data for four representative temperatures and load levels. It can be seen that in the lower load levels/temperatures, models performs better predicting the creep data whereas increasing the load level/ temperature causes greater deviation from the test data. Also it should be noted that because the model treats the material to be homogenous and orthotropic, the effect of the nano fillers are already implicitly included in the material parameters so that the representative curves of the Figure 5.24 shows reasonable agreement between the model prediction and experimental data particularly at lower load/temperature levels.

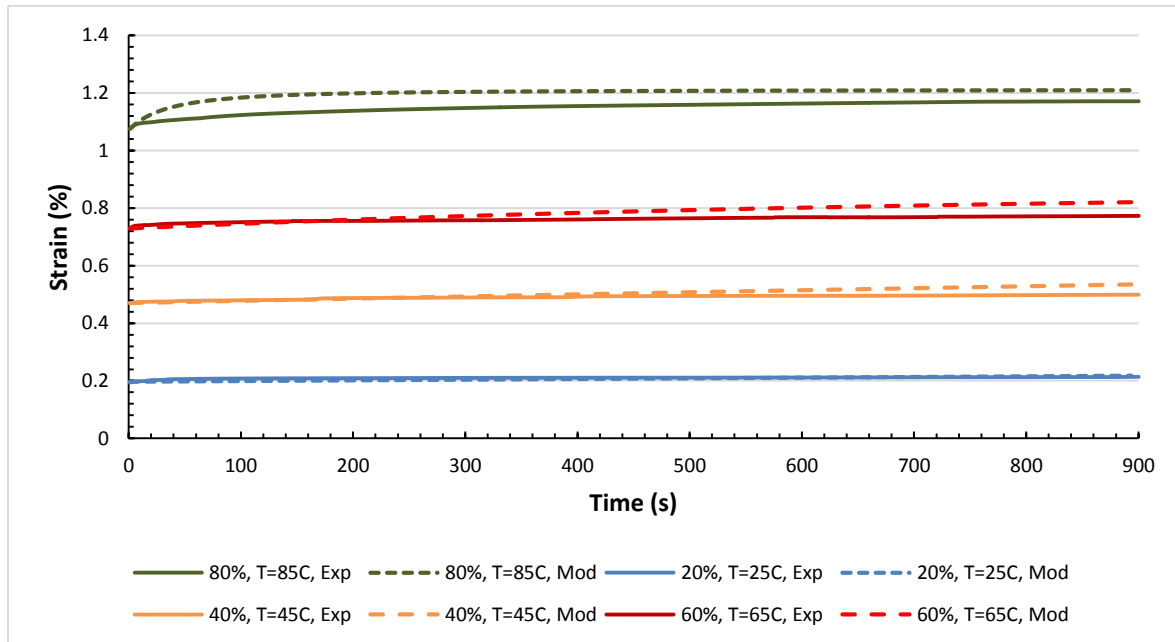


Figure 5.24. A sample plot of experimental data versus model prediction for the CNT composite sample at four different temperatures and load levels.

5.5. Conclusions

A comprehensive experimental investigation was conducted to study the viscoplastic behavior of polymer matrix hybrid nano composites. Different configurations of carbon fiber reinforced composites were fabricated with CNT and ZnO nano rods grown on their surfaces. Both axial stress relaxation and creep tests together with quasistatic tensile tests were performed at four different temperatures below the glass transition of the epoxy matrix. It was shown that hybridization increases the adhesion of the carbon fibers to the matrix and makes the composites more resistant to the slippage phenomena that occurs during the creep deformation. This also increases the magnitude of the interlaminar shear strength which is a determining factor in the delayed failure of the laminated composites. On the other hand the nano particles embedded in the polymer modify the viscous properties of the polymer itself. However a patterned growth of the CNTs on the carbon fibers which enhances the infusion of the polymeric matrix into the carbon fibers, out preformed the other configurations.

A phenomenological viscoelastic-viscoplastic model was utilized to predict the creep behavior of the both neat and nano composite laminates. The advantages of the model are: utilizing a very short stress/time data to predict the long term creep behavior and assuming the material to be orthotropic and homogenous which eliminates the need of costly and complicated homogenization techniques for nano composites. However because the model assumes that the behavior of the composite is uniform over different temperature and stress levels, it over predicts the material response at higher temperature/load levels. Different approaches have been made to reduce the temperature dependency of material parameters such as averaging m and applying it to

all of the temperatures or taking n and A to be constant at all temperatures. However all of these efforts are purely a sensitivity analysis to ensure the model will acquire a good fit for the experimental data rather than a physical basis. In this study it was shown that this model is applicable to hybridized nano composites with CNT and ZnO nano rods. The model predictions are in good agreement in lower load/temperature levels with the experimental data for nano composites. There is not a definite trend how the material parameters vary with temperature; however the hybridized composites with nano particles embedded in possess the lowest m in most of the temperature levels.

Chapter 6

6. Conclusions and Future Work

6.1. Conclusions

Molecular dynamic (MD) simulations were employed to understand the effect of chirality and length on the translocation of SWCNTs into a lipid bilayer cell membrane as well as surface functionalization. The simulations revealed that at the earliest time spans the mechanism of interaction between the SWCNT and the membrane is pure penetration. As time evolves penetration is accompanied by endocytosis and almost halfway through 60 ps, endocytosis becomes the dominant form of interaction. Also they showed that the presence of the (PEG) molecules enhanced the penetrability of the SWCNTs in the lipid membrane. The study also showed that shorter nano tubes -with length shorter than the thickness of the membrane- undergoes significant rotation during the endocytosis stage. By doubling the length, all of SWCNTs did penetrate through the membrane and the chirality showed its effect vividly. Lower chirality (higher aspect ratio) assisted the SWCNT to cross through the membrane faster. This was also concluded from the lesser adhesion established between the membrane and the SWCNT with lowest chirality; (10, 0). As lesser of the SWCNT energy was consumed to establish adhesion with the membrane

it was capable of translocating through the membrane from the other side faster than the other nano tubes. The results of the (10, 5) nano tubes suggest that there is an optimal aspect ratio/chirality value at which the adhesion to the membrane attains a minimum. Furthermore, the aspect ratio of the SWCNTs plays a major role in defining the mechanism by which the SWCNTs penetrate through the lipid membrane. The higher chiral tubes inserts slower with/without surface functionalizing PEG chains which reveals the marginal contribution of PEG (n=1) in the potential energy of the overall system. Schematic observations divulge a significant difference in the penetration mechanisms of f-SWCNTs versus SWCNTs where the PEGlayted ones tend to penetrate with less energy dependent mechanism and imposing more deflection to the membrane. It is shown that even in a small percentage of water soluble PEG chains when attached covalently to the SWCNT can slow down the penetration process regardless of the chirality. This property can be utilized for incorporating the SWCNT in a much smarter way for selective targeting of desired cells. Also PEG chains even in a small proportion reduced the adhesion energy up to 10% which concur with the experimental findings about the circulation time of PEGlayted particles in the blood serum.

The negative stiffness for ferroelectric materials undergoing phase transformation are typically explored while these materials are embedded in a stiff constraining media. However, this morphology deems the negative stiffness material inaccessible and thus no direct measurement of its stiffness is possible. In this study the stiffness and creep behavior of a low Curie temperature ferroelectric material were measured in-situ utilizing a novel non-isothermal nano indentation technique at the onset of its phase transformation. Triglycine sulfate (TGS) single crystals were grown by evaporating the water phase from the mixture of its constituents (i.e. sulfuric acid and

glycine in stochastic ratio). A single crystal of TGS was mounted on a hot stage along the (001) direction aligned with the indentation loading direction. Different nano indenter tips geometries were utilized to mimic the effect of constraining media (in the direction of the applied load) while the tests were carried out in a temperature range of 60 °C to 37 °C. Assuming a large ratio of the overall crystal volume to the sample/indenter contact area and slow cooling rates the thermally induced displacement of the nano indenter was eliminated by imposing proper corrections. It was shown that the TGS crystal, around its transformation temperature (47°C), exhibits both a negative stiffness (in the order of -1.5 GPa) and a negative creep compliance. This study provides a nondestructive methodology to examine the presence of negative stiffness and to quantify the change of the stiffness around the phase transition temperatures.

It was shown that fully crystalline ZnO nano rods could be grown on the surface of carbon fibers utilizing hydrothermal synthesis with minimal degradation of the fibers. The viscoelastic behavior of the hybrid ZnO nano rod/carbon fiber composites were investigated using both accelerated and prolonged methods. It was shown that accelerated methods such as the TTSP can be successfully applied to these composite in spite of their hierachal architecture with acceptable repeatability.

The DMA flexural creep tests revealed that the whiskerization of carbon fibers with ZnO nano rods reduces the creep compliance by 23% in comparison to composites based on neat carbon fibers. The better viscoelastic response of hybridized composites can be explained in terms of several micro and macro scale mechanisms. The dominant effect of ZnO nano rods on reducing the creep compliance comes from the fact that they serve as physical obstacles slowing down the rearrangement and slippage of polymeric chains (main mechanism for creep and relaxation of

polymers). Moreover, modifying the interfacial area via the addition of ZnO nano rods enhances the polymer/fiber adhesion and thus hampers the creep deformation in the CFRPs.

The obtained creep data was also verified utilizing the inverse proportional relation of creep compliance and stress relaxation modulus. Long term relaxation tests disclosed a considerable high relaxation modulus for composites with surface grown ZnO nano rods; the stress relaxation modulus improved by 65%, which is in agreement with the low creep compliance obtained from the TTPS master curves. Also DMA tests proved them to be advantageous for structural damping applications. The enhanced damping properties of the hybrid composites are attributed to the frictional sliding mechanisms of the high surface area/high aspect ratio ZnO nano rods grown uniformly throughout the FRP. This attenuation can also be related in part to electromechanical coupling of ZnO as well.

A comprehensive experimental investigation was conducted to study the viscoplastic behavior of polymer matrix hybrid nano composites. Different configurations of carbon fiber reinforced composites were fabricated with CNT and ZnO nano rods grown on their surfaces. Both axial stress relaxation and creep tests together with quasistatic tensile tests were performed at different temperatures below the glass transition of the epoxy matrix. It was shown that hybridization increases the adhesion of the carbon fibers to the matrix and makes the composites more resistant to the slippage phenomenon that occurs during the creep deformation. This also increases the magnitude of the interlaminar shear strength, which is a determining factor in the delayed failure of the laminated composites. On the other hand the nano particles embedded in the polymer modify the viscous properties of the polymer itself. However a patterned

growth of the CNTs on the carbon fibers, which enhances the infusion of the polymeric matrix into the carbon fibers, out, preformed the other configurations.

A phenomenological viscoelastic-viscoplastic model was utilized to predict the creep behavior of the both neat and nano composite laminates. The advantages of the model are: utilizing a very short stress/time data to predict the long term creep behavior and assuming the material to be orthotropic and homogenous which eliminates the need of costly and complicated homogenization techniques for nano composites. However because the model assumes that the behavior of the composite is uniform over different temperature and stress levels, it over predicts the material response at higher temperature/load levels. Different approaches have been made to reduce the temperature dependency of material parameters such as averaging m and applying it to all of the temperatures or taking n and A to be constant at all temperatures. However all of these efforts are purely a sensitivity analysis to ensure the model will acquire a good fit for the experimental data rather than a physical basis. In this study it was shown that this model is applicable to hybridized nano composites with CNT and ZnO nano rods. The model predictions are in good agreement in lower load/temperature levels with the experimental data for nano composites. There is not a definite trend how the material parameters vary with temperature; however the hybridized composites with nano particles embedded in possess the lowest m in most of the temperature levels.

6.2. Future Work

The number of unsolved problems in nanobiomechanics that can be addressed using sophisticated MD simulations is considerably large. For instance, the effect of nano particles on the enzymes of

immune system is still uncovered in many aspects. Most of such interactions starts with a simple adhesion which can be investigated via MD simulation in depth. Also effect of electronic charge on the internalization of conductive nano tubes and metallic nano particles in the cell membranes is still unrevealed.

In situ nano indentation tests can be carried out on the other ferroelectric materials using the dynamics modules and obtaining dynamic properties of the negative stiffness materials such as damping coefficient. Also multiphase nano composites with one of the phases being negative stiffness is another interesting topic that can be studied using the proposed method.

While the viscoelastic-plastic characterization of the hybrid composites was covered extensively in this study, however, other different modeling techniques can be utilized to better match the experimental data. Of growing interest are the micromechanics approaches where the nano phase can be considered separately. Also, while the simple phenomenological model provides a relatively good validation with the experiments, however, the model's parameters sensitivity affects its prediction significantly. An interesting parametric Uncertainty Quantification (UQ) can be utilized to investigate the sources of inaccuracy imposed by material parameters on the model's predictions.

7. References

1. Minary-Jolandan M, Yu M-F. Nanomechanical heterogeneity in the gap and overlap regions of type I collagen fibrils with implications for bone heterogeneity. *Biomacromolecules*. 2009;10:2565-2570
2. Fitzgerald M. Nanobiomechanics *Technology Review. MIT*. 2011
3. Bourzac K. The feel of cancer cells. *Technology Review. MIT*. 2011
4. Smart S, Cassady A, Lu G, Martin D. The biocompatibility of carbon nanotubes. *Carbon*. 2006;44:1034-1047
5. Warheit D. What is currently known about the health risks related to carbon nanotube exposures? *Carbon*. 2006;44:1064-1069
6. Gogotsi Y. How safe are nanotubes and other nanofilaments? *Materials Research Innovations*. 2003;7:192-194
7. Zeineldin R, Al-Haik M, Hudson LG. Role of polyethylene glycol integrity in specific receptor targeting of carbon nanotubes to cancer cells. *Nano letters*. 2009;9:751-757
8. Zhou F, Xing D, Ou Z, Wu B, Resasco DE, Chen WR. Cancer photothermal therapy in the near-infrared region by using single-walled carbon nanotubes. *Journal of biomedical optics*. 2009;14:021009
9. Kohli P, Martin CR. Smart nanotubes for biotechnology. *Current Pharmaceutical Biotechnology*. 2005;6:35-47
10. Li CY, Yang KQ, Zhang YY, Tang H, Yan F, Tan L, et al. Highly biocompatible multi-walled carbon nanotube-chitosan nanoparticle hybrids as protein carriers. *Acta Biomaterialia*. 2011;7:3070-3077
11. Villa CH, Dao T, Ahearn I, Fehrenbacher N, Casey E, Rey DA, et al. Single-walled carbon nanotubes deliver peptide antigen into dendritic cells and enhance IgG responses to tumor-associated antigens. *ACS Nano*. 2011;5:5300-5311
12. Varkouhi AK, Foillard S, Lammers T, Schiffelers RM, Doris E, Hennink WE, et al. Sirna delivery with functionalized carbon nanotubes. *International Journal of Pharmaceutics*. 2011;416:419-425
13. Kang B, Yu D, Dai Y, Chang S, Chen D, Ding Y. Cancer-cell targeting and photoacoustic therapy using carbon nanotubes as "bomb" agents. *Small*. 2009;5:1292-1301
14. Becker ML, Fagan JA, Gallant ND, Bauer BJ, Bajpai V, Hobbie EK, et al. Length-dependent uptake of DNA-wrapped single-walled carbon nanotubes. *Advanced Materials*. 2007;19:939-945
15. Roda E, Coccini T, Acerbi D, Barni S, Vaccarone R, Manzo L. Comparative pulmonary toxicity assessment of pristine and functionalized multi-walled carbon nanotubes intratracheally instilled in rats: Morphohistochemical evaluations. *Histology and Histopathology*. 2011;26:357-367

16. SM R, G M, X W, DM H, DJ B. Advances in pegylation of important biotech molecules: Delivery aspects. *Expert Opin. Drug Deliv.* 2008;5:371-383
17. Kailer A, Gogotsi YG, Nickel KG. Phase transformations of silicon caused by contact loading. *Journal of Applied Physics.* 1997;81:3057-3063
18. Suresh S. Crystal deformation: Colloid model for atoms. *Nat Mater.* 2006;5:253-254
19. Shen L, Cheong WCD, Foo YL, Chen Z. Nanoindentation creep of tin and aluminium: A comparative study between constant load and constant strain rate methods. *Materials Science and Engineering: A.* 2012;532:505-510
20. Everitt NM, Davies MI, Smith JF. High temperature nanoindentation - the importance of isothermal contact.
21. Prasad J, Diaz AR. Synthesis of bistable periodic structures using topology optimization and a genetic algorithm. *Journal of mechanical design* 2006;128:1298
22. AKMousavi, Kashamolla MR, Leseman ZC. Improved model for the adhesion of microcantilevers: Theory and experiments. *J. Micromech. Microeng.* 2013;23:115011
23. Mizuno T, Toumiya T, Takasaki M. Vibration isolation system using negative stiffness. *Int. J. Jap. Soc. Mech. Eng.* 2003;46:807-812
24. Lakes RS. Extreme damping in composite materials with a negative stiffness phase. *Physical review letters.* 2001;86:2897-2900
25. Atwater M, Mousavi A, Leseman Z, Phillips J. Direct synthesis and characterization of a nonwoven structure comprised of carbon nanofibers. *Carbon* 2013;57:363-370
26. Kashdan L, Seepersad C, Haberman M, S. Wilson P. Design, fabrication, and evaluation of negative stiffness elements using sls. *Rapid Prototyping Journal.* 2012;18:194-200
27. Sarlis AA, D. T. R. Pasala SMA, M. C. Constantinou MA, A. M. Reinhorn FA, S. Nagarajaiah MA, Taylor DP. Negative stiffness device for seismic protection of structures. *J. Struct. Eng.* 2013;139:1124-1133
28. Diamantini MC, Kleinert H. Strings with negative stiffness and hyperfine structure. *Physical review letters.* 1999;82:267-270
29. Jaglinski T, Frascone P, Moore B, Stone DS, Lakes RS. Internal friction due to negative stiffness in the indium-thallium martensitic phase transformation. *Philosophical Magazine.* 2006;2011:4285-4303
30. Lakes RS, Lee T, Bersie A, Wang YC. Extreme damping in composite materials with negative stiffness inclusions. *Nature.* 2001;410:565-567
31. Lakes RS, Drugan WJ. Dramatically stiffer elastic composite materials due to a negative stiffness phase. *Journal of the Mechanics and Physics of Solids.* 2002;50:979 - 1009
32. Gates TS. Experimental characterization nonlinear rate dependent behavior in advanced polymer matrix composites. *Experimental Mechanics.* 1992;32:68-73
33. Gates TS, Sun CT. Elastic/viscoplastic constitutive model for fiber reinforced thermoplastic composites. *AIAA.* 1991;29:457
34. Nicholson LM, Gates TS. The influence of cross-link density on the creep compliance of an advanced polyimide. *Journal of Thermoplastic Composite Materials.* 2001;14:477-488
35. Mousavi AK, Atwater MA, Mousavi BK, Jalalpour M, Taha MR, Leseman ZC. Mechanical and electrical characterization of entangled networks of carbon nanofibers. *Materials.* 2014;7:4845-4853

36. Morris DH, Yeow YT, Brinston HF. The viscoelastic behavior of the principal compliance matrix of unidirectional graphite/epoxy 1979
37. Bordonaro CM. Rate dependent mechanical behavior of high strength plastics: Experiment and modeling 1995 PhD thesis
38. Liu MC, Krempl E. A uniaxial viscoplastic constitutive model for fiber reinforced thermoplastics composites. *I. Mech. Phys. Solids.* 1979;27:377
39. Megnis M, Varna J. Micromechanics based modeling of nonlinear viscoplastic response of unidirectional composite. *Comp. Sci. and Tech.* 2003;63:19
40. Goldberg R, Hopkins D. Applications of boundary element methods to the micromechanical analysis of composite materials. *computers and structures.* 1995;56:721
41. Guedes RM, Marques AT. Analytical and experimental evaluation of nonlinear viscoelastic-viscoplastic composite laminates under creep, creep-recovery, relaxation and ramp loading. *Mechanics of time-dependent materials.* 1998;2:113
42. Dillard DA, straight MR, Brinson HF. The nonlinear viscoelastic characterization of graphite/epoxy composites. *polymer engineering and science.* 1987;27:116
43. Kawi M, Masuko Y. Macromechanical modeling and analysis of viscoplastic behavior of unidirectional fiber-reinforced composites. *Journal of Composite Materials* 37. 2003;37:1885
44. Krempl E. Relaxation behavior and modeling. *International Journal of Plasticity* 2001;17
45. Krempl E, Bordonaro CM. A state variable model for high strength polymers. *Polymer Engineering and Science* 1995;35:310
46. Colak OU. Modeling deformation behavior of polymers with viscoplasticity theory based on overstress. *International Journal of Plasticity*. 2005;21:145
47. Khan AS, Pamies OL. Time and temperature dependent response and relaxation of a soft polymer. *International Journal of Plasticity* 2002;18
48. Al-Haik M. Durability of a polymer matrix composite: Neural networks approach. *Mechanical Engineering.* 2001;PhD
49. Schapery RA. *Composite materials* 1974.
50. Tong L, Liu YX, Dolash BD, Jung Y, Slipchenko MN, Bergstrom DE, et al. Label-free imaging of semiconducting and metallic carbon nanotubes in cells and mice using transient absorption microscopy. *Nature Nanotechnology.* 2012;7:56-61
51. Niu JJ, Schrlau MG, Friedman G, Gogotsi Y. Carbon nanotube-tipped endoscope for in situ intracellular surface-enhanced raman spectroscopy. *Small.* 2011;7:540-545
52. Vakarelski IU, Brown SC, Higashitani K, Moudgil BM. Penetration of living cell membranes with fortified carbon nanotube tips. *Langmuir* 2007;23:10893-10896
53. Gao H, Shi W, Freund LB. Mechanics of receptor-mediated endocytosis. *Proc Natl Acad Sci* 2005;102:9469-9474
54. Yaron PN, Holt BD, Short PA, Lösche M, Islam MF, Dahl KN. Single wall carbon nanotubes enter cells by endocytosis and not membrane penetration. *Journal of Nanobiotechnology.* 2011;9
55. Pogodin S, Baulin VA. Can a carbon nanotube pierce through a phospholipid bilayer? *ACS Nano.* 2010;4:5293-5300
56. Lu Q, Moore JM, Huang G, Mount AS, Rao AM, Larcom LL, et al. RNA polymer translocation with single-walled carbon nanotubes. *Nanoletters.* 2004;4:2473-2477

57. Kostarelos K, Lacerda L, Pastorin G, Wu W, Wieckowski S, Luangsivilay J, et al. Cellular uptake of functionalized carbon nanotubes is independent of functional group and cell type. *Nature Nanotechnology*. 2007;2:108-113
58. Qiao R, Roberts AP, Mount AS, Klaine SJ, Ke PC. Translocation of c60 and its derivatives across a lipid bilayer. *Nano Letters*. 2007;7:614-619
59. Yang K, Ma Y-Q. Computer simulation of the translocation of nanoparticles with different shapes across a lipid bilayer. *Nature Nanotechnology*. 2010;5:579-583
60. Wallace EJ, Sansom MS. Blocking of carbon nanotube based nanoinjectors by lipids: A simulation study. *Nano Letters*. 2008;8:2751-2756
61. Al-Haik MS, Hussaini MY. Adhesion energy of single-wall carbon nanotube-polyethylene composite: Effect of magnetic field. *Journal of Computational and Theoretical Nanoscience*. 2006;3:243-248
62. Tanaka T, Liu HP, Fujii S, Kataura H. From metal/semiconductor separation to single-chirality separation of single-wall carbon nanotubes using gel. *Physica Status Solidi-Rapid Research Letters*. 2011;5:301-306
63. Lustig SR, Jagota A, Khripin C, Zheng M. Theory of structure-based carbon nanotube separations by ion-exchange chromatography of DNA/cnt hybrids. *Journal of Physical Chemistry B*. 2005;109:2559-2566
64. Ozawa H, Fujigaya T, Niidome Y, Hotta N, Fujiki M, Nakashima N. Rational concept to recognize/extract single-walled carbon nanotubes with a specific chirality. *Journal of the American Chemical Society*. 2011;133:2651-2657
65. Zhu XF, Li YG, Duan PF, Liu MH. Self-assembled ultralong chiral nanotubes and tuning of their chirality through the mixing of enantiomeric components. *Chemistry-a European Journal*. 2010;16:8034-8040
66. Cherukuri P, SM SB, Litovsky S, Weisman R. Nearinfrared fluorescence microscopy of single-walled carbon nanotubes in phagocytic cells. *J. Am. Chem. Soc.* 2004;126:15638-15639
67. Kam N, Jessop T, Wender P, Dai H. Nanotube molecular transporters: Internalization of carbon nanotubeprotein conjugates into mammalian cells. *J. Am. Chem. Soc.* 2004;126:6850-6851
68. Pantarotto D, Briand J, Prato M, Bianco A. Translocation of bioactive peptides across cell membranes by carbon nanotubes. *Chem Commun*. 2004;1:16-17
69. Bottini M, Rosato N, Bottini N. Peg-modified carbon nanotubes in biomedicine: Current status and challenges ahead. *Biomacromolecules*. 2011;12:3381-3393
70. Bianco A, Hoebeke J, Godefroy S, Chaloin O, Pantarotto D, Briand J-P, et al. Cationic carbon nanotubes bind to cpg oligodeoxynucleotides and enhance their immunostimulatory properties. *J. Am. Chem. Soc.* 2005;127:58-59
71. Bhirde AA, Patel S, Sousa AA, Patel V, Molinolo AA, Ji Y, et al. Distribution and clearance of peg-single-walled carbon nanotube cancer drug delivery vehicles in mice. *Nanomedicine*. 2010;5:1535-1546
72. Yaron PN, Holt BD, Short PA, Losche M, Islam MF, Dahl KN. Single wall carbon nanotubes enter cells by endocytosis and not membrane penetration. *Journal of nanobiotechnology*. 2011;9:45

73. Skandani AA, Zeineldin R, Al-Haik M. Effect of chirality and length on the penetrability of single-walled carbon nanotubes into lipid bilayer cell membranes. *Langmuir : the ACS journal of surfaces and colloids*. 2012;28:7872-7879
74. Lee H. Interparticle dispersion, membrane curvature, and penetration induced by single-walled carbon nanotubes wrapped with lipids and pegylated lipids. *The journal of physical chemistry. B*. 2013;117:1337-1344
75. Kraszewski S, Bianco A, Tarek M, Ramseyer C. Insertion of short amino-functionalized single-walled carbon nanotubes into phospholipid bilayer occurs by passive diffusion. *PloS one*. 2012;7:e40703
76. Gangupomu VK, Capaldi FM. Interactions of carbon nanotube with lipid bilayer membranes. *Journal of Nanomaterials*. 2011;2011:1-6
77. Liu F, Wu D, Kamm RD, Chen K. Analysis of nanoprobe penetration through a lipid bilayer. *Biochimica et biophysica acta*. 2013;1828:1667-1673
78. Foloppe N, MacKerell AD. All-atom empirical force field for nucleic acids: I. Parameter optimization based on small molecule and condensed phase macromolecular target data. *Journal of Computational Chemistry*. 2000;21:86-104
79. MacKerell AD, Banavali NK. All-atom empirical force field for nucleic acids: II. Application to molecular dynamics simulations of DNA and RNA in solution. *Journal of Computational Chemistry*. 2000;21:105-120
80. Alexander D, MacKerell J, Banavali N, Foloppe N. Development and current status of the CHARMM force field for nucleic acids. *Biopolymers (Nucleic Acid Sciences)*. 2001;56:257-265
81. A. D. MacKerell J, Bashford D, Bellott M, R. L. Dunbrack J, Evanseck JD, Field MJ, et al. All-atom empirical potential for molecular modeling and dynamics studies of proteins. *J. Phys. Chem. B*. 1998;102:3586-3616
82. Feller SE, Alexander D, MacKerell J. An improved empirical potential energy function for molecular simulations of phospholipids. *J. Phys. Chem. B*. 2000;104:7510-7515
83. Klauda JB, Brooks BR, Alexander D, MacKerell J, Venable RM, Pastor RW. An ab initio study on the torsional surface of alkanes and its effect on molecular simulations of alkanes and a dppc bilayer. *J. Phys. Chem. B*. 2005
84. Mensah SY, Allotey FKA, Mensah NG, Nkrumah G. Differential thermopower of a CNT chiral carbon nanotube. *Journal of Physics-Condensed Matter*. 2001;13:5653-5662
85. Liang SD, Xu NS. Chirality effect of single-wall carbon nanotubes on field emission. *Applied Physics Letters*. 2003;83:1213-1215
86. Natsuki T, Tantrakarn K, Endo M. Prediction of elastic properties for single-walled carbon nanotubes. *Carbon*. 2004;42:39-45
87. Lopez CF, Moore PB, Shelley JC, Shelley MY, Klein ML. Computer simulation studies of biomembranes using a coarse grain model. *Computer Physics Communications*. 2002;147:1-6
88. Shelley JC, Shelley MY, Reeder RC, Bandyopadhyay S, Klein ML. A coarse grain model for phospholipid simulations. *Journal of Physical Chemistry B*. 2001;105:4464-4470
89. Zhou G, Duan W, B.Gu. Electronic structure and field-emission characteristics of open-ended single-walled carbon nanotubes. *Phys. Rev. Lett.* 2001; 87:095504

90. Al-Haik M, Hussaini MY, Garmestani H. Adhesion energy in carbon nanotube-polyethylene composite: Effect of chirality. *Journal of Applied Physics*. 2005;97
91. Liang ZY, Gou JH, Zhang C, Wang B, Kramer L. Investigation of molecular interactions between (10,10) single-walled nanotube and epon 862 resin/detda curing agent molecules. *Materials Science and Engineering A*. 2004;365:228-234
92. Allinger NL, Yuh YH, Lii J-H. Molecular mechanics. The mm3 force field for hydrocarbons. 1. *Journal of the American Chemical Society*. 1989;111:8551–8566
93. Lii J-H, Allinger NL. Molecular mechanics. The mm3 force field for hydrocarbons. 2. Vibrational frequencies and thermodynamics. *Journal of the American Chemical Society*. 1989;111:8566–8575
94. Lii J-H, Allinger NL. Molecular mechanics. The mm3 force field for hydrocarbons. 3. The van der waals' potentials and crystal data for aliphatic and aromatic hydrocarbons. *Journal of the American Chemical Society*. 1989;111:8576–8582
95. Dudek MJ, Ponder JW. Accurate modeling of the intermolecular electrostatic energy of proteins. *Journal of Computational Chemistry*. 1995;16:791-816
96. Rapaport DC. *The art of molecular dynamics simulation*. Cambridge, UK: Cambridge University Press; 1995.
97. Leach AR. *Molecular modeling principles and applications*. Essex, England: Prentice Hall; 2001.
98. Skandani AA, Al-Haik M. Reciprocal effects of the chirality and the surface functionalization on the drug delivery permissibility of carbon nanotubes. *Soft Matter*. 2013;9
99. Wang AZ, Gu F, Zhang L, Chan JM, Radovic-Moreno A, Shaikh MR, et al. Biofunctionalized targeted nanoparticles for therapeutic applications. *Expert opinion on biological therapy*. 2008;8:1063-1070
100. Hess B, Kutzner C, Spoel Dvd, Lindahl E. Gromacs 4: Algorithms for highly efficient, load-balanced, and scalable molecular simulation. *Journal of Chemical Theory and computation* 2008;4:435-447
101. Berendsen HJC, Spoel Dvd, Drunen Rv. Gromacs: A message-passing parallel molecular dynamics implementation. *Computer Physics Communications*. 1995;91:43-56
102. Van Der Spoel D, Lindahl E, Hess B, Groenhof G, Mark AE, Berendsen HJ. Gromacs: Fast, flexible, and free. *Journal of Computational Chemistry*. 2005;26:1701-1718
103. Miyamoto S, Kollman PA. An analytical version of the shake and rattle algorithms for rigid water models. *Journal of Computational Chemistry*. 1992;13:952-962
104. Skandani AA, Zeineldin RR, Al-Haik M. Effect of chirality and length on the penetrability of single wall carbon nanotubes into lipid bilayer cell membranes. *Langmuir* 2012;28:7872-7878-7879
105. Lopez CF, Nielsen SO, Moore PB, Klein ML. Understanding nature's design for a nanosyringe. *Proceedings of the National Academy of Sciences of the United States of America*. 2004;101:4431-4434
106. Chung DDL. Structural composite materials tailored for damping. *Journal of Alloys and Compounds*. 2003;355:216-223
107. Paul B. Prediction of elastic constants of multiphase materials. *Trans. AIME*. 1960; 218:36-41

108. Hashin Z, Shtrikman S. A variational approach to the theory of the elastic behavior of multiphase materials. *J. Mech. Phys. Solids.* 1963;11:127-140
109. Matthias BT, Miller CE, Remeika JP. Ferroelectricity of glycine sulfate. *physical review.* 1956;104:849-850
110. Andriyevsky B, Esser N, Patryn A, Cobet C, Ciepluch-Trojanek W, Romanyukc M. Band structure and uv optical spectra of tgs crystals in the range of 4–10 ev. *Physica B.* 2006;373:328-333
111. Logeswari J. Synthesis and dielectric studies on pure and doped triglycine sulphate single crystals for laser applications. *Optoelectronics and Advanced Materials – Rapid Communications.* 2008;2:630-634
112. Deguchi K, Nakamura E. Thermal expansion coefficient of tgs near the critical temperature. *Physics Letters.* 1977;60A:351-352
113. Skandani AA, Pham T, Luhrs C, MS El-Genk MA-H. Effects of composition and transparency on photo and radioluminescence of y₂o₃: Eu complexes. *Radiation Effects & Defects in Solids.* 2011;166:501-512
114. Alexandru HV, Berbecaru C. Growth and kinetic measurements of triglycine sulphate crystals. *Cryst. Rex Technol.* 1995;30:307-315
115. Smith JFZ, S. High temperature nanoscale mechanical property measurements *Surface Engineering.* 2000;143-146
116. Beake BDaS, James F. High-temperature nanoindentation testing of fused silica and other materials philosophical magazine *Philosophical Magazine.* 2002;82:2179 — 2186
117. Milhans J, Li DS, Khaleel M, Sun X, Al-Haik MS, Harris A, et al. Mechanical properties of solid oxide fuel cell glass-ceramic seal at high temperatures. *Journal of Power Sources.* 2011;196:5599-5603
118. Cizman A, Antropova T, Anfimova I, Drozdova I, Rysiakiewicz-Pasek E, Radojewska EB, et al. *Size-driven ferroelectric-paraelectric phase transition in tgs nanocomposites.* 2013.
119. Oliver WC, Pharr GM. An improved technique for determining hardness and elastic modulus using load and displacement sensing indentation experiments. *Journal of Materials Research.* 1992;7:1564-1583
120. Skandani AA, Ctvrtlik R, Al-Haik M. Nanocharacterization of the negative stiffness of ferroelectric materials *Applied Physics Letters.* 2014;105:082906
121. Doerner MF, Nix WD. A method for interpreting the data from depth-sensing indentation instruments. *Journal of Materials Research.* 1986;1:601-609
122. Heydari D, Skandani A, Haik MA. Effect of carbon content on carbide morphology and mechanical properties of ar white cast iron with 10–12% tungsten. *Materials Science and Engineering: A.* 2012;542:113-126
123. Al-Haik M, Dai J, Garcia D, Chavez J, Taha MR, Luhrs C, et al. Novel growth of multiscale carbon nanofilaments on carbon and glass fibers. *Nanoscience and Nanotechnology Letters.* 2009;1:122-127
124. Qin Y, Wang X, Wang ZL. Microfibre-nanowire hybrid structure for energy scavenging. *Nature.* 2008;451:809-813
125. Wang ZL, Song J. Piezoelectric nanogenerators based on zinc oxide nanowire arrays. *Science.* 2006;312:242-246

126. Tonezzer M, Lacerda RG. Integrated zinc oxide nanowires/carbon microfiber gas sensors. *Sensors. Actuat. B-Chem.* 2010;150:517-522
127. Jo SH, Banerjee D, Ren ZF. Field emission of zinc oxide nanowires grown on carbon cloth. *Appl. Phys. Lett.* 2004;85:1407
128. Unalan HE, Wei D, Suzuki K, Dalal S, Hiralal P, Matsumoto H, et al. Photoelectrochemical cell using dye sensitized zinc oxide nanowires grown on carbon fibers. *Appl. Phys. Lett.* 2008;93:133116
129. Hyer MW. *Stress analysis of fiber reinforced composite materials*. USA: DEStech publications; 2009.
130. Zhou W, Jin Hb. Acoustic emission based flexural characteristics of glass fiber reinforced composites embedded with zno nanowhiskers. *J. Compos. Mat.* 2011;46:291-299
131. Alipour Skandani A, Masghouni N, Case SW, Leo DJ, Al-Haik M. Enhanced vibration damping of carbon fibers-zno nanorods hybrid composites. *Applied Physics Letters*. 2012;101:073111
132. Skandani AA, Masghouni N, Al-Haik M. Superior damping of hybrid carbon fiber composites grafted by zno nanorods. *Topics in Modal Analysis*. 2012;7:187-193
133. Guo C, Zheng Z, Zhu Q, Wang X. Preparation and characterization of polyurethane/zno nanoparticle composites. *Polymer-Plastics Technology and Engineering*. 2007;46:1161-1166
134. Ascione L, Berardi VP, D'Aponte A. A viscoelastic constitutive law for frp materials. *International Journal for Computational Methods in Engineering Science and Mechanics*. 2011;12:225-232
135. Miyano Y, Kanemitsu M, Kunio T, Kunih H. Role of matrix resin on fracture strengths of unidirectional cfrp. *Journal of Composite Materials*. 1986;20:520-538
136. Aboudi J, Cederbaum G. Analysis of viscoelastic laminated composite plates. *Composite Structures*. 1989;12:243-256
137. Scott DW, Lai JS, Zureick A-H. Creep behavior of fiber-reinforced polymeric composites: A review of the technical literature. *Journal of Reinforced Plastics and Composites*. 1995;14:588-617
138. Findley WN. Mechanism and mechanics of creep of plastics. *SPEJ*. 1960;16:57-65
139. Schapery RA. A theory of non-linear thermoviscoelasticity based on irreversible thermodynamics. *Proceedings of The Fifth US National Congress in Applied Mechanics, ASME*. 1966
140. Raghavan J, Meshii M. Creep of polymer composites *Composites Science and Technology* 1998;57:1673-1688
141. Goertzen WK, Kessler MR. Creep behavior of carbon fiber/epoxy matrix composites. *Materials Science and Engineering: A*. 2006;421:217-225
142. Abdel-Magid B, Lopez-Anido R, Smith G, Trofka S. Flexure creep properties of e-glass reinforced polymers. *Composite Structures*. 2003;62:247-253
143. Abdel-Magid BM, Gates TS. Accelerated testing of polymeric composites using the dynamic mechanical analyzer. *NASA report*. 2001
144. Shankar K, Lakkad SC. Damping in fibre reinforced plastics. *J. Mater. Sci. Lett.* 1982;1:53-57

145. Adams RD, Maher MR. Damping in advanced polymer–matrix composites. *J. Alloy. Compd.* 2003;355:126-130
146. Chandra R, Singh SP, Gupta K. Micromechanical damping models for fiber-reinforced composites: A comparative study. *Compos. Part A-Appl. S.* 2002;33:787-796
147. Hudnut SW, Chung DDL. Use of submicron diameter carbon filaments for reinforcement between continuous carbon-fiber layers in a polymer-matrix composite. *Carbon.* 1995;33:1627-1631
148. Vlasveld DPN, Bersee HEN, Picken SJ. Nanocomposite matrix for increased fibre composite strength. *Polymer.* 2005;46:10269-10278
149. Dutra RCL, Soares BG, Campos EA, Silva JLG. Hybrid composites based on polypropylene and carbon fiber and epoxy matrix. *Polymer.* 2000;41:3841-3849
150. Baruah S, Dutta J. Hydrothermal growth of zno nanostructures. *Sci. Technol. Adv. Mater.* 2009;10:013001
151. Sun L, Gibson RF, Gordaninejad F, Suhr J. Energy absorption capability of nanocomposites: A review. *Compos. Sci. Technol.* 2009;69:2392-2409
152. . Based on the results obtained by the authors of this article
153. Zhou X, Shin E, Wang KW, Bakis CE. Interfacial damping characteristics of carbon nanotube-based composites. *Compos. Sci. Technol.* 2004;64:2425-2437
154. Thostenson ET, Chou TW. Aligned multi-walled carbon nanotube-reinforced composites: Processing and mechanical characterization. *J. Phys. D Appl. Phys.* 2002;35:L77-L80
155. Rajoria H, Jalili N. Passive vibration damping enhancement using carbon nanotube-epoxy reinforced composites. *Compos. Sci. Technol.* 2005;65:2079-2093
156. Gojny FH, Wichmann MHG, Kopke U, Fiedler B, Schulte K. Carbon nanotube-reinforced epoxy-composite sites: Enhanced stiffness and fracture toughness at low nanotube content. *Compos. Sci. Technol.* 2004;64:2363-2371
157. Gojny FH, Wichmann MHG, Köpke U, Fiedler B, Schulte K. Carbon nanotube-reinforced epoxy-composites: Enhanced stiffness and fracture toughness at low nanotube content. *Composites Science and Technology.*, 2004;64:2363-2371
158. Suhr J, Koratkar N, Keblinski P, Ajayan P. Viscoelasticity in carbon nanotube composites. *Nat. Mater.* 2005;4:134-137
159. Skandani AA, Boroujeni AY, Al-Haik M. Temperature dependent viscoelastic behavior of frp/zno nano-rods hybrid nanocomposites. *ASME 2013 International Mechanical Engineering Congress and Exposition.* 2013;V009T010A036-V009T010A036
160. Skandani AA, Boroujeni AY, Kalhor R, Case SW, Al-Haik M. Viscoelastic behavior of epoxy/carbon fiber/zno nano-rods hybrid composites. *Polymer Composites.* 2014
161. Tobolsky AV. *Properties and structures of polymers.* New York: Wiley; 1960.
162. Ferry JD. *Viscoelastic properties of polymers.* New York: Wiley; 1980.
163. Sullivan JL. *Comp. Sci. and Tech.* 1990;39:207-232
164. Sumita M, Gohda H, Asai S, Miyasaka K. New damping materials composed of piezoelectric and electro-conductive, particle-filled polymer composites: Effect of the electro mechanical coupling factor. *Makromol. Chem., Rapid Commun.* . 1991;12:657-661
165. Liu Z, Wang Y, Huang G, Wu J. Damping characteristics of chlorobutyl rubber/poly(ethyl acrylate)/piezoelectric ceramic/carbon black composites. *J. Appl. Polym. Sci.* 2008;108:3670-3676

166. Zhang Q, Liu J, Sager R, Dai L, Baur J. Hierarchical composites of carbon nanotubes on carbon fiber: Influence of growth condition on fiber tensile properties. *Composites Science and Technology*. 2009;69:594-601
167. Choi E, Al-Haik M, Garmestani H, al e. Enhancement of thermal and electrical properties of carbon nanotube polymer composites by magnetic field processing. *Journal of Applied Physics*. 2003; 94
168. Garmestani H, Al-Haik MS, K. Dahmen ea. Epoxy mediated alignment of single wall carbon nanotubes under high magnetic fields. *Advanced Materials*. 2003;15
169. Jin L, Bower C, Zhou O. Alignment of carbon nanotubes in a polymer matrix by mechanical stretching. *Applied Physics Letters*. 1998;73:1197-1199
170. Garcia E, Wardle BL, deVillori RG, Wicks S, Ishiguro K, Yamamoto N, et al. Aligned carbon nanotube reinforcement of advanced composite ply interfaces. *49th AIAA/ASME/ASCE/AHS/ASC Structures, Structural Dynamics, and Materials Conference 16t*. 2008
171. Xia Z, Curtin WA, Li H, B.W. Sheldon, Liang J, Chang B, et al. Direct observation of toughening mechanisms in carbon nanotube ceramic matrix composites. *Acta Materialia*. 2004;52:931-944
172. Li YL, Kinloch IA, Windle AH. *Science*. 2004;304
173. E. Bekyarova ETT, A. Yu, H. Kim, J. Gao, J. Tang, H. T. Hahn, T.-W. Chou, M. E. Itkis and R. C. Haddon. Multiscale carbon nanotube-carbon fiber reinforcement for advanced epoxy composites. *Langmuir*. 2007;23:3970-3974
174. Wang ZL. Energy harvesting for self-powered nanosystems. *Nano Research*. 2008;1:1-8
175. Gullapalli H, Vemuru VS, Kumar A, Botello-Mendez A, Vajtai R, Terrones M, et al. Flexible piezoelectric zno–paper nanocomposite strain sensor. *small*. 2010;6:1641-1646
176. Kumar A, Gullapalli H, Balakrishnan K, Botello-Mendez A, Vajtai R, Terrones M, et al. Flexible ZnO-cellulose nanocomposite for multisource energy conversion. *small*. 2011;7:2173-2178
177. Wang ZL. Energy harvesting using piezoelectric nanowires—a correspondence on “energy harvesting using nanowires?” by alexe et al. *Advanced Materials*. 2009;21:1311-1315
178. Wagner R, Ellis W. Vapor-liquid-solid mechanism of single crystal growth. *Applied Physics Letters*. 1964;4:89-90
179. Lin Y, Ehlert G, Sodano HA. Increased interface strength in carbon fiber composites through a zno nanowire interphase. *Advanced Functional Materials*. 2009;19:2654-2660
180. Ehlert GJ, Sodano HA. Zinc oxide nanowire interphase for enhanced interfacial strength in lightweight polymer fiber composites. *ACS Applied Materials & Interfaces*. 2009;1:1827-1833
181. Gates TS. *Effects of elevated temperature on the viscoplastic modeling of graphite/polymeric composites*. American Society for Testing and Material ASTM; 1933.
182. Ho K, Kreml E. Extension of the viscoplasticity theory based on overstress (vbo) to capture non-standard rate dependence in solids. *International Journal of Plasticity*. 2002;18:851